INVESTIGATION OF THE MAGNETIC PROPERTIES OF NON-THIOLATED Au NANO-STRUCTURES GROWN BY LASER ABLATION

Chenlin Zhao

Dissertation submitted to the faculty of the
Virginia Polytechnic Institute and State University
in partial fulfillment of the requirements for the degree of

Doctor of Philosophy
In
Materials Science and Engineering

Jeremiah T. Abiade, Chair
Jiefang Li,
Dwight D. Viehland
Mitsuhiro Murayama
Guo-Quan Lu
Gordon T. Yee

July 25th 2014 Blacksburg, Virginia

Keywords: Ferromagnetism, Gold Nano-structures, Pulsed Laser Deposition

Investigation of the Magnetic Properties of Non-Thiolated Gold Nano-structures Grown By Laser Ablation

Chenlin Zhao

ABSTRACT

Although it is known that gold (Au) is diamagnetic in bulk form, it has been reported that Au displays magnetic properties when reduced to the nano-scale. Researchers found magnetism in Au nanoparticles (NPs) in a size range from 2 to 10 nanometers. Moreover, the Au nanoparticles are usually coated by thiol-containing organic caps, which are believed to be responsible for the magnetism. However, others suggest that organic capping is not necessary to observe magnetism in Au NPs, and magnetism may be an intrinsic property for nano-structured gold. For this investigation, we used pulsed laser deposition to prepare nano-structured gold of different sizes and concentrations to investigate the magnetic properties. Our experiment results confirmed that for the samples in which Au is in the metallic state as nanoparticles with ~5 nm diameter, as well as inthe alloy form, bonded with indium, the samples show ferromagnetism when embedded in an Al_2O_3 matrix without any thiol-containing organic capping. Our results suggest that ferromagnetism is an intrinsic property of Au nano-structures, which means that it is not necessary to incorporate Au-S bonds with organic coatings in order to observe this phenomenon. We believe due to the significant broken symmetry at the surface of the nanoparticles, holes are generated in *d* bands of the surface Au atoms. These holes are most possibly responsible for ferromagnetism in Au nanoparticles. The realization of magnetism in Au coupled with the lack of clear understanding of its origin makes the investigation of magnetism of diamagnetic metals ripe for further inquiry.

ACKNOWLEDGEMENTS

First, I want to thank Prof. Jeremiah Abiade, who has been my advisor since 2008. He taught me from the beginning how to be a more accomplished researcher. Equally important, he educated me on how to become a more responsible and consistent person. I will never forget the time when we conversed in his office about some of the problems I encountered when I first came to Virginia Tech. I also thank my co-advisor Prof. Jiefang Li. Her example of kindness and compassion will stay with me throughout my life. I also thank my committee members—Prof. Dwight Viehland, Prof. G-Q Lu, Prof. Mitsuhiro Murayama, and Prof. Gordon Yee—for their many contributions to this effort.

Thank you to my parents and grandparents who have always supported and encouraged me to study abroad in the U.S. Their happinessin my success helped me to complete this doctorate. I thank all my family members for motivating me to complete my dissertation.

I also would like to acknowledge those who contributed in various technical ways to this investigation. For starters, I acknowledge Dr. Mitsu Murayama at the Nano--scale Characterization and Fabrication Laboratory (NCFL) for helping me with TEM measurements. I also thank NCFL staff members, John McIntosh, Dr. Jerry Hunter, and Steve McCartney, for their contributions to this study. I must also extend my thanks to my fellow group members both at Virginia Tech and the University of Illinois at Chicago for their support. In particular, I am grateful to Dr. Ke-bin Low for the help with XPS.

Thank you to everyone who assisted me during my research — and I hope you know who you are. It is due to the talented, insightful, and diligent professors and colleagues at Virginia Tech and UIC that I have had this chance to receive the best education leading to my future career.

Table of Contents

TABLE OF FIGURES

LIST OF TABLES

CHAPTER 1:

INTRODUCTION

The main goal of this research was to understand the magnetic properties of nano-structured Au (gold) and Au-based materials, as well as the relationship between magnetic properties and other variables such as temperature. Gold has fully filled 5d orbitals with ten electrons in the 5d band. Further, the radius of d-shells is fairly large, which indicates less interaction among electrons and less exchange interactions (exchange interactions are short range, just a few Angstrom). Thus, Au is known to be inherently diamagnetic In bulk. However, it has been reported that Au shows magnetic properties when reduced to the nano-scale. [3, 4, 8-25] Specifically, our experimental results suggest that ferromagnetism is an intrinsic property for Au nano-structures, and that the presence of an organic layer like surfactant is not required to observe this phenomenon. The main goal of this research, therefore, is to understand whether the magnetism is dependent on the organic capping layers. Additionally, this study was designed to elucidate the relationship between magnetic properties and other variables, such as sample preparation temperature

To conduct this study, we employed pulsed laser deposition to prepare nano-structured gold of differing sizes and concentrations of Au versus total samplevolume. The morphology of the Au samples was characterized by transmission electron microscopy (TEM) and scanning transmission electron microscopy (STEM); the chemical composition was studied using X-ray photoelectron spectroscopy (XPS) and energy-dispersive X-ray spectroscopy (EDS). Further, we examined the magnetic and electronic environments of Au via a physical properties measurement system with vibrating sample magnetometer (PPMS with VSM), superconducting quantum interference device (SQUID), and X-ray absorption spectroscopy (XAS).

Our results show clear signs of magnetism for nanostructured Au as associated with the observation of a hysteresis loop with remanence. Magnetism was not observed in the

samples that did not contain Au. Since the morphology of Au in the samples was important for understanding the size effect on magnetism, cross-sectional TEM was utilized to understand the effect of size and distribution. Additionally, we used XPS to determine whether magnetic impurities were present in the samples, as well as bonding information for the Au NPs—specifically, if Au is metallic or alloyed with other elements, considering that XPS is also an element-specific magnetic testing techniques. XAS results provided direct evidence for magnetism in Au NPs or nano-structures, instead from the presence of impurities. The magnetic studies with XAS coupled by TEM, EDS and XPSsuggest same results.

We also determined that samples in which Au was in the form of an alloy with indium were confirmed to be magnetic without any organic capping layers. After ruling out the possibility of impurities—as well as other magnetization-inducing components in the samples such as ITO film and sapphire substrates—we attributed the observed magnetism to the existence of nano-sized gold. We believe that the size of the gold nanoparticles plays an important role in the existence of ferromagnetism. Other possible explanations for the magnetism have been proposed. It is know that symmetry affects properties via Neumann's principle [107]. A high fraction of surface atoms out of the total volume fraction will result in average properties appearing to have lower symmetry. This also includes the magnetic point group symmetry of Au nano-particles. Point groups are symmetry operation groups containing combinations of mirror planes, inversion centers and different types of rotation axes. Magnetic point groups have the additional operation of time inversion that accounts for the distribution of spin up/down, in addition to the distribution of lattice points. The magnetic point groups govern the anisotropy of the properties of magnetic materials. The lower symmetry at the surfaces also will allow electronic reconstructions, which could in fact alter the magnetic properties. For example, the surface Au atoms that have been partially filled 5 d electron band due to the appearance of 5 d holes generated by the asymmetry at surface. Nevertheless, the size effect which generates 5 d holes by increasing the density of states at the Fermi level, could also be linked to observed magnetism.

Future work should focus on study of the magnetism in other diamagnetic metals in nano scale, such as Ag or Cu, and compared to gold NPs trying to find out the true mechanism of magnetism in nanostructures of noble metals.

CHAPTER 2:

LITERATURE REVIEW

This chapter begins with a discussion of the various types of magnetism, as well as the origins of each type. Of particular importance to this study are the magnetic properties of Au, which displays such behavior when reduced to nano- particles featuring thiol-containing organic capping. Thus, this literature review will focus on magnetism in gold Nanoparticles (NPs) or thin films, as well as other Au-containing alloys. Finally, a summary of possible explanations for such phenomenon will be discussed at the end of this chapter.

2.1 Types of Magnetism

Magnetism, which originates from the spin or orbital moments of electrons in materials, can be distinguished according to the following types: ferromagnetism, paramagnetism, diamagnetism, antiferromagnetism, and ferrimagnetism. For instance, diamagnetism is characterized by a contrary response of the inner-atomic currents due to an external magnetic field. In contrast, paramagnetism corresponds to magnetic moments that result from electrons spinning around their own axes or the orbital contributions in the direction of external field. These and other types of magnetism will be discussed in the following sections.

2.1.1 Diamagnetism

In general, people use Spin-up and Spin-down to describe electron pairs that orienting in opposite directions. At the atomic scale, a pair of spin-up and spin-down electrons will result in a zero net moment. However, when an external magnetic field is applied, the orbits can shift to such an extent that a very tiny magnetic field is generated in opposition to the external field. The sum of such mechanism results in diamagnetism in bulk materials. As inferred by its name, diamagnetism is regarded as non-magnetism since it results in a repulsive effect. Specifically, diamagnetism describes a mechanism whereby a material reacts to an external magnetic field by creating a magnetic field in the opposite direction. Diamagnetism is not a permanent magnetism, since it is evidenced only when an external magnetic field is applied. Most organic compounds and noble metals—for example Cu, Ag

and Au—are diamagnetic in bulk. A typical diamagnetic moment versus magnetic field diagram using Au foil is depicted in Figure 1.

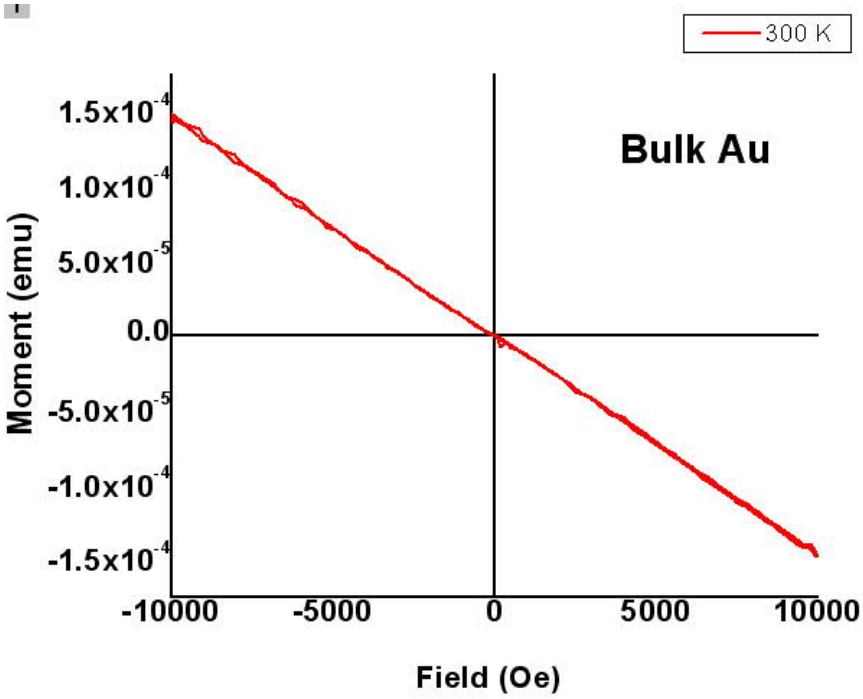

Figure 1: A typical diamagnetic diagram of bulk Au

2.1.2 Paramagnetism

Paramagnetism is associated with magnetic moments resulting from electrons that spin around their own axes or from the orbital contributions in the direction of the external field. According to the Pauli principle: No two electrons can have the same set of four quantum numbers n, l, m and m_s.. Therefore, for all other quantum numbers being the same on electron will have a positive spin and one will have a negative spin, which are also called spin up and spin down. To understand the spin paramagnetism, we assume an electron band to be divided into two halves, each of which is thought to be occupied under normal conditions by an identical amount of electrons of opposite spin. If we apply an external magnetic field to a free electron solid, some of the electrons having unfavorably oriented spins tend to change their field direction. Eventually the two band halves shift relative to each other until equilibrium and a common Fermi energy is reached. Spin paramagnetism is almost always field dependent, meaning that the alignment of moments disappears instantly when the external field is removed due to thermal vibration. Electron-orbit paramagnetism can be found in free atoms or dilute gases, as well as in rare earth elements and their salts and oxides.

It originates from the magnetic moments of orbiting electrons when the individual magnetic vectors of orbit correspond to the external field direction. Nevertheless, thermal fluctuations disturb this alignment. As a result, electron-orbit paramagnetism is temperature dependent. Also important to note is that ferromagnetism or ferrimagnetism (will be presented in next section) have a critical temperature, above which magnetic materials will become paramagnetic. This temperature is known as the Curie temperature for ferromagnetic and ferrimagnetic materials, but is known as the Néel temperature for antiferromagnetic materials.

2.1.3 Ferromagnetism, antiferromagnetism and ferrimagnetism

Ferromagnetism is a term that describes the magnetic status of materials characterized by spontaneous magnetization. An important distinguishing phenomenon of a ferromagnetic material is that it exhibits spontaneous magnetization, which has a net magnetic moment even in the absence of an external field. Ferromagnetic materials have a domain structure that minimizes total energy, which is illustrated in Figure 2.

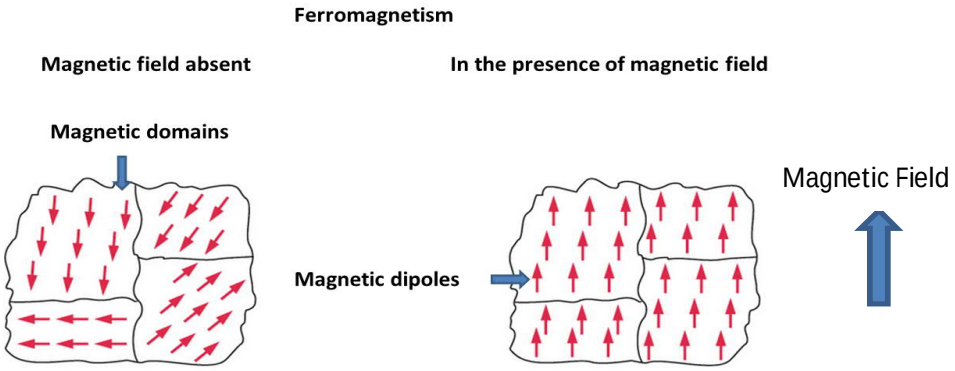

Figure 2: A schematic illustration of ferromagnetism with domain structures

A typical hysteresis loop of a ferromagnetic material is shown in Figure 3. As depicted, remanence—also known as remanent magnetization—refers to the magnetization that remains in a ferromagnetic material after an external magnetic field is removed. As such, it is a key feature providing magnetic memory in magnetic storage devices. In most cases, a higher remanence indicates an improved capacity to record magnetic information. Coercivity, which is also known as the coercive field, describes a magnetic field that reduces the

magnetic moment to zero after the sample is magnetized. The process is also called demagnetization. Thus, coercivity describes the resistance of a material against demagnetization. Another term of interest is “magnetic saturation,” which is a state of a magnetic material above which the point of magnetic moment will not change even when the applied field is increased, which is shown in Figure 3.

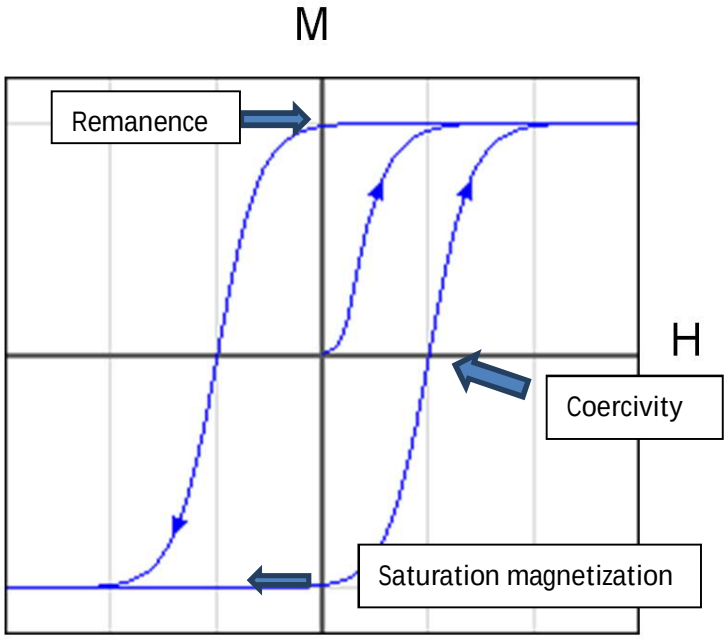

Figure 3: A typical hysteresis loop of a ferromagnetic material

Similar to ferromagnetic materials, antiferromagnetic materials possess spontaneous alignment of moments below the Curie temperature. However, due to their specific crystal structure, the participating neighboring atoms in antiferromagnetic materials are aligned in an antiparallel direction, which cancels out each other—the net result being a zero magnetic moment. The third kind is called ferrimagnetism. In this instance, participating neighboring atoms have two opposite directions; however, the net moment is non-zero. Ferrimagnetism are also characterized by spontaneously aligned moments below the Curie temperature. In most cases, ferromagnetic materials are constituted by two or more than two sub-lattices. Schematic representations for both ferrimagnetic and antiferromagnetic materials at the atomic scale are shown in Figure 4.

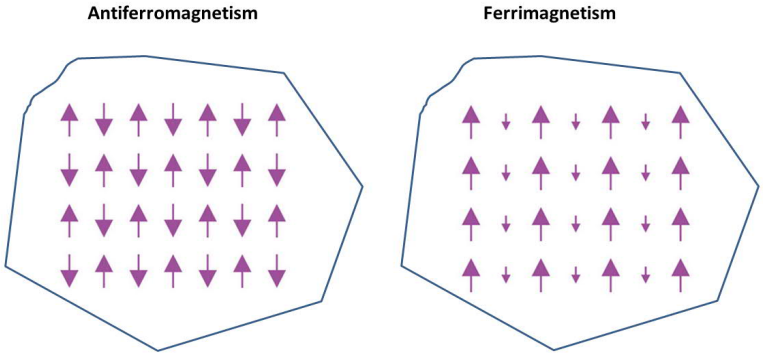

Figure 4: The magnetic moments at the atomic scale for antiferromagnetism and ferromagnetism materials.

2.1.4A Brief overview of magnetism

2.1.4.1 Exchange interactions

The basic origin of ferromagnetism is associated with the spontaneous magnetization produced by a parallel alignment of spins. German theoretical physicist Werner Heisenberg first proposed this exchange interaction in 1928. As is well known, two nearby magnetic dipoles will tend to align in opposite directions. At short distances, however, the exchange interaction is much stronger than the dipole-dipole magnetic interaction. Stoner suggested that the interaction energy $W_{i,j}$ between two nearby spin s_i and s_j is determined by the following equation:

$$W_{i,j} = -2Js_i * s_j$$

Where J is the exchange integral:

$$J = \int \varphi_a(1)\varphi_b(2)\varphi_a(2)\varphi_b(1)[\frac{1}{r_{ab}} - \frac{1}{r_{a2}} - \frac{1}{r_{b1}} + \frac{1}{r_{12}}]dt$$

Where the exchange integral contains the forces between nuclei a and b, the forces between two electrons 1 and 2, and the interactions between the nuclei and their neighboring electrons. If $J > 0$, when the distance between two electrons r_{12} is small, or a small radius of d orbits r_{ab}, the energy between two parallel spins reaches its minimum. The exchange interaction J is a parameter that is distance-dependent. Exchange interaction is short range among only neighbor spins, but such short range interaction can be found in whole magnetic system.. The

overall effect of an exchange interaction results in ferromagnetism in bulk materials, such as Fe Co and Ni.

2.1.5 Superparamagnetism

In small ferromagnetic or ferrimagnetic nanoparticles—e.g., when their particle size is smaller than a certain critical diameter—magnetization can randomly flip direction under the influence of temperature. As a result, when the time used to measure the magnetization of the nanoparticles is much longer than the flipping time which is also called Néel relaxation time, their magnetization appears to be in average zero. It should be noted that the transition from magnetic to superparamagnetic is different from the Curie transition, whereby ferromagnetic or ferrimagnetic materials become diamagnetic above the Curie temperature. In contrast, superparamagnetism occurs below the Curie temperature of a given material. When the size of nano-structures is less than a critical diameter, which can vary from 3 to 50 nm depending on the material, the nano-structures can be single domain, which means that the nano-structure consist of a single magnetic grain from a collection of all the moments of atoms within. A typical MH loop for the superparamagnetic nano-material nickel (Ni) is shown in Figure 5.

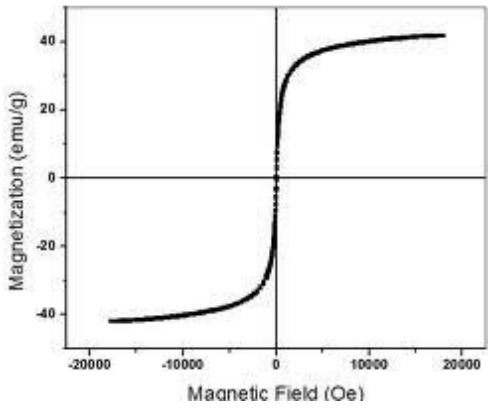

Figure 5: A typical superparamagnetic curve from the LORE lab for Ni nanoparticles

2.2 Properties of Gold

Gold is one of the most valuable metals on earth, with an atomic weight of 197 amu; the concentration of free electrons in gold is 5.90×10^{22} cm^{-3}. Gold atoms have fully-filled 5d electron shells and only 1 electron on the 6s band. As discussed above, the fully filled 5d

bands will generate a field in opposition to an external magnetic field; as a result, gold is diamagnetic in the bulk. Recently, however, it was suggested [3, 4, 8-25] that gold might be magnetic when its dimensions are reduced to the nano-scale. An overview of the recent results is given in the following sections.

2.3 Ferromagnetism in Au Nano-structures

It has been suggested that the size of Au plays an important role in magnetic properties. Specifically, gold—which again is diamagnetic in bulk— has been reported to be ferromagnetic at the nano-scale, both at room temperature and low temperature. The majority of work in this area has focused on thiol-capped gold nanoparticles (NPs), resulting in a number of published reports [3, 4, 8-25] . Later, Hori and Yamamoto described the diameter dependence of ferromagnetic spin moment in Au nano-crystals. Figure 6 illustrates the relationship between diameter (nm) and magnetization using Au nanoparticles.

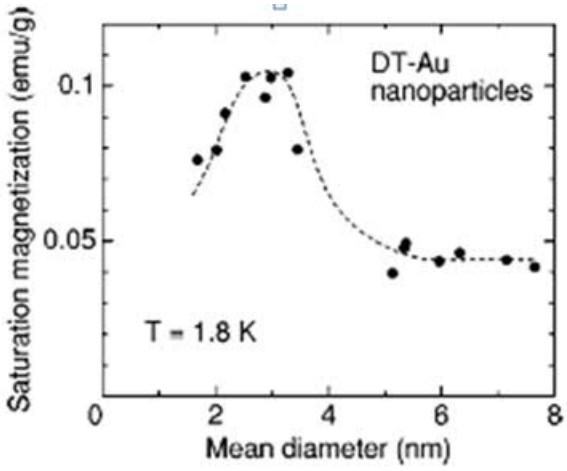

Figure 6: Magnetization versus diameter of Au NPs [26]

The following section reviews the ferromagnetism of thiol or other organic layer capped Au NPs, which have been widely studied. Additionally, other forms of Au-based magnetic nano-structures, including Au thin films and Au NPs without any coating, will be further discussed in this section. First, is a review of the thiol-capped Au NP systems, which will be divided into two parts based on type of magnetism. Second, is a discussion of magnetism in other Au-based nano-materials, such as thin films and NPs, as well as magnetism in other nano-scale noble metals.

2.3.1 Ferromagnetism in thiol-capped Au nano-structures

Crespo et al. [3, 8, 24, 25, 27-39] suggested that ferromagnetism in thiol-capped gold NPs results from a charge-transfer at the interface of the Au and S atoms, which induces surface permanent magnetism with respect to the diamagnetism of bulk Au. They also concluded that thiol bonding induces not only localized holes and lattice expansion, but also permanent magnetic moments associated with the spin of extra *d* holes localized near the Au-S bonds. As a result, the strong spin-orbit coupling of Au with high local anisotropy results in freezing the magnetic moments.

In contrast, Hori and colleagues [1, 12, 26, 40-44] performed X-ray magnetic circular dichroism (XMCD) on similar gold thiol-capped NPs. They observed that the sign of the XMCD signal reversed when the magnetic field direction was changed, which supports their claims that the observed magnetic signal truly originated from the gold. Detailed mechanism of XMCD will be discussed in section 3.6. Moreover, they reported that asymmetry in the L_3 ($2p_{3/2}$ to $5d_{5/2}$ and $6s_{1/2}$) and L_2 ($2p_{1/2}$ to $5d_{3/2}$ and $6s_{1/2}$) peaks of the XMCD spectra indicated that the Au 5*d* electrons contain a considerable orbital moments. Based on these results, the researchers concluded that the large ratio of the number of atoms on the surface in comparison to the number in the core is the cause for the ferromagnetic polarization. It has been predicted theoretically that ferromagnetic spin polarization could take place in 4 *d* and 5*d* transition metals with reduced coordination. Both hypotheses will be discussed in detail in Sections 2.3.1.1 and 2.3.1.2.

2.3.1.1 Hole-induced ferromagnetism in thiol-capped Au NPs

Quite a few studies [25, 27-39] have reported that ferromagnetism in thiol-capped gold NPs results from a charge transfer at the interface of the Au and S atoms. Research has also confirmed that thiol-bonding induces not only hole localization and lattice expansion, but also magnetic moments associated with the polarized spin, which is localized near the Au-S bonds. As a result, the strong spin-orbit coupling of Au with a high local anisotropy is believed to result in freezing the magnetic moments.

Figure 7 [3] depicts moment vesus magnetic field for both an Au-SR sample (thiol-capped sample) and an Au-NR non-thiol capped surfactant sample at both 5 K and 300

K. NPs dispersed by a surfactant (the Au-NR sample) exhibited diamagnetic behavior, which is very similar to that of bulk gold. In contrast, thiol-capped gold NPs (the Au-SR sample) show signatures of ferromagnetism on this moment versus magnetic field (MH) diagram. The samples had coercivity of 860 Oe at 5 K that decreases to 250 Oe at room temperature. Additionally, saturation was not observed at either 5 K or room temperature.

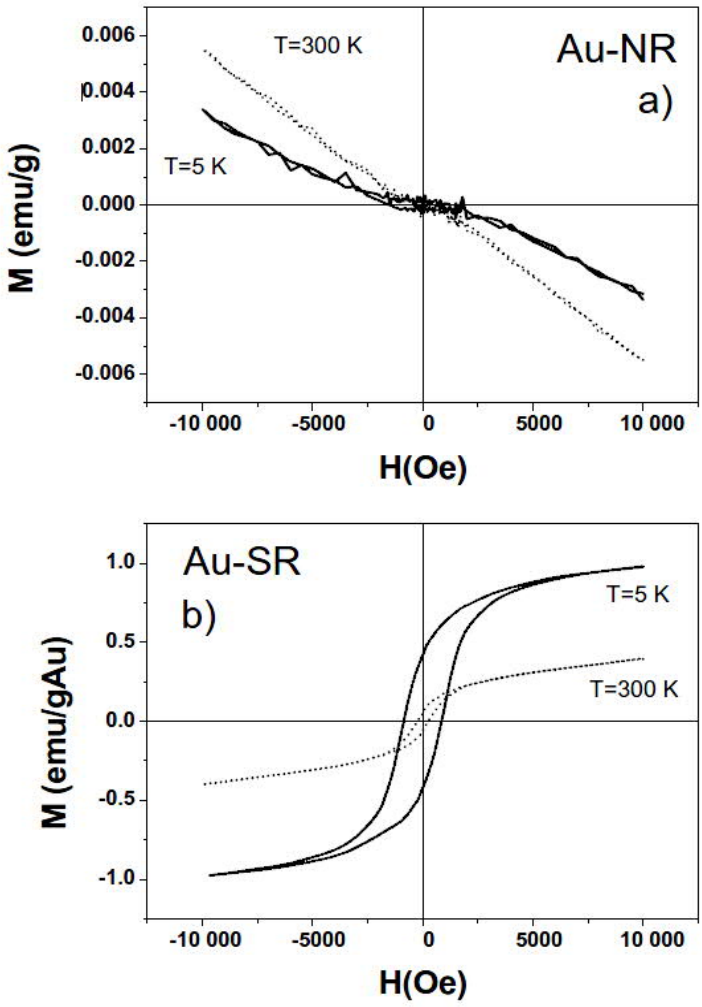

Figure 7: Magnetization curves of gold nanoparticles stabilized by means of a non-thiol surfactant, Au-NR (a), and hysteresis loops corresponding to the thiol-capped Au NPs, Au-SR (b), at 5 and 300 K. For the Au-SR sample, the magnetization is given in emu per gram of gold. From reference: [3]

Figure 8 shows X-ray absorption near edge structure (XANES) results of the Au-L_3 edge for the two nano-structured samples (Au-NR and Au-SR), together with bulk Au. It is understood that the large area under the white line in Figure 8 indicates an extremely large

charge transfer from gold to sulfur atoms in the Au-SR sample, which has also been verified in the literature [4]. More details about X-ray analysis featuring XMCD and XANES will be discussed in Section 1.2.4.

It has also been reported [6] that ferromagnetism has been observed for 5 nm dodecanethiol-capped Au NPs. In this instance, the researchers reported a blocking temperature (T_B) at 50 K. Transmission electron microscopy (TEM) was performed on the selected sample; subsequent TEM images (not shown) have indicated that those Au NPs were a spherical shape and had an average diameter of 4.8 nm.

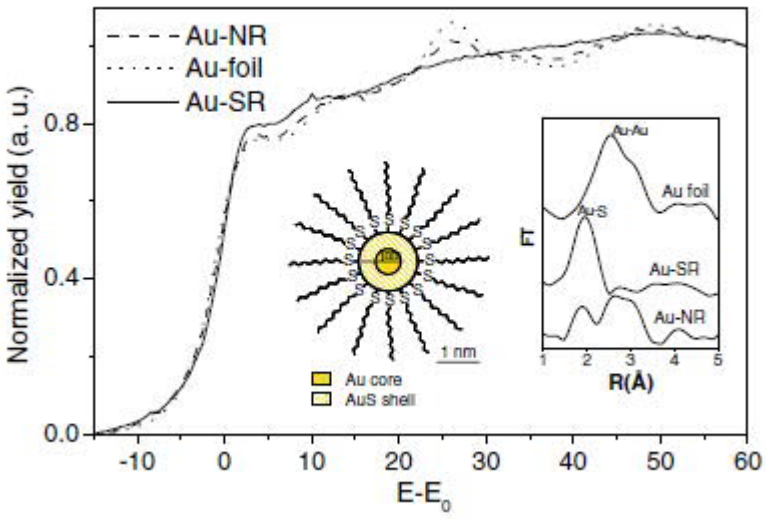

Figure 8: Au-L3-edge XANES spectra for the two different gold NPs compared to bulk gold.[4]

It should be noted that magnetic susceptibility is strong temperature dependentin this case compared to those samples with moments at room temperature [3,4]. In Figure 9a (sample S1) and Figure 9b (sample S2), one can determine the value of susceptibility (M/H) when the magnetic field (H) is set at 500 Oe for the field cooling and zero field cooling process. The sample S2 is diamagnetic at both low and high temperature with a susceptibility $\chi d = -5.65\times10-7$ emu/g Oe, which indicates critical size exists for observing magnetism in Au NPs. In contrast, there was a bifurcation of the ZFC and FC curves at the blocking temperature around 50 K in the smaller sample S1, which indicates that sample S1 displays

magnetic properties of typical magnetic nanoparticles based on the M-T curve.

Due to thermal fluctuations at the blocking temperature, the exchange bias ***J*** will approach zero when the blocking temperature is reached. In addition, researchers have observed an electron magnetic resonance (EMR) line [4], which exhibits temperature-dependent properties—thereby confirming blocking for $T<T_B=50K$. These experimental results led the authors to believe that in addition to the charge transfer mechanism between surface Au atoms to the capping organics, the surface effect due to small size isbelieved to be the cause of the observed magnetism. The existence of blocking phenomena indicates that those Au NPs can possibly exhibit behaviors similar to those of traditional magnetic NPs.

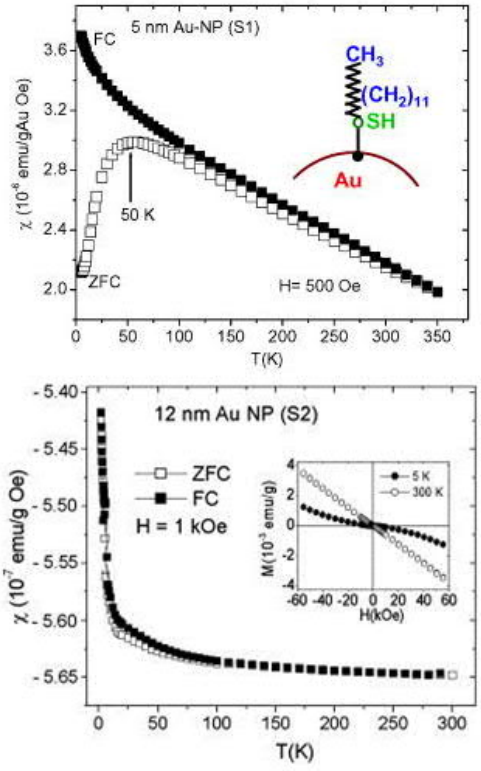

Figure 9: 9a (top): Magnetic susceptibility χ (M/H) vs T at H = 500 Oe for the ZFC and FC modes for S1. The inset shows representation of Au–SH bond to DT.

9b (bottom): Susceptibility vs. T at H = 1 kOe for S2. The inset shows the M vs H at 5 and 300 K for sample S2. From Reference [6].

Solid matrix materials such as ceramics and polymers have also been used to the study the magnetic properties of thiol capped Au NPs. For example, Yamamoto et al. observed ferromagnetismin polymers embedded with gold nanoparticles [8]. The permanent magnetism of certain Au NPs has implications for practical applications that require frozen magnetic moments, such as magnetic memory devices or creating patterns of stable magnetic fields. In another study, de la Venta et al. [8] prepared dodecanethiol-capped Au nanoparticles embedded in a polymeric matrix. TEM was used to generate bright field images of dodecanethiol-capped Au NPs displaying a mean diameter of 3–4 nm (Figure 10).

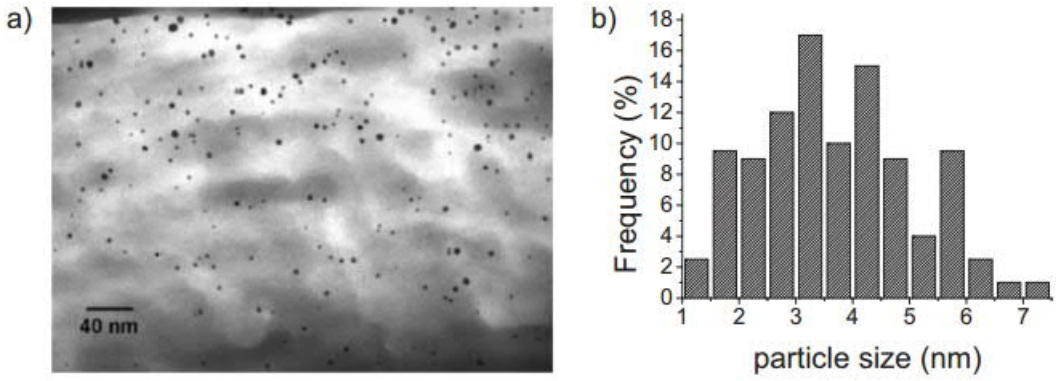

Figure 10: a) Bright-field transmission electron microscopy image, and b) particle size distribution, of 4 wt % Au-NP–PE film.[8]

It should also be mentioned that the observed magnetic moments of thiol-capped Au NPs is attributed to the interaction of surface Au atoms with capping S atoms, which induces 5d holes in the Au NPs. Therefore, the introduction of a polymer matrix could possibly change this mechanism since it can prohibit or alter the formation of Au-S bonds. In fact, Figure 11apresentsanMH diagram of thiol-capped Au NPs in a polymeric matrix tested at 300 K. The polymeric matrix exhibits diamagnetism like other solid or ceramic substrates. However, the diamagnetic background must be subtracted from the total signal to determine magnetic data for the Au NPs. The magnetic signal from Au in Figure 11a is saturated around 4000 Oe. Although there is only a small amount of Au in the polymeric matrix, the magnetic

signal from the Au is clearly shown, and the diagram is a combination of magnetic and diamagnetic signal below 4000 Oe. Thiol-capped Au NPs lacking a polymeric matrix have been prepared for comparison; these show similar magnetic moment values. As shown in Figure11band 11c, the coercivity of Au NPs is 40 Oe at 5 K and about 20 Oe at 300 K 。

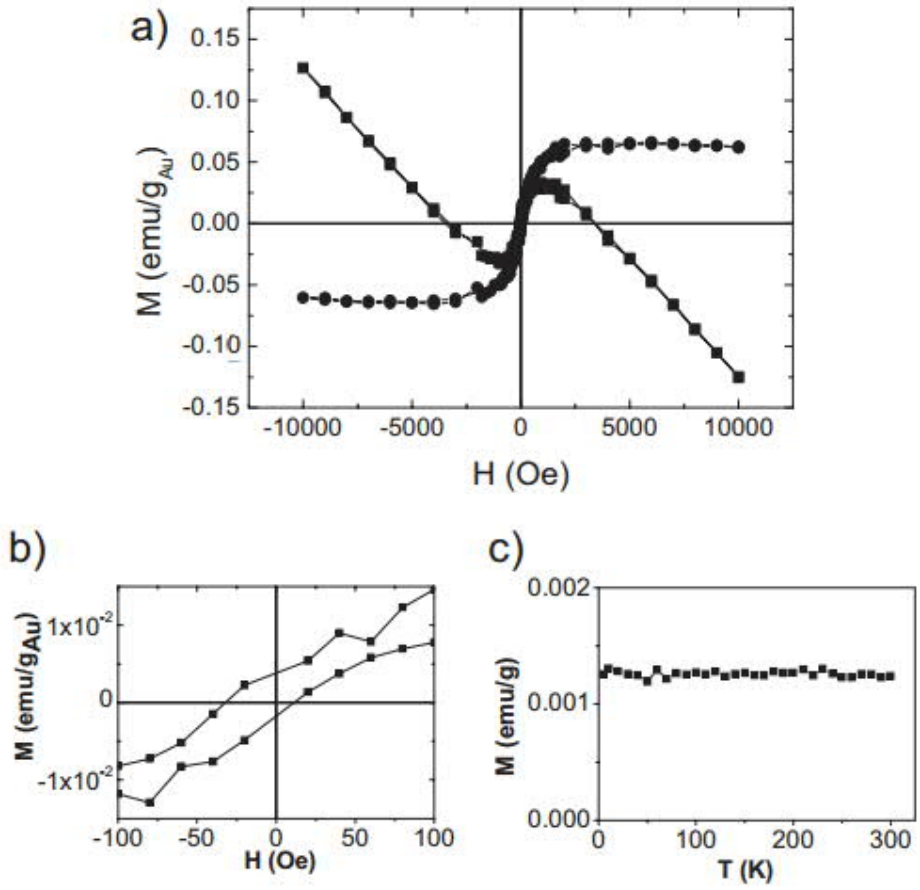

Figure 11: a) the MH diagram of thiol-capped Au NPs in the polymeric matrix tested at 300 K, b) the coercivity of Au NPs is 40 Oe at 5 K, and c) the moment versus temperature diagram of thiol-capped Au NPs from 5 K to 300 K [8].

2.3.1.2 Intrinsic ferromagnetism in thiol-capped Au NPs

Researchers have also argued that magnetism in Au is an intrinsic property of nano-structured gold. For example, Hori et al. [1, 26] first observed Au nanoparticles that exhibited ferromagnetic spin polarization on the surface and attributed it to the “Fermi hole effect.” (See appendix A) The researchers noted that certain Au NPs exhibited diameter dependence in magnetization. XMCD was used to confirm the ferromagnetic spin polarization of the Au nanoparticles. As an offshoot of the Pauli Exclusion Principle, the

‘‘Fermi hole effect’’ with one free surface election is proposed to impact magnetism. In bulk Au, the spin correlations in 5d bands with up and down spin cancel each other out, and the net amount of spin polarization is zero. Nevertheless, the ratio of Au surface atoms in NPs is much higher than in bulk, and the imbalance near the surface becomes significant compared to bulk, which can be regarded as a discontinuity or defect in the NPs. Okazaki and Teraoka [45, 46] investigated magnetism in diamagnetic thin films such as noble metals. When the diameter of Au NPs is small enough to generate considerable anisotropy on the surface, the net of spin up and spin down is not zero, which results in imbalance. This surface imbalance can possibly induce ferromagnetism in most diamagnetic metal NPs or thin films.

X-ray magnetic circular dichroism is a technique that can detect magnetism from a specific element, which is known as element-specific magnetization (ESM). For Au NPs, we can focus on the L_3 band of gold’s X-ray absorption band by measuring the difference between the up and down spin at the Fermi level. Compared to SQUID or PPMS, which are ensemble magnetometry techniques, XMCD can focus on the Au element only and rule out any contributions from magnetic impurities such as Fe or Ni.

Figure 12 shows the X-ray absorption spectroscopy (XAS) and XMCD spectra from an Au sample as reported by Crespo et al. [1]. The applied field was set at 10 T with a low temperature of 2.6 K to freeze all the possible moments from the Au sample. Both L_3 ($2p_{3/2} \rightarrow 5d_{5/2}, 6s_{1/2}$) and L_2 edge ($2p_{1/2} \rightarrow 5d_{3/2}, 6s_{1/2}$) were examined and plotted in Figure 12. As depicted, when the direction of the magnetic field was reversed, the XMCD signal reversed with the field. This finding provides direct evidence of ferromagnetism in Au that cannot be attributed to any impurities since we focus on L_3 edge of Au. However, these samples were also thiol-coated nanoparticles.

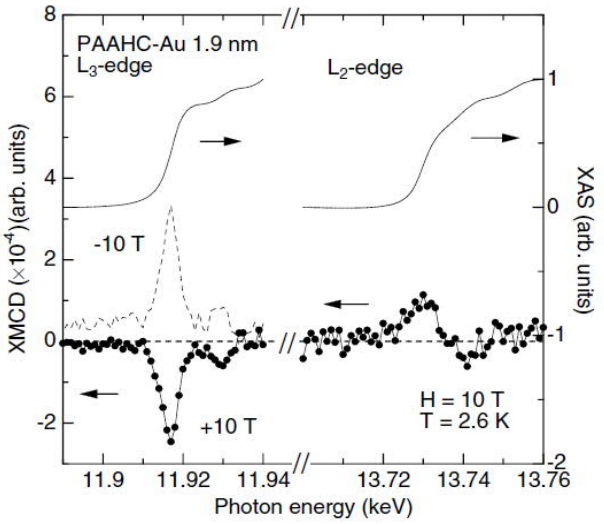

Figure 12: X-ray absorption spectroscopy (XAS) and XMCD spectra of Au[1].

2.3.2 Ferromagnetism in other Au-based nano-structures

In addition to observing ferromagnetism in the thiol capped Au NPs, Hernando et al. [7] also reported that ferromagnetism was found in thiol-capped gold thin films. Surface electrons were believed to generate considerable surface anisotropy not only in the Au thin film but also in the thiol-capped Au NPs. The spin-orbit interaction induced orbital moment at the surface, which is responsible for the surface anisotropy. As illustrated in Figure 13, the top magnetization curve (c) represents when H is perpendicular to the surface, while the lower magnetization curve (d) depicts when H is parallel to the surface. Hernando concluded that the Au (111) surface is the orientation perpendicular to the surface with a planar mass density of $2x10^{14}$ atoms/cm^2, and with magnetic moment of 100 μ_B per surface atom. Additionally, these studies indicate that the strong spin-orbit interaction at the gold surface [47-49] induced the giant orbital moments in the Au nano-structure.

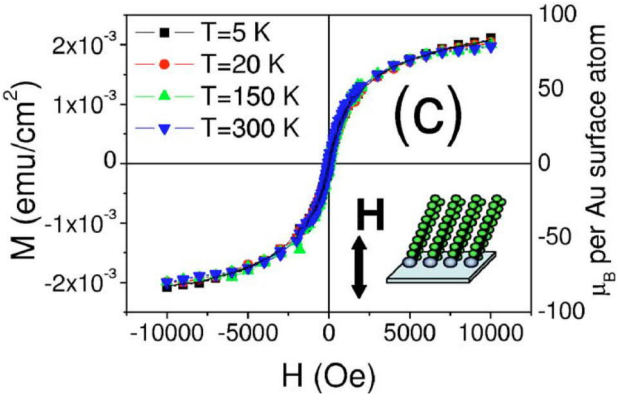

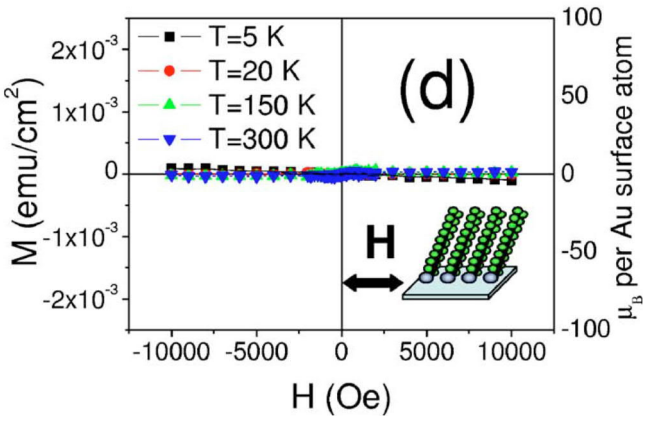

Figure 13: Magnetization curves for an Au thin film deposited on a glass substrate.[7]

2.3.3 Ferromagnetism in other noble metal nano-structures

Recently, Teng et al. [2] investigated the magnetic properties of ultrathin Gold/Platinum Au/Pt nano-wires. Specifically, they produced $Au_{25}Pt_{75}$ and $Au_{48}Pt_{52}$ alloyed ultrathin nano-wires of less than 3 nm in diameter using a wet chemistry approach at room temperature. Their results confirmed that both the $Au_{25}Pt_{75}$ and $Au_{48}Pt_{52}$ nano-wires were alloyed with a structure of Pt abundant shell and Au abundant core. The unoccupied *d* sites in the Au atoms of $Au_{48}Pt_{52}$ show a decrease in amount compared to the Au foil in bulk. However, as shown in Figure 14, the L_3 edge of Pt has a different trend change in $Au_{48}Pt_{52}$ compared to the Pt foil. This result is not surprising given that the *d* charges migrate from the Au sites to the Pt sites during alloy formation, which creates the *d* holes in Au atoms and d electron gain in Pt atoms.

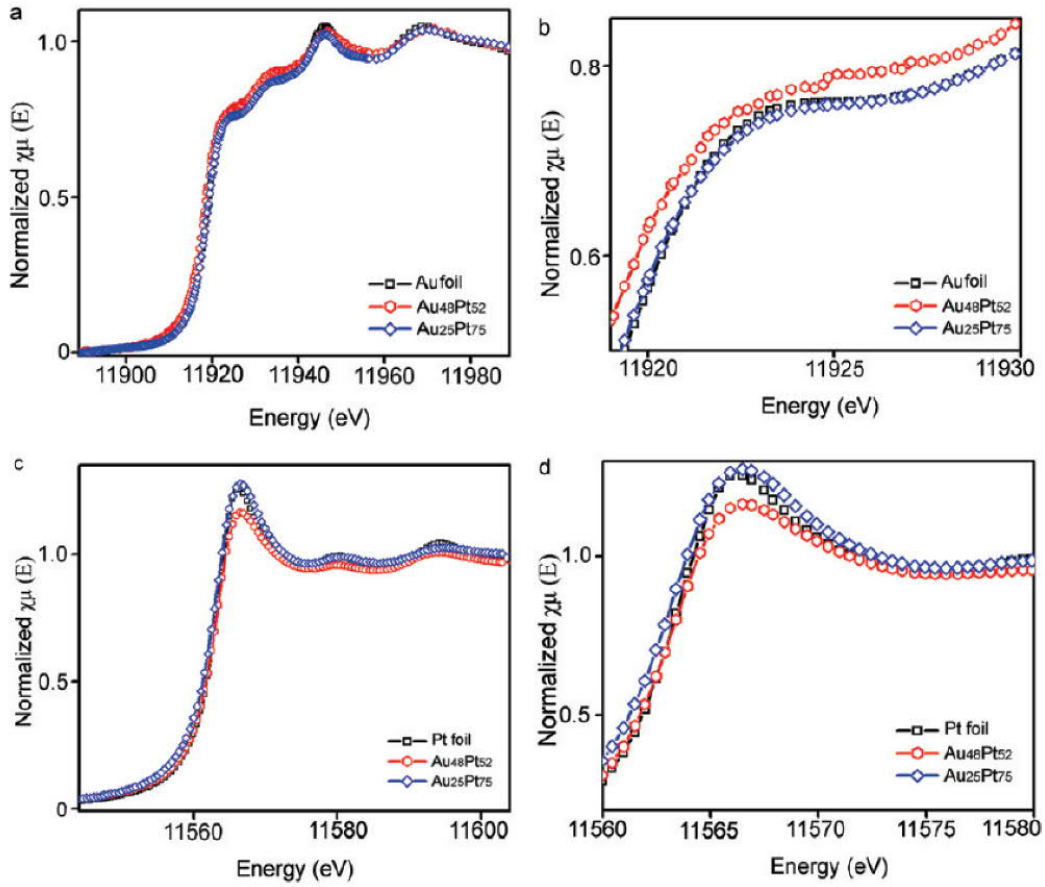

Figure 14: XANES spectrum of as-made $Au_{48}Pt_{52}$ (nano-wires),$Au_{25}Pt_{75}$ (nano-wires), Pt (foil reference), and Au (foil reference)[2].

Ferromagnetism has also been reported in palladium (Pd)-based nano-structures. In fact, Hori et al. [5] described magnetism in Pd and Au nanoparticles as early as 1999. In their investigation, the researchers used the wet chemical method to prepare Au and Pd NPs using the organic agent, poly-N-vinyl-2-pyrrolidone (PVP). The mean sizes of both varieties of NPs were approximately 2.5 nm in diameter. They observed a value of $18\mu_B$ on the saturation magnetization of Pd NPs, compared to the observed spin polarization of $22\mu_B$ for the Au NPs, as shown in Figure 15. Based on these outcomes, they concluded that an extension of the Stoner's enhancement took place at the nano-scale level-—in other words, there is a special mechanism that occurs at the nano-scale, and that this nano-polarization effect on the surface or in NPs can be a universal effect.

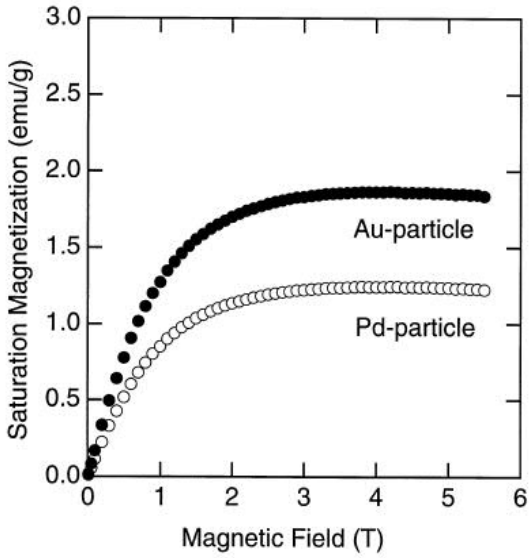

Figure 15: Saturation magnetization of Au and Pd nanoparticles [5].

At the same time, Taniyama et al.[50] confirmed the presence of ferromagnetism in Pd NPs when the diameter of the particle was less than 7 nm. Analogous to Crespso et al.'s [1] explanation of thiol-capped Au NPs, Taniyama and coworkers indicated the presence of a surface anisotropy, and that only the surface monolayer is magnetic. This causes a change in crystal structure from a face-centered cubic (fcc) structure in bulk into an icosahedral structure at the nano-size level—which accounts for the size of the ferromagnetism. They also reported an increase in ferromagnetic susceptibility when the size of NPs decreased from 9.9 nm to 5.9 nm.

In 2006, Litrán et al. [108] compared ferromagnetism in palladium NPs with different capping organic layers. Organic molecules with weakly interacting inter-alkylammonium salts (Pd-NR4), as well as strong bonding organics such as alkane-thiol molecules (Pd-SR1), have been used to form covalent bonds to Pd NPs. The average particle sizes of Pd-NR4 (C4) and Pd-NR4 (C12) were 2.4 and 2.1 nm, respectively, whereas the Pd-SR1 NPs were approximately 1.2 nm on average, and the SR2 NPs were in the range of 2.3 nm. The structures of each capping system are shown in Figure 16. The magnetic property has been confirmed by MH diagram in Figure 17.

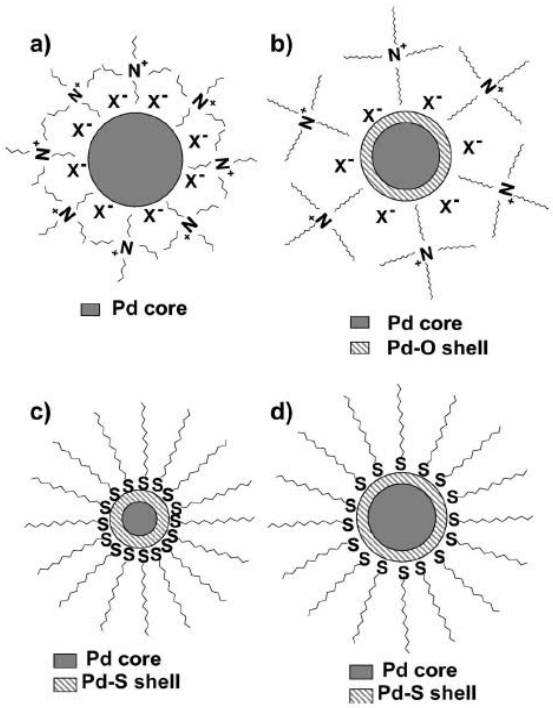

Figure 16: Saturation magnetization of Pd and Au nanoparticles with a diameter of 2.5 nm. Black and open circles represent the Ms of Au and Pd, respectively.[108]

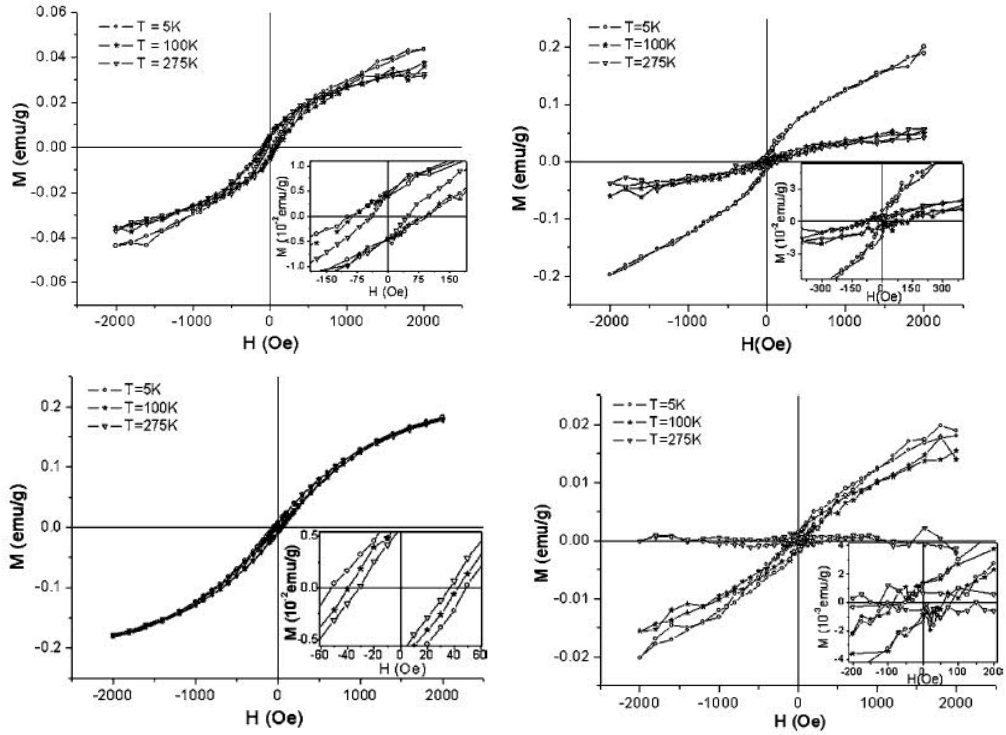

Figure 17: Hysteresis loops of Pd-NR4 (C4) [left top], Pd-NR4 (C12) [right top], Pd-SR1 [left bottom] and Pd-SR1 [right bottom] from reference Litrán et al. [9].

In 2008, Oba et al.[51] linked the ferromagnetism they observed to the stress in Pd nanoparticles. They focused on the influence of temperature and crystal structure and resulting defects on the ferromagnetic behavior. The temperature-dependent saturation magnetization is shown in Figure18 (a), while a diagram depicting saturation magnetization changing with lattice stress Δε is shown in Figure18 (b). They claimed that palladium should show varying magnetic properties as a result of changing structure and related defects. Moreover, the authors reported that due to size effects, the lattice expansion related stress (Δ ε) can produce local anisotropic strains in the crystal lattices of Pd NPs. This lattice stress can alter the symmetry, which may produce magnetic anisotropy and modify electronic states to induce ferromagnetism.

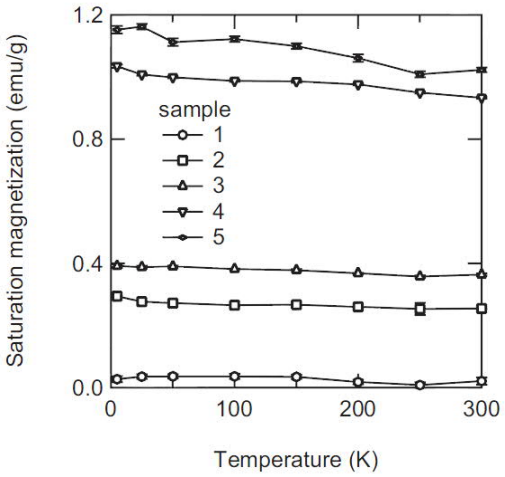

Figure 18(a): Temperature dependence of saturation magnetization from the literature [51].

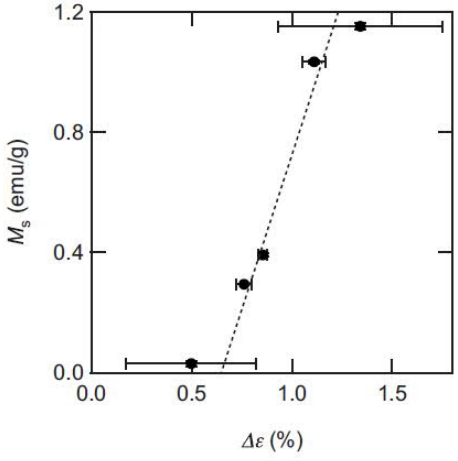

Figure 18(b): Saturation magnetization as a function of Δ ε from the literature [51].

In 2010, Goikolea et al. reported ferromagnetism in three dodecanethiol-capped Silver

nano-particle samples, with average diameter distributions ranging from 2.1 nm to 2.3 nm. They asserted that the observed ferromagnetism resulted from the chemical or physical bonding between surface Ag atoms and organic layers when those surface atoms were exposed to dodecanethiol capping.

An EXAFS spectra of several Ag samples, using Ag foil for comparison, are shown in Figure 19. Since the curves associated with the dodecanethiol-capped Ag nanoparticles did not fit with that of Ag foil (the dotted black line), this implies that the S-Ag bonds on the sample surface are responsible for the ferromagnetic results. The EXAFS spectrum for the Au NPs from reference [4] is also shown Figure 19. The similarity of the curves led researchers to suggest that the true mechanism for ferromagnetism in both Au and Ag NPs is very similar, which has been attributed to the bonds from Ag or Au surface atoms to the S atoms of the dodecanethiol, thereby contributing to the enhanced ferromagnetic properties of thiol-capped NPs by the Ag-S bonds at surface.

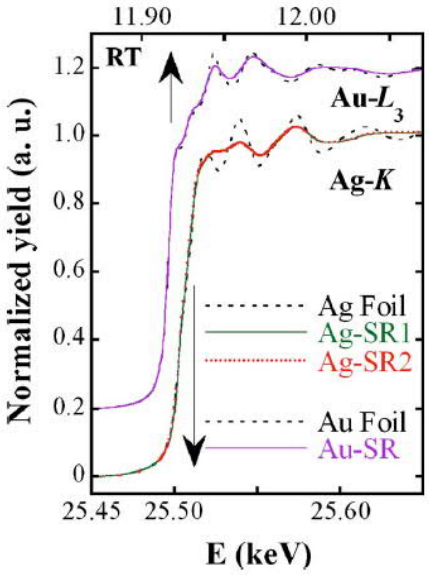

Figure 19: Ag K-EXAFS spectra for samples Ag-SR1, Ag-SR2, and a Ag foil together with Au L_3-EXAFS spectra obtained for previously reported ferromagnetic Au-thiol NPs

2.3.4 X-ray magnetic circular dichroism (XMCD)

X-ray magnetic circular dichroism (XMCD) represents the difference of two X-ray absorption spectra (XAS) obtained in a magnetic field—where the first is obtained using left circularly polarized X-ray, and the other uses right circularly polarized X-ray. XMCD is an

element-sensitive measurement that studies two different spectrums to obtain the magnetic properties of atoms from desired elements. In the case of noble metals, the spectra mainly show two broad L_2 and L_3 peak, reflecting the width of the empty *d*-bands.

Zhang and Sham [4] reported X-ray Absorption Near Edge Structure (EXAFS) results for the 4.0, 2.4, and 1.6 nm gold NPs showing lattice contractions of 0.7%, 1.1%, and 1.4%, respectively, relative to the bulk. Figure 20 illustrates the XANES spectrum of Au at the L_3 edge of the Au foil and three NP samples from their research. Overall, the shape and the pattern of the curves of the three different Au NPs are similar to that of the Au foil—although there is a broader range and peak broadening for the NPs compared to the bulk. Such phenomena can be understood because although Au NPs have a similar chemical state, they differ in electron distribution, as shown in the EXAFS curves. Since we know that the L_3 peak is associated with a electron transition from $2p_{3/2}$ to $5d_{5/2, 3/2}$, the peak height at the L_3 edge is proportional to the intensity of the resonance at white line, which is associated with the unoccupied holes in 5d band. This figure also shows that the researchers found an intensity increase at the L_3 edge according to the following sequence: Au foil<4.0 nm NP < 2.4 nm NP < 1.6 nm NP [4]. This means that the 1.6 nm NPs have the highest 5d hole density, in comparison to the lowest in the gold.

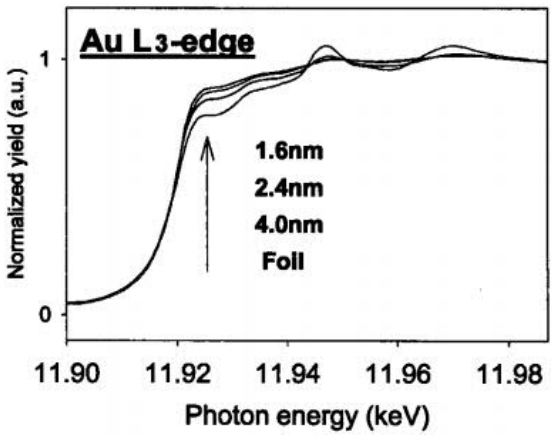

Figure 20: Au L3-edge XANES of the NP samples and gold foil.[4]

In addition, XPS studies were performed on the samples shown in Figure 21. Previously, it was believed that there were a significant number of $_d$ holes in Au NPs compared to bulk Au, which is indicated by the $4f_{7/2}$ peak of Au shifting to higher binding energy. Additionally, similar to XANES results, there also exists a peak broadening in the

NPs when their size decreases, which is associated with symmetry disruption due to an increase in the surface/core ratio of Au atoms. It is also possibly associated with the emergence of 5*d* holes in NPs compared to the bulk gold.

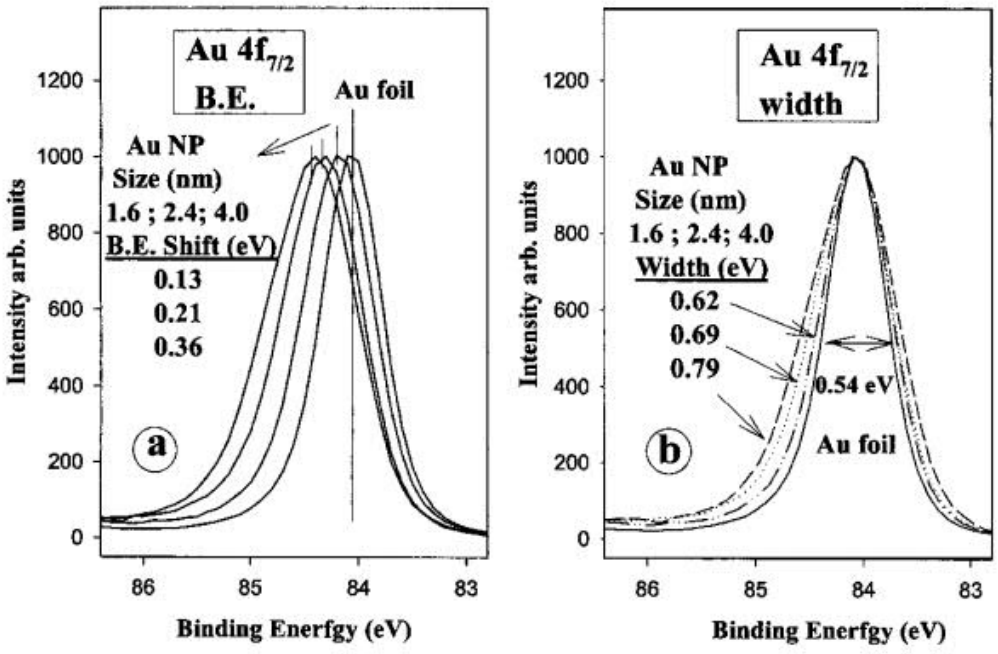

Figure 21: (a): Au 4f XPS spectra of the three NP samples and bulk gold (b): same as (a) except that the 4f peaks of the NP samples were aligned with the bulk gold. The binding energy shifts and the linewidths are also shown.[4]

The so-called "size effect" has been raised to explain the lattice contraction of Au NPs compared to bulk Au. X-ray absorption spectroscopy has already confirmed that both uncapped Au NPs and thiol-capped Au NPs have a significant reduction in lattice constant compared to bulk Au. Specifically, researchers have indicated that lattice reduction is about 2% for uncapped Au NPs and less than 1.5% for their thiol-capped counterparts [4]. Moreover, research has shown that this finding is also related to the size of the NPs, i.e., smaller nanoparticles will generate a greater reduction in the lattice constant. As previously discussed, the Au-S bond, which can induce 5*d* holes in Au surface atoms by means of charge transfer at the interface, is also supported by the whiteline at the L_3 edge. The peak at the L_3 edge for weakly interacted organic capped Au NPs is very close to that of bulk Au; in contrast, the L_3 edge associated with strongly capped Au NPs is much higher in intensity than that of bulk gold. This process is accompanied by a charge transfer from the Au atom to S, which can

deplete electrons in the 5d band in surface Au atoms. As a result, in addition to the symmetry disruption due to an increase in the surface/core ratio of Au atoms, the d holes on the surface of Au NPs, which is induced by Au-S bonds, play an important role in generating surface magnetism in thiol-capped Au NPs.

Yamamoto et al.[40] published significant experimental results using XANES and XMCD, respectively. The XMCD results from Yamomoto and coworkers are shown in Figure 8. Figure 22 depicts X-ray absorption spectroscopy (XAS) and XMCD spectra for Au [40]. Yamamoto et al. established the testing field at 10 T with a low temperature of 2.6K to freeze all possible moments detected for the Au. Both L3 ($2p_{3/2}$ to $5d_{5/2}$ and $6s_{1/2}$) and L2 edge ($2p_{1/2}$ to $5d_{3/2}$ and $6s_{1/2}$) have been examined and plotted in Figure 8. A negative peak at the L3 edge and a positive one at the L_2 edge can be seen in the XMCD diagram. These findings confirm that when the direction of the magnetic field is reversed, the XMCD signal reverses with the field, as illustrated in Figure 24. This finding on the L_3 edge of Au also provides direct evidence for ferromagnetism in Au in the current study . By the method of sum rules [52, 53], the ratio of orbital moment versus spin moment wasfound to be 0.145, which is significantly larger than those in which the spin moment is dominant, such as 3d transition metals. It is needed to mention that sum rule is actually x-ray absorption sum rule, which links the total intensity of the L_3 and L_2 resonances with the number N of empty d states (holes) of tested element. The d valence shell of gold can hold up to 10 electrons which are filled into band states up to the Fermi level and the number of filled states is therefore 10 -N. The x-ray absorption sum rule is based on dipole selection rules and the d-shell properties are best probed by L-edge absorption studies (2p to 3d transitions).

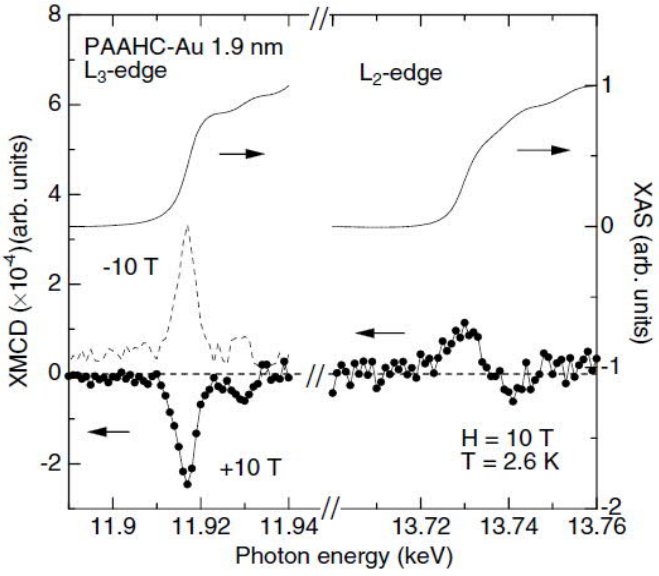

Figure 22: X-ray absorption spectroscopy (XAS) and XMCD spectra of Au[40]

Negishi et al. [5] investigated the X-ray magnetic circular dichroism of size-selected, thiolated gold clusters, utilizing both XANES and XMCD results. They plotted an XMCD diagram of the L_3 edge ($2p_{3/2}$-> $5d_{5/2}$, $6s_{1/2}$) and the L_2 edge ($2p_{1/2}$-> $5d_{3/2}$, $6s_{1/2}$) of $Au_{18}(SG)_{14}$ at a temperature of 2.7 K under a magnetic field at 10 Tesla. They obtained a negative and a positive peak at the L3 edge at 11.922 keV, and at the L2 edge at 13.733 keV, respectively. These peak positions show agreement with XMCD results obtained by Yamamoto/Hori, which indicate that the signal does actually emanate from Au and not from other magnetic impurities.

2.3.5 Preliminary explanations for the observed ferromagnetism in Au

There are a number of publications describing magnetism in Au-based nano-structures, as well as theoretical predictions and explanations for this phenomenon. Nonetheless, researchers have yet to reach agreement about the precise mechanisms associated with this unusual finding. While there are quite a few reasonable hypotheses to account for it, it is important to further investigate the likely origins of ferromagnetism in gold.

2.3.5.1 Induced Fermi hole imbalance at the surface due to symmetry breakings

Section 1.2.1.1 describes X-ray magnetic circular dichroism (XMCD) results for thiol-capped Au NPs performed by Hori and other groups. In addition to those studies,

Okazaki and Teraoka [42] also have conducted theoretical predictions for the existence of ferromagnetism induced by surface imbalance in thin films and NPs. Essentially, they believe that broken surface symmetry, which results from the large ratio of surface atoms in comparison to core atoms, is the actual mechanism causing surface ferromagnetic polarization. In nano- materials, one must consider the Fermi hole effect, where every electron spin is accompanied by a spin in the opposite direction—with both spins creating a sphere at the Fermi state. In Au NPs, however, due to the large ratio of surface atoms in Au NPs, an imbalance at the surface would be more apparent compared to bulk Au. The imbalance of 5d spins could result in the formation of d holes and subsequent polarization of spins at the surface of Au NPs. Specifically, there is believed to be an imbalance between the up and down spins on the surface of Au nanoparticles. This spin imbalance may account for the net polarization of ferromagnetic spin on the surface

2.3.5.2 Surface anisotropy and spin-orbit coupling induced by size effect

The term “surface anisotropy” was first discussed by Néel [54]. Basically, due to the crystal electrical field inside a bulk material, the orbital momentum of the electrons is dramatically quenched, and is superseded by the spin moment of electrons.[55] As a result, the magnetic contribution from orbital momentum is not usually taken into account when determining the total magnetic moments of a bulk material. Skomski [56] reported that due to the size effect—especially at the nanoscale—the nano-surface/core atom ratio will increase dramatically compared to the analogous figure for bulk materials. A large surface-to-atom ratio will suppress the quenching of the orbital moments, in which case the contribution from orbital momentum is considerable, and spin-orbit coupling will induce magnetic anisotropy on the lower coordinated surfaces of Au -nanoparticles[2, 38]. Such a mechanism can enhance the surface magnetic anisotropy energy in small particles, and induce ferromagnetism in noble metals that are nonmagnetic in bulk.

2.3.5.3 Localized magnetic moments induced by charge transfer in Au-S bonds

In addition to size effects, electronic structure can be another possible cause for the unconventional magnetic properties observed in nano-materials in noble metals. Magnetic

properties have been widely reported in nano-materials capped by organic surfactants such as alkyl thiols and amines. Crespo et al. [1], for example, described a charge transfer from metal atoms to organic shells containing thiol and nitrile (S and N) with the generation of holes in the d orbitals of Au NPs, giving rise to ferromagnetic moments at temperatures from 5 K to room temperature. In the sample of Au-S nanoparticles, there is a considerable amount of charge transfer from gold to thiol, which is believed to result in a larger number of d holes on the surface of Au atoms. Au-Au bond and Au-S bond nanoparticles have coordination numbers of 2.0 and 1.3, respectively, From XAS results described in Section 2.3.4, Figure 20, it appears that the large ratio of Au atoms remain on the surface. This means that Au-S bonding induced the 5d electrons of gold NPs to generate localized electrons on the surface, thereby becoming localized electrons.

2.4 Summary of Literature Review and Motivations for This Research

In this chapter, I have discussed the origins of magnetism for traditional materials, as well as specific types of magnetism and how they function at the atomic level. To reiterate, Au is diamagnetic in bulk; nonetheless, magnetism in Au nano-structures has been recently reported and increasingly discussed. Experimentally, Au NPs have been prepared by the reaction of chemical solutions, resulting in gold being coated by thiol-containing organic layers. Some researchers have indicated that Au-S bonds at the Au surface are the true source of magnetism, while others argue the magnetism is an intrinsic property of Au at the nano-scale level.

It should be noted that most of the sample preparation methods that other researchers have employed have been based on chemical precipitation of Au NPs followed by thiol-based cappings. In contrast, this study utilized a method based on physical evaporation, which can be used to clarify whether the presence or absence of Au-S bonds is needed to observe magnetism at the nano-scale.

CHAPTER 3:

MATERIALS AND METHODS

3.1 Sample Preparation Techniques: Pulsed Laser Deposition

This study relied on pulsed laser deposition (PLD) as an essential technique for sample preparation. Although there are many thin film deposition techniques, PLD is optimal for the growth of oxide thin films as well as metals, including high-Tc superconducting thin films such as YBCO (yttrium barium copper oxide). In terms of sequential processing, PLD consist of ablation of solid targets by focusing the laser on a solid surface—namely, the target material; this process typically takes place in a vacuum chamber. At the location where the laser is focused, some material will be ejected from the surface, which will form a plume containing high-energy plasma, atoms clusters, and molecules [61]. This deposition process can be controlled by adjusting a number of essential parameters, such as laser energy, chamber pressure, distance between target and sample substrate, and substrate temperature on the sample heater. Depending on these parameters, one can form nano-structures of varying dimensions. PLD has important advantages over other deposition methods, including preserving the stoichiometry between the target and deposited structure, high deposition speed, and comparatively easy operation. The experimental targets in this study included gold (Au), indium-tin oxide (ITO), aluminum oxide (Al_2O_3), and indium. Important to note is that there are six different available target positions on the rotary target holder in the chamber; thus, different targets can be ablated sequentially in the chamber to enable the growth of different substances on the same substrate. Different gases can be used for laser generation, including krypton (Kr), fluorine (F_2) and helium (He). These gases are used to generate a laser with a wavelength ranging from 193 nm to 308 nm. For this study we employed a krypton fluoride laser (KrF laser), also known as an excimer laser, with a wavelength of 248 nm. A schematic illustration of a PLD system is shown in Figure 23.

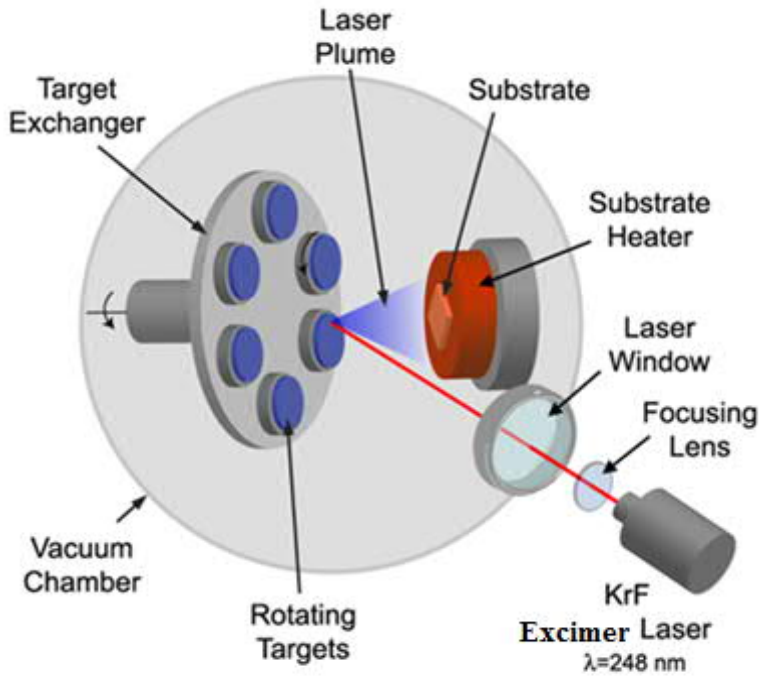

Figure23(a): A schematic representation of the PLD system in the Laboratory of Oxide Research and Education (LORE) lab

3.2 Deposition of Samples

In order to control both the diameter of the Au nanoparticles, as well as the thickness of the thin film serving as the deposited buffer layer, a set of thickness calibration samples had to be prepared. These calibration samples were prepared using the same conditions during which we later formulated the samples for magnetic and characteristic testing. Specifically, a pre-cut square sample was half covered by a mask prior to deposition. This technique essentially forms a “step” at the edge of the mask after the deposition, with half the sample coated and the other half remaining bare. The step height can be measured using a profilometer.

The growth rate of Au, ITO, Al_2O_3, and In_2O_3(indium oxide), as well as other materials that were subsequently used for future sample preparation, were measured via step PLD growth method. Results showed that the growth rate varied from 0.02 nm/pulse to 0.1nm/pulse depending on target selections. Knowing the growth rate of a given sample is important since the diameter of metallic nanoparticles and thin film thickness can be tailored

for different purposes. The details of sample preparation for each experiment are shown below:

3.2.1. A standard experiment set-up using PLD

We utilized pulsed laser deposition (PLD) of solid metal and oxide targets by an excimer laser under high vacuum (~ 10^{-6} to 10^{-7} Torr) to fabricate the samples. The samples were deposited on sapphire (100) substrates by a laser ablation of gold (Au), indium tin oxide target (ITO) and aluminum oxide (Al_2O_3) targets. Samples were prepared at either room temperature or at elevated temperatures up to 650 °C during the deposition. Prior to each deposition, the sapphire substrates ware cleaned in acetone and isopropanol. The PLD system contained a six-target carousel and a KrF excimer laser with a wavelength of λ =248 nm. The ITO, Al_2O_3 and Au targets were alternately ablated to form the desired samples. The experiments were been repeated a minimum of three times to confirm the results. .

3.2.2. Thin Film Growth Mode

The thin film growth process on a crystal surface depends largely on the interaction between adatoms of the deposited material and the surface of the substrate. The thin film growth process occurs in most of vapor phase deposition techniques such as pulsed laser deposition (PLD), physical vapor deposition (PVD) and molecular beam epitaxy (MBE). Thin films follow three growth modes: Volmer–Weber (VW) growth, Frank–van der Merwe (FM) growth and Stranski–Krastanov (SK) growth.

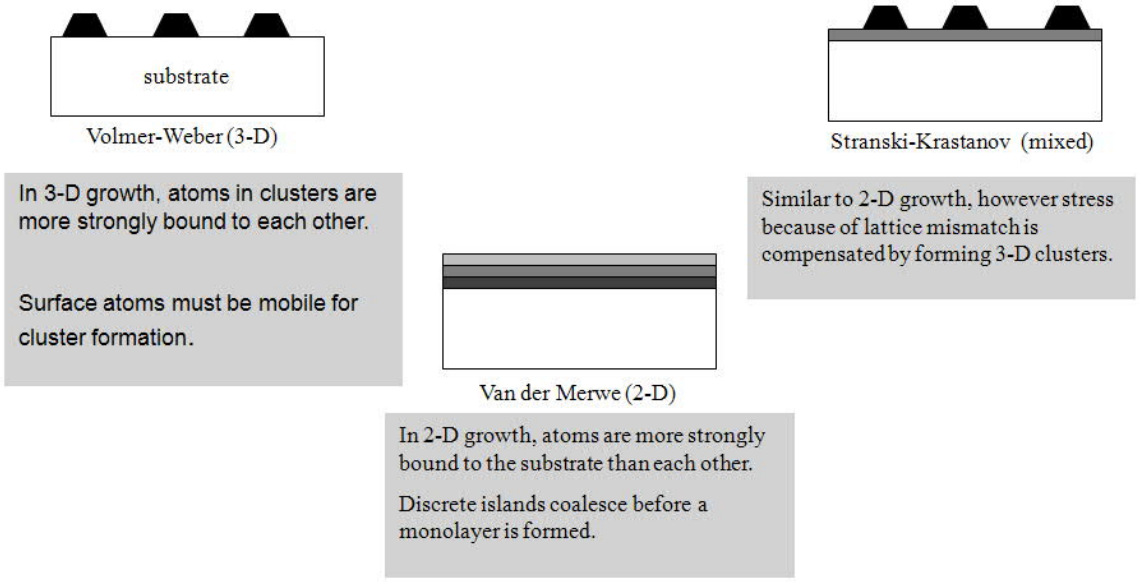

Figure23(b): A schematic representation of three thin film growth modes

In Volmer–Weber (VW) growth, the interactions among adatoms from the deposited material are stronger than those of the adatoms with the surface atoms of the substrate, resulting in the formation of three-dimensional structures that are also called islands. Island growth can be controlled in order to mimic the formation of nanoparticles. Conversely, in Frank–van der Merwe (FM) growth, the interactions among adatoms from the deposited material are weaker than those of the adatoms with the surface atom of substrate, leading to the formation of atomically smooth, fully formed layers. Stranski–Krastanov growth is a mixed growth mode characterized by both homogeneous 2D layers followed by 3D island growth. Transition from the two-dimensional to three-dimensional growth occurs at a critical layer thickness, which largely depends on the chemical and physical properties of both deposited and substrate materials, such as surface energies and lattice mismatch between the two materials.

3.3 Transmission Electron Microscopy

Transmission electron microscopy (TEM) is a technique whereby a beam of electrons is transmitted through a polished thin film. Due to interactions with the film as the beam passes through it, an atomic pattern is projected on a screen. The atomic resolution of the technique is associated with the deBroglie wavelength of electrons being around $\lambda = 0.004$

nm. An optimal TEM voltage is around 300 KV, which guarantee a resolution as high as an angstrom.

A typical TEM instrument (see Figure 24) is comprised of three component systems: the illumination components, the objective lens and adjustable stage, and the imaging tools. The illumination components contain an electron gun and a set of condenser lenses that collect the electrons from the gun focusing them on the specimen. The accelerator can increase the incident beam with energy ranging from 20 to 1000 eV; the condenser lens will tailor the diameter of the incident electron beam. However, the most important component system in a TEM is the objective lens and adjustable stage, which is where the beam-specimen interaction takes place. A well-tailored beam-specimen interaction is essential for obtaining good images and diffraction patterns, which are the two most frequently-used functions for this instrument. A TEM's imaging tools are comprised of a set of several lenses, including the objective lens system, which magnifies the projection images or diffraction patterns on a fluorescence display, a charge-coupled device (CCD) or TV camera. The images can be further recorded and stored on a computer.

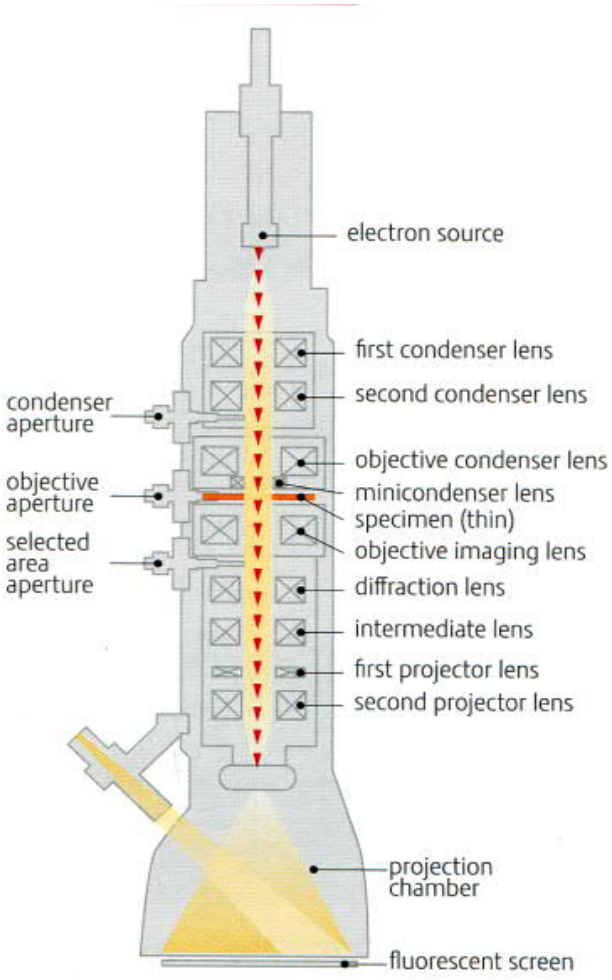

Figure 24: A schematic illustration of a typical TEM instrument

A requirement for any sample intended for TEM analysis is that it must be ultra-thin. Hand polishing and focused ion beam lithography (FIB) are two possible methods for reducing a bulk substrate into nano-meter thickness. For this study, the planar and cross-section samples were polished and viewed under a Titan TEM at the Nano-scale Characterization and Fabrication Laboratory (NCFL) at Virginia Tech. The instrument is shown in Figure 25.

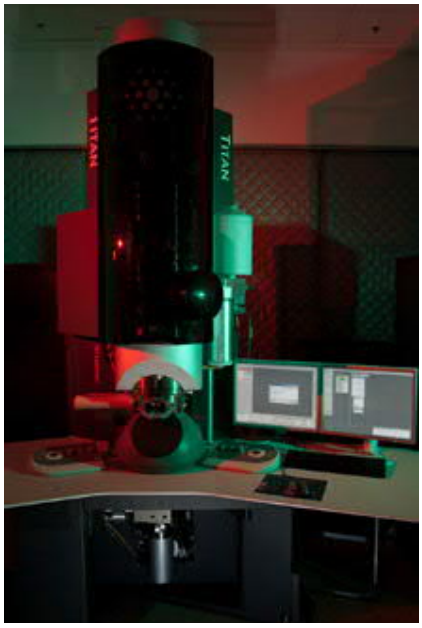

Figure25: Titan TEM at the NCFL at Virginia Tech

3.4 X-ray Photoelectric Spectroscopy

X-ray photoelectron spectroscopy is a very sensitive elemental characterization technique, which is based on the photoelectric effect. The photoelectric effect is a process by which an electron is generated by an incident X-ray with a given wavelength of sufficient energy to excite the electrons from the inner orbitals of the corresponding atoms. Since the energy of the incident monochromatic X-ray radiation would be known, one can measure the kinetic energy of excited electrons with a hemispherical energy analyzer in an XPS chamber and subtract that value from the incident energy; in so doing, the binding energy between the excited electron and the atoms with which it was bonded can be revealed. The binding energy of every electron orbital in different elements is unique, so the obtained binding energy can be used to determine the compositional details.

The process associated with of XPS signal capture is dependent on the photoemission process, which is determined by energy conservation rule:

$$E_b = h_v - E_k - W_f$$

Where h_v is the photon energy, E_b is the binding energy of electrons, E_k is the kinetic energy of the photoelectron, and W_f is the work function which is the minimum work to remove an electron from a solid to a point in the vacuum. With values for incident

X-ray wavelength and the kinetic energy of the photoelectron, the binding energy of electrons of a given element can be determined. The XPS principle is shown in Figure 26.

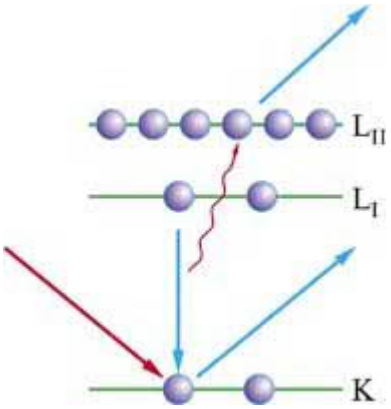

Figure 26: The schematic illustration of the principle of XPS

Important to note is that XPS is a very surface sensitive technique. In other words, it can only reveal the bonding information about a limited number of atomic layers from the surface. In contrast, an ion beam is normally used to sputter down the sample for ascertaining the bonding information inside a sample. The detection limits of XPS is 0.1–1.0 at% (0.1 at% = 1 part per thousand = 1000 ppm). The ultimate detection limit for most elements is approximately 100 ppm, which requires 8–16 hours.

3.5 Superconducting Quantum Interference Device SQUID

A superconducting quantum interference device (SQUID) is a highly sensitive magnetometer that can detect extremely subtle magnetic fields. Using a device known as a Josephson junction, a SQUID can detect a change of energy as much as 100 billion times weaker than the electromagnetic energy that moves a compass needle. In the presence of liquid helium, temperatures as low as 1.8 K can be reached. The field in the super-cold chamber can be as high as 7 T with the help of a superconducting loop. SQUID is ideal for applications that require detecting magnetism in nano-sized materials.

3.6 X-rayAbsorption Techniques: XAS and XMCD

As discussed in Chapter 1, X-ray absorption spectroscopy (XAS) is a technique that reveals the localized geometric or electronic structure of a material. XAS relies on intense and tunable X-ray beams from synchrotron radiation, such as electron accelerators, to

produce results. According to Beer's Law, which describes the absorption of electromagnetic radiation into solid matter[62]:

$$Ix = I0e - \mu I(x) = \quad I_0 e^{-\mu^{\circ} x}$$

Where the I_0 is the intensity of incident electromagnetic radiation, and $I(x)$ is the intensity of the electromagnetic signal within the tested material. This equation describes an energy loss along the direction of x going into the material. In the case of an X-ray the attenuation coefficient μ° is almost the same as the X-ray absorption coefficient μ. This assumption makes the use of XAS practical for many applications. In the application of XAS, we characterize the absorption edges by the X-ray absorption coefficient μ. Since different elements have their own unique absorption edges, XAS can be considered to be an element-selective technique. By probing the properties of absorption edge of excited electrons, it can identify the localized geometric or electronic structure of a given element.

X-ray magnetic circular dichroism (XMCD) provides element-specific magnetization curves that are comparable to magnetization in nano-sized structures and susceptibility data acquired by SQUID magnetometry. As such, it is a powerful tool for probing the magnetic properties of an electronic state of given symmetry. Consider 3d transition metals as an example. The valence electrons on the 3d bands are the true source of the magnetism of transition metals such as Fe and Co [63, 64]. Due to exchange interaction principles, this is characterized by the following equation:

$$M_s = -2 < s > \frac{\mu_B}{\hbar} \neq \quad N \uparrow - N \downarrow) \mu_B$$

The net amount of up and down spins equals the total amount of magnetic moments associated with the atoms in the 3d transition metals. As such, the spin-orbit interaction is almost seven magnitudes smaller than the exchange interaction, which can be ignored.

A good way to characterize those unfilled 3d electron bands are to excite those in the 2p bands into 3d bands and then study their X-ray absorption spectra, which are L_2 and L_3 edge of XAS spectra. In theory, the X-ray absorption of the L edges can take place in both p-to-d and p-to-s transitions; however, the intensity of the former is larger [65]. It is known that the sum of the white line intensities of both the L_2 and L_3 edges results in the total

number of d holes in a magnetic material, which permits one to investigate its unfilled electron orbitals and magnetic properties. [66]

Research confirms that photoelectrons can be generated/excited by left or right circularly polarized X-rays [67]. The photoelectrons are generated at the L_3 edge, and that angular momentum can be delivered to the spin. Right-polarized photons would deliver the opposite momentum to the electrons in comparison to left-polarized photons. We know that the L_3 and L_2 edges have opposite spin-orbit coupling, which is 1+s at L_3, and 1-s at L_2, so the direction of spin polarization on the L_3 and L_2 edges would be different too.

It has been studied that a case in which the spin moment is dominant in a given material, and the XMCD intensity is A at L_3 edge, and B at L_2 edge—which represent the intensities in response to right and left circular polarizations of spin contributions. According to the sum rule, the spin-related moment is shown as A-2B [68]. However, when the orbital moment is dominant, the net moment can be written as: A+B [53].

In the case of Au, it is worth noting that there is a contribution to the intensity from transitions to the continuum that must be subtracted from the raw XAS intensity data for the L_2 and L_3 edges. However, the intensity of the white line in Au NPs is very small, so in essence we can subtract XANES results for the white line information associated with the Au foil from the total signal.

CHAPTER 4:

FERROMAGNETISM IN Au-BASED ALLOYS

4.1 Introduction

As described in Chapter 1, Au nanoparticles (NPs) have been reported to be ferromagnetic when coated with organic layers such as dodecanethiol. Nonetheless, researchers disagree as to whether magnetism is intrinsic in gold-based nano-structures. In order to clarify this conundrum, this chapter will detail the preparation of Au-In-Sn alloys via pulsed laser deposition (PLD), which was achieved by ablating gold and indium oxide doped with tin oxide targets on sapphire substrates without any organic binders. The goal was to fabricate a composite sample of multiple layers of Au nanoparticles separated by ITO (indium tin oxide) thin film layers using Volmer-Weber-type growth for the Au nanoparticles. The morphology of the sample, however, was different from what we expected. The formation of the Au alloy is a result of the unexpected depletion of oxygen from indium oxide due to activity of Au —at the nano-scale, which will be discussed later. Although magnetic testing confirmed that the sample was magnetic, we believe that the magnetism emanated from the Au-ITO alloy instead of from other sources—e.g., from the substrate or from impurities, which we corroborated via XPS results. Furthermore, our calculations showed that the observed signal was too high for magnetic impurities with concentrations below the XPS detection limit. Therefore, in order to determine the origin of magnetism—namely from the Au or the In-Au alloy—uncapped Au NPs were prepared to compare them to the Au-ITO alloy sample we obtained in the first step. In the next section we will describe the preparation of Au NPs according to specific growth conditions, followed by a discussion of the magnetic testing results.

4.2 Methodology

4.2.1 Preparation of nano-structured Au-based alloys

To prepare the nano-structured Au-based alloys, we utilized conventional pulsed laser deposition (PLD) of solid metal and oxide targets by an excimer laser under high vacuum

(~10^{-6} torr). The apparatus consisted of a focusing lens for the incoming excimer laser (λ = 248 nm) and a vacuum chamber containing the targets and substrates. The number of laser pulses on the ITO target was fixed at 2000 pulses, whereas the number of pulses on the gold target was increased from 70 (sample S1) to 165 (sample S2) to 245 (sample S3), at a laser frequency of 10 Hz. Additional details about the sample preparation are discussed in Section 3.2. .

4.2.2 Morphologic, magnetic and elemental characterizations

Microstructural investigations were carried out at the Nano-scale Characterization and Fabrication Laboratory (NCFL) at the Institute for Critical Technology and Applied Science located at Virginia Tech. Specifically we utilized a FEI TITAN 80-300 transmission electron microscope, equipped with an E.A. Fischione model 3000 annular dark field detector (ADF), EDAX r-TEM energy dispersive X-ray spectrometer, which was operated at 200 kV in the scanning transmission electron microscopy (STEM) mode. Cross sectional TEM samples were made using the focused ion beam (FIB)-based micro-sampling technique, utilizing a FEI Helios 600. The elemental compositions of the samples were determined during TEM analysis by EDS. X-ray photoelectron spectroscopy (XPS) was used to verify the stoichiometry of the samples.

4.3 Results

4.3.1 Magnetic characterization of Au-ITO sample: Moment versus Field (MH) and Moment versus Temperature (MT)

The first step focused on elucidating the magnetic properties of nano-structured gold. To do so, we measured the magnetic properties of the samples at temperatures ranging from 5K to 300K. Results showed that ferromagnetic characteristics such as coercivity and remanence were observed up to 300 K. This finding was intriguing, since gold, ITO, and the various Au-In-Sn alloys are diamagnetic in bulk at room temperature. Figure 27(a) shows moment versus magnetic field hysteresis loops at 5K and 300K. An alumina (Al_2O_3) substrate was used, which is responsible for the diamagnetism observed at high field values; in contrast, ferromagnetism was detectable at low field values only. In order to eliminate the contribution of the substrate to the ferromagnetic hysteresis loops, the linear diamagnetic signal was

subtracted from our original result, which is depicted in Figure 27(b). The magnetometry results for the Au alloy samples confirmed that all samples were ferromagnetic.

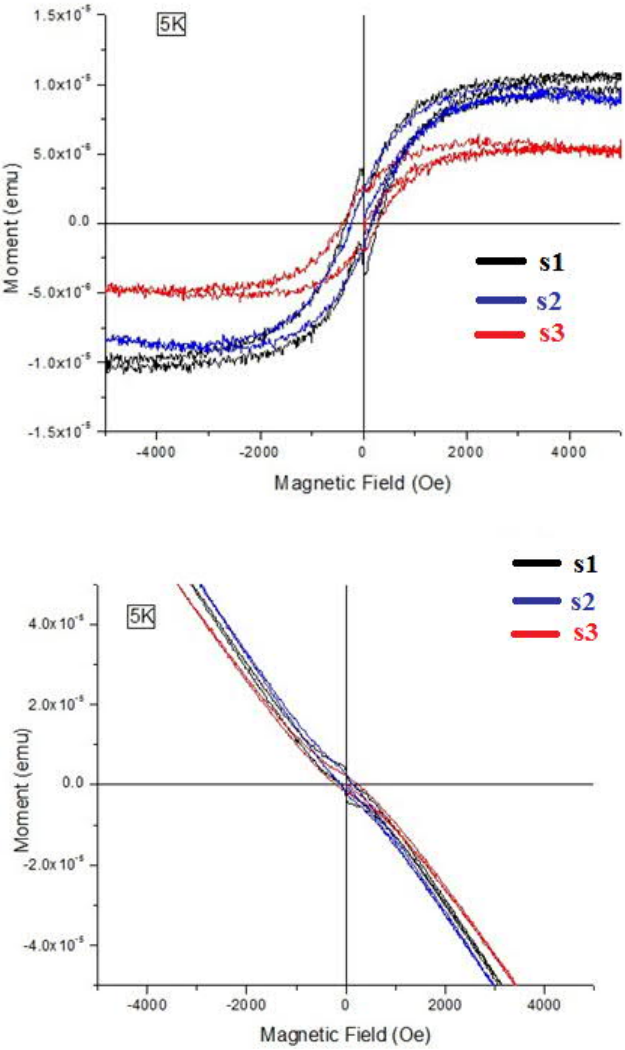

Figure 27 (a): Moment versus Magnetic Field at 5K for three samples: before (bottom) and after (top) subtracting diamagnetic signal from sapphire substrate

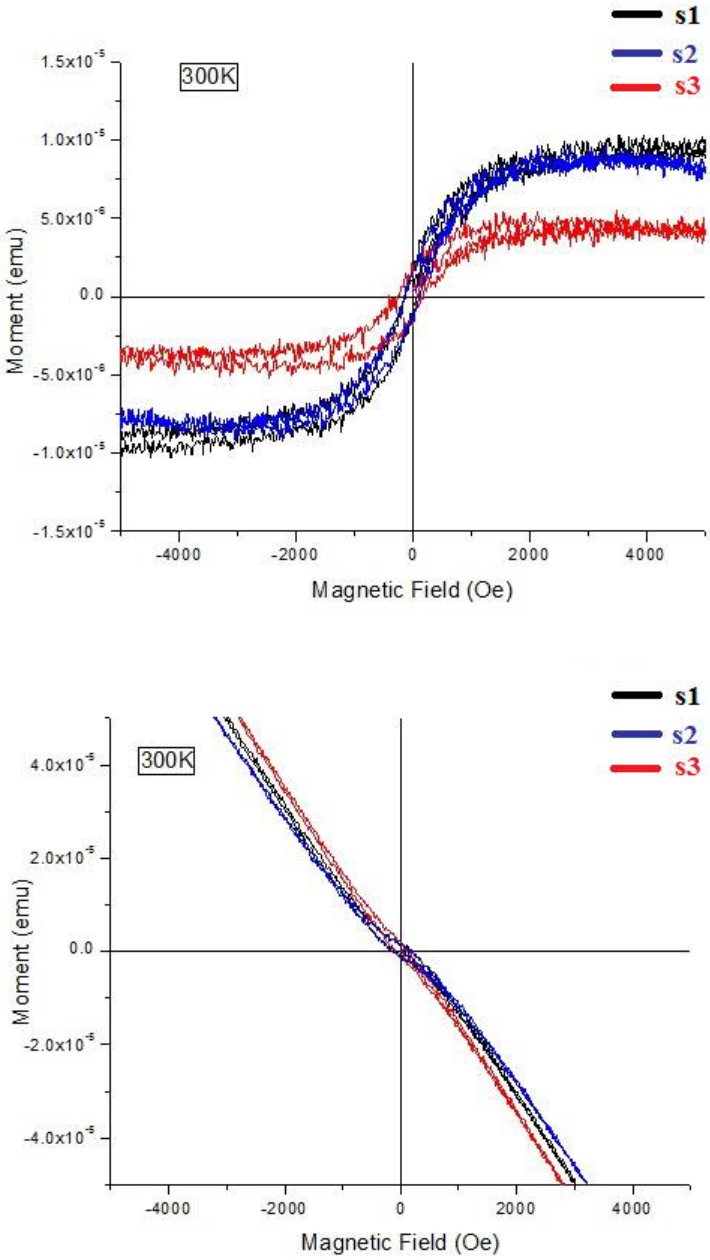

Figure 27 (b): Moment versus Magnetic Field at 300K for three samples: before (bottom) and after (top) subtracting diamagnetic signal from sapphire substrate

We also plotted saturation magnetization versus temperature for the three Au-In samples (Figure 28). Data were gathered from the MH loops for the different samples.

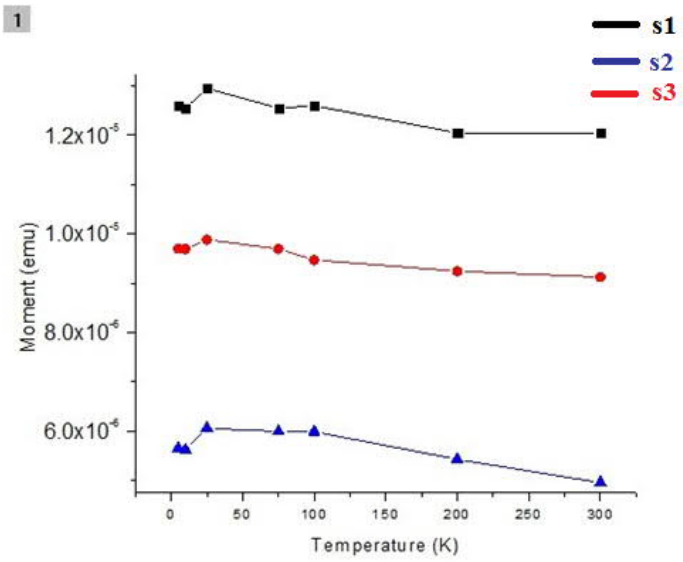

Figure 28: Saturation magnetization versus temperature for three samples

Three unique features of the Au system became quite apparent. First, the magnetic moment of the Au nanoparticles dramatically decreases as the nano-particle diameter is increased. This relationship is seemingly counter-intuitive. In traditional magnetic materials, the magnetic moment increases with nano-particle diameter because it is dependent on the number of atoms contributing to the magnetic signal. The second unique feature of this Au system is the absence of a significant correlation between magnetic moment and measurement temperature (see Figures 28). Typically, the magnetic saturation ($M_s \sim T^{-3/2}$) level yields an appreciable increase in magnetic moment as the measurement temperature approaches 0K. The third outstanding characteristic associated with the magnetic properties of Au nanoparticles can be observed in the MH loops in Figure 27. Specifically, resulting coercivity data shows little dependence on either particle size or measurement temperature. These three findings suggest that the physical origin of the ferromagnetism in the Au-ITO sample may be quite different from traditional ferromagnetic materials.

The correlation between size and magnetic saturation (Ms) derived here shows why observed ferromagnetism is limited to small dimensions only. In other words, as size increases, polarization decreases because of the decrease in the fraction of surface atoms.

4.3.2 Morphology of the Au-rich phase in the alloy: TEM characterization

The ferromagnetic properties of the Au-ITO samples were examined by magnetic

measurement. As mentioned in Section 3.2.1, the initial plan was to fabricate a composite sample of multiple layers of Au nanoparticles separated by ITO thin film layers using Volmer-Weber type growth for the Au particles. However, Figure 29 clearly shows that no Au nanoparticles were present and the sample consisted of a multiphase thin film. Figure 29 illustrates a cross-sectional image of a sample Au-ITO composite showing the platinum (Pt) layer, composite thin film, and the sapphire substrate. The platinum layer on the sample's top was deposited to protect the sample during Focused ion beam (FIB) processing. Generally, two main phases were observable in the sample. The microstructure of the film appears inhomogeneous based on the contrast differences in the STEM-HAADF image. Together with subsequent EDS results (discussed later), we determined that the brighter regions were Au-rich and the darker regions were In-rich. The mean size of each phase was estimated to be 100 nm. Considering that the gold and ITO targets were ablated separately, the formation of an Au-ITO composite indicates that either the gold diffused into the indium-tin oxide, or vice versa.

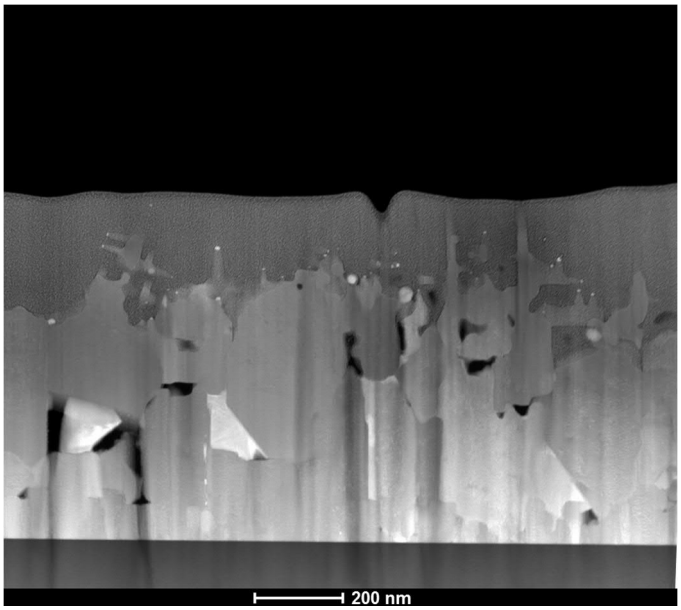

Figure 29：Cross-sectional image of the Au-ITO composite showing the platinum layer (top), composite thin film, and the sapphire substrate.

4.3.3 Elemental and binding characterizations by Energy Dispersive X-ray Spectrometry (EDS) and X-ray Photoelectron Spectroscopy (XPS)

As shown in Figure 30, chemical analyses were performed across a grain of bright, Au-rich grain, and dark, In-rich grain. Table 1 summarizes the concentration of Au, In and Sn in those phases. The oxygen concentration is also provided as a reference. Although the presence of oxygen cannot be quantitatively assessed by regular EDS analysis in TEM, we found a strong positive correlation between oxygen and In; in contrast, the Au signal intensity decreased when the oxygen signal increased. Therefore, we concluded that two distinct phases were present; a metal alloy phase consisting of Au-In and Sn, and second phase that was predominantly ITO. The gold concentration jumped from 1.507 wt% to 59.142 wt%, as the beam was moved from the dark phase to the bright phase. The concentrations of In, Sn and oxygen decreased dramatically. This trend was confirmed by analysis of the adjacent dark region, which is labeled in this figure as point #4.

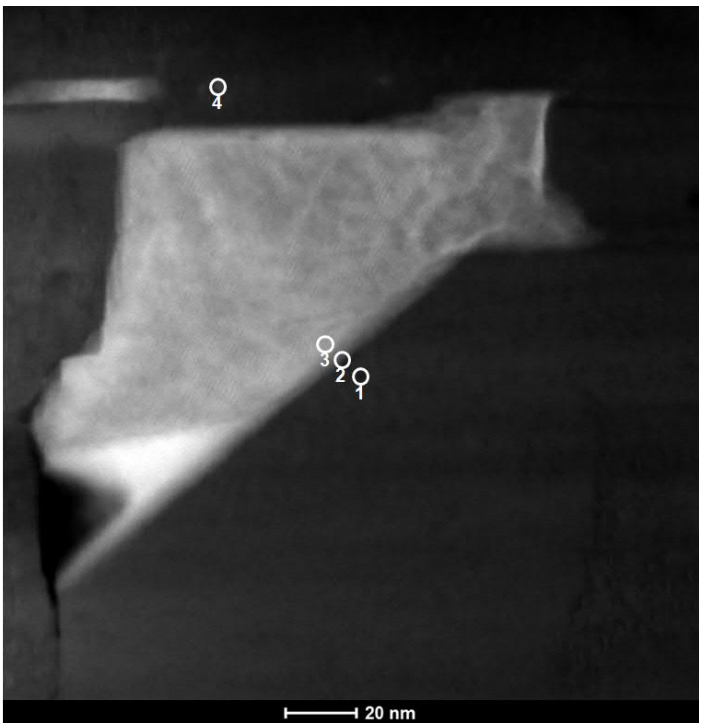

Figure 30: Cross-sectional image of the Au-ITO composite. Chemical analysis performed across a grain boundary of brightly imaged Au-rich grain and darkly imaged In-rich grain

Table 1: concentration of Au, In and Sn across a grain boundary of brightly imaged Au-rich grain and darkly imaged In-rich grain

Analysis position	Au wt%	In wt%	Sn wt%	O wt%
1	1.507	86.000	0	12.493
2	7.179	67.191	14.376	11.254
3	59.142	29.486	10.092	1.280
4	5.213	71.373	11.557	11.857

The reduction of indium oxide to metallic indium resulted in localized Au-rich phases. Considering that the melting temperatures of metallic indium and indium oxide are 156 ^{o}C and 1910^{o}C, respectively, we believe that the nano-structured Au was responsible for this phenomenon.

The reactivity of Au-based nano-structures has been well studied. Au and other noble metal nanoparticles (e.g., platinum) are used as catalysts because of their enhanced reactivity at the nano-scale. In this specific case, it is possible that the presence of Au particles at high temperature induced the migration of oxygen out of ITO film, which resulted in localized molten regions of In and Sn that readily reacted with Au, which is illustrated in Figure 31. This type of Au-induced de-oxygenation was also reported for the Au-STO-LSMO system. As a result, the high reactivity of gold nano-structured materials represents the underlying driving force for localized reduction, resulting in the formation of Au-rich phases in the Au-In alloys. Our observations are consistent with the phase diagram for the Au-In system. It should be noted that the Au-In system was primarily considered due to the fact that Au–In and Au–Sn alloys are very similar, and the concentration of Sn as a dopant in ITO is very low. The Au phase prior to reaction with ITO was in particulate form or discontinuous. The lack of contact between the Au particles and the ITO in some regions of the samples resulted in distinct boundaries between Au-rich and Au-free regions, thus accounting for the resultant compositional inhomogeneity.

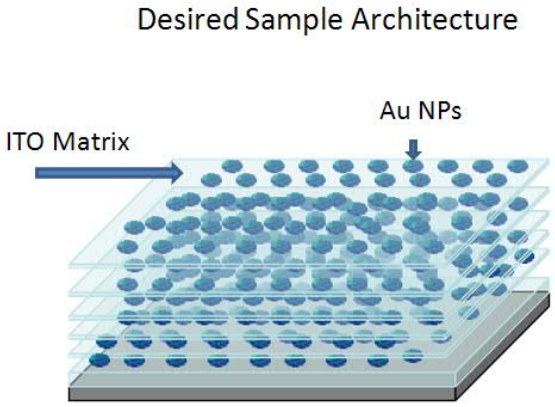

Figure 31a: A schematic illustration of expected sample structure prior to experimentation.

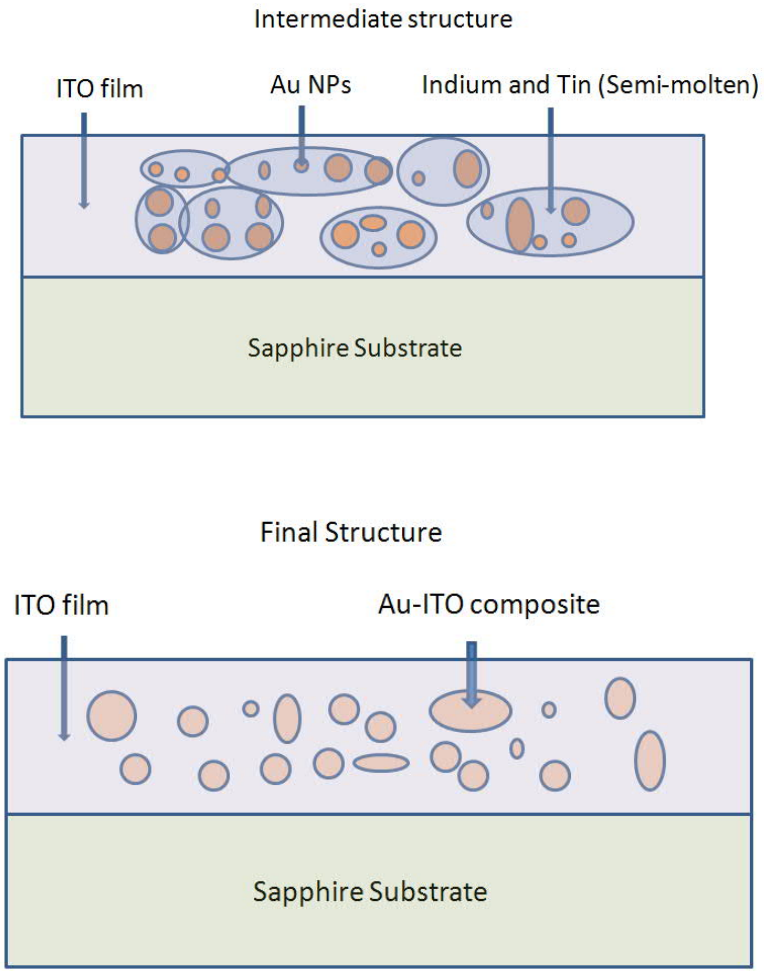

Figure 31b: A schematic illustration of the formation of an Au-ITO composite.

X-ray photoelectron spectroscopy (XPS) was used to determine the chemistry of Au in the Au-In-Sn alloys. As shown in Figure 32, the Au binding energy in sample 1 is ~ 84.5 eV and

88.5 eV, whereas the In peaks are at 452 eV and 444 eV, which are also seen in other samples. These peaks show good agreement with reference data for Au-In bonding. Given these XPS and EDS results, evidence suggests that Au and In are indeed alloyed.

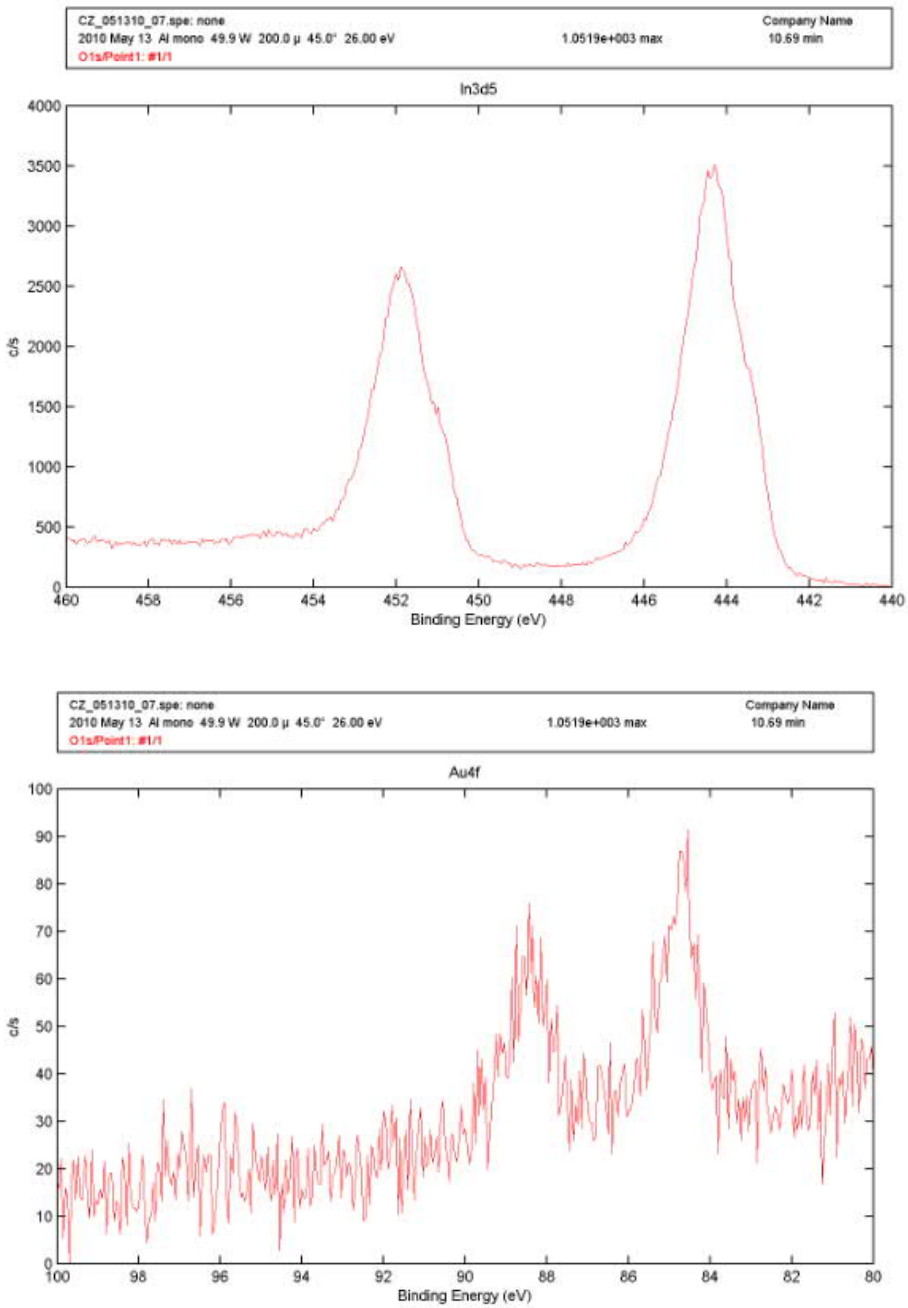

Figure 32: XPS results for Indium and Au in Au-ITO composite

In order to confirm that the observed magnetism emanated from the Au component,

we prepared an analogous sample having the exact same composition of ITO on the sapphire substrate—minus the presence of Au. Figure 33 is the MH loop for ITO on sapphire substrate, which has same concentration of ITO as the one with gold showing magnetic under PPMS. The diamagnetic pattern in Figure 33 clearly indicates the sample is diamagnetic without gold. The present of gold is a key factor to observe ferromagnetism, even in a state of alloy with other elements.

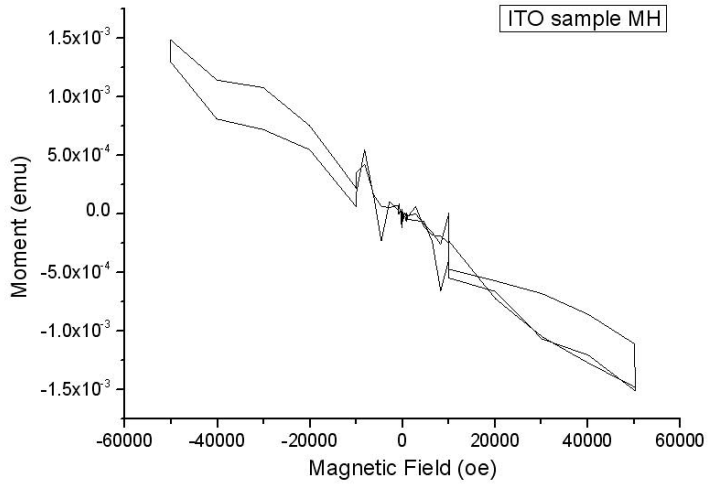

Figure 33: MH for ITO on sapphire substrate

This study then attempted to identify the specific mechanism associated with the observed magnetism in Au-based alloy systems. As discussed earlier in the literature review with respect to Au/Pt alloys [2], scholars believe that d charges migrate from Au sites to Pt sites during the formation of alloys, which causes the generation of d holes in Au atoms, and a gain in d electron in Pt atoms. So the magnetism we observed for our assay can possibly be driven by the same mechanism—namely, that because of electron migrations there are d holes generated in the Au sites of Au-In alloys, which can possibly polarize electron spins in Au atoms. However, an Au-based alloy is a distinctly different system in comparison to Au NPs. Thus, the mechanism for magnetism in an alloy system should be different from the magnetic mechanism associated with nanoparticles.

4.3.4 Examining the existence of FM impurities

It may be argued that the observed magnetism is due to the presence of ferromagnetic impurities, such as Co and Fe. Three reasons make this highly improbable in our sample.

First, both EDS and XPS depth profile results suggested that no ferromagnetic impurities were present within detectable limits. Additionally, the samples were handled in such a way as to avoid coming in contact with any magnetic impurities. Thus, the sample was free from any instrument-related contaminants. Second, magnetism typically strongly depends on the temperature in most ferromagnetic materials. For example, the magnetization of Fe or Ni is proportional to $T^{-3/2}$, which means the magnetization will decrease dramatically with an increase in temperature. However, we observed very little change in the magnetization of our sample when the temperature was increased from 5 K to 300 K, which indicates that the contribution of magnetic impurities to the magnetic signal was highly unlikely. Third, a recent report [24] indicates that the presence of FM impurities actually weakens the observed ferromagnetic activity in Au-based nano-structures. Specifically, the researchers concluded that Fe impurities reduce the high local anisotropy field, which contributes to ferromagnetic behavior in gold nanoparticles. As a result, the ferromagnetism in Au NPs is not likely to be associated with the existence of magnetic impurities.

The following results were obtained via XPS with respect to the degree to which the magnetic moment can contribute to the total signal, as shown in the following calculation:
The detection limit of the XPS ranged from 0.1 wt% to 0.02 wt%, and the limit for EDS is around 1 wt%. XPS is one of the best surface sensitive techniques to examine a thin layer of Au NPs on the substrate. The size of Au NPs is less than 5 nm shown under TEM, which is comparable with XPS work depth about several atomic layers. The sapphire substrates from manufacturer were examined on EDS and XPS for ferromagnetic impurities prior to the sample preparation. Since XPS has much higher resolution than EDS on surface, we selected the upper detection limit of XPS for determining the presence of magnetic impurities. Fe was selected as a candidate whose saturation moment is 93.1 emu/g. Considering that the depth of XPS detection into a given material is about 5 nm, and the area of our sample was 1 cm^2, the detection volume is:

$$V = 5 \text{ nm} \times 1\ cm^2 = 5 \times 10^{-13} m^3$$

Since the amount of Fe impurity was very small, we can use the Au mass as the total mass of the detection volume. With the density of Au being 19.3 g/cm^3, the total mass of detection volume is:

$$M = 96.5 \times 10^{-10} g$$

Using the upper limit of XPS, which is 0.1% wt, the total mass of Fe impurity in our study was 96.5 x 10^{-10} g, which makes a contribution of 8.98x10^{-7} emu to the total signal. The moment of our sample was 10^{-5} emu, which is two magnitudes higher than the impurity signal of Fe (if it exists). In conclusion, it is not likely that any Fe impurities contributed to the strong signal we obtained.

We also performed an XPS in-depth profile on the Au-ITO sample, the results of which are shown in Table 1. Note that the highest concentration of FM impurities emanated from the Co sample, which at 0.07 wt.% is much less than the value we assumed above. Again, the observed magnetism was very unlikely to have been caused by sample impurities.

Table 2: XPS depth profile

Time, min	Fe2p at%	Co2p at%	Ni2p at%
0	0	0.06	0
0.8	0	0.02	0.03
1.6	0	0.04	0.05
2.4	0	0.07	0.04
3.2	0	0.03	0.02
4	0	0	0.02
4.8	0	0	0.02
5.6	0	0	0.02
6.4	0	0	0.01
7.2	0	0	0
8	0	0.02	0
8.8	0	0.07	0.01
9.6	0	0.06	0.02
10.4	0	0.02	0.01

4.4 Chapter Summary and Discussion of Remaining Problems

As mentioned above, our original plan was to make a composite sample of multiple layers of Au nanoparticles separated by ITO thin film layers using Volmer-Weber type growth for the Au particles. However, Figure 29 clearly shows that instead of Au nanoparticles, a Au-ITO alloy is present in the sample. The associated process is illustrated in Figure 31. We

assumed that the actual driving force behind the phenomenon of the absence of oxygen was the high reactivity of Au NPs, which can locally disassociate oxygen from the ITO oxides, thereby creating a phase separation with oxygen inhomogeneity. The Au-In and Au-Sn phase diagrams suggest liquid phases in the Au-In-Sn alloy at an experimental temperature at 650 ^{o}C, which also implies possible solubility between Au and In or Sn after degeneration from the corresponding oxide composites in ITO. A physical property measurement system (PPMS) equipped with a vibrating sample magnetometer (VSM) was used to measure the field dependence of the magnetic moment. The samples showed clear signs of ferromagnetism up to room temperature. An Au-free sample, but with the same amount of ITO on a sapphire substrate, was determined to be diamagnetic. Ferromagnetic impurities were ruled out as the source of the magnetic signal via careful compositional analysis. Thus, the Au element in the Au-ITO sample is believed to be the source of magnetism. The d holes in Au generated by electron migration are believed to account for the observed magnetism. It should be noted, however, that even though magnetism was observed in the Au-ITO sample, it does not necessarily mean that metallic Au NPs are the source of that magnetism since an Au-In alloy is formed. Further evidence is needed to support such a conclusion. The ferromagnetic properties of Au NPs will be discussed in Chapter 5.

CHAPTER 5:

FERROMAGNETIC Au NANO--PARTICLES (NPS) IN DIFFERENT DIAMAGNETIC THIN FILM MATRICES

5.1 Introduction

The previous chapter confirmed that nano-structured Au-In/Sn alloys exhibited ferromagnetism at both low and room temperature. However, it remains to be determined if the Au NPs or the Au-ITO alloy—or both—were magnetic. In this chapter, we review preparation of Au NPs at room temperature, instead of at high temperature, which prevents the formation of Au-based alloys. Using pulsed laser deposition (PLD), Au-ITO samples were grown at room temperature (sample S1); sample S2 was prepared at 400 ^{o}C, which is above the melting temperature of indium wherein Au-based alloy formation is expected. Additionally, bare Au NPs embedded in an Al_2O_3 matrix (sample S3) were also prepared. Samples S1 and S3 contained bare Au NPs, and S2 was utilized to test if magnetism remained when Au was present in the alloy phase. Results indicated that all three samples were ferromagnetic at both low (5 K) and high temperatures (400 K). Moreover, we found that Au can deplete oxygen in an indium oxide structure and form nano-structured Au-In alloys above the melting temperature of indium, which rarely takes place when the temperature is comparative low. Again, based on our observations of ferromagnetism in both samples, it seems plausible that ferromagnetism originated from the gold in Au-based nano-structures.

5.2 Morphologic, Magnetic and Elemental Characterizations

Microstructural investigations were carried out using the FEI TITAN 80-300 equipped with an E. A. Fischione Model 3000 annular dark field detector operated at 200 kV in STEM mode. Cross sectional TEM samples were made using focused ion beam (FIB), utilizing the FEI Helios 600. The elemental composition of the samples was determined during TEM investigations employing energy dispersive X-ray spectroscopy (EDS). X-ray photoelectron spectroscopy (XPS) was used to verify the stoichiometry of the samples. The magnetic

properties of the Au-ITO and Au-Al_2O_3 systems were measured using a physical property measurement system (PPMS) equipped with a vibrating sample magnetometer, and superconducting quantum interference device (SQUID) at low and room temperature.

Figure 34 provides a diagram of moment-versus-magnetic field (MH) for samples S1 and S3. The data were gathered from the MH loops for the different samples tested at 5 K and 400 K, respectively. Both samples exhibited typical ferromagnetic properties, i.e., exhibiting complete hysteresis loops in a MH diagram, as shown in Figure 2. Several unique features of the Au system are quite apparent, however. First, in comparing the room temperature (RT) Au-ITO sample to the RT Au- Al_2O_3 sample, we found an increase in both magnetic moment and coercivity—the latter measuring the resistance of a ferromagnetic material to becoming demagnetized. Second, we found a temperature effect on the hysteresis loop of both samples at different testing temperatures. Specifically, magnetic moment and coercivity decreased a little when the temperature was increased from 5 K to 400 K. Moreover, the influence of temperature appeared to be greater for the RT Au-ITO in comparison to the Au NPs, but nonetheless remained within the the same magnitude, which is 10^{-6} emu. The MH loop for the 400°C Au-ITO sample was similar to the loop described in the prior chapter, which also exhibited typical ferromagnetic hysteresis.

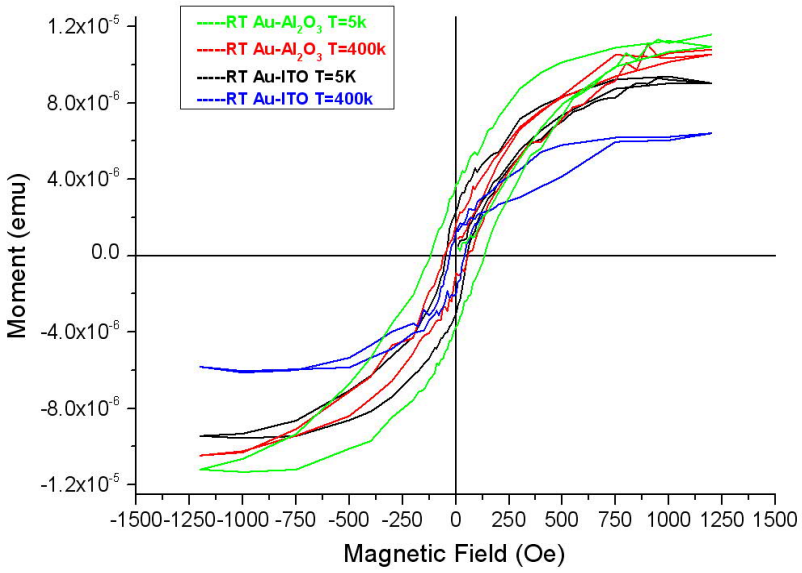

Figure 34: MH loop of Au-ITO and Al_2O_3 sample prepared at room temperature, tested at 5 K

and 400 K respectively

Figure 35 provides a moment-versus-temperature plot for the RT Au-ITO sample with a testing field of 50 Oe. The dashed lines represent original data with noise, and the solid lines indicate the averages for both zero field cooling (ZFC) and field cooling (FC). The ZFC and FC lines bifurcate at a blocking temperature of 220 K, above which temperature traditional ferromagnetic materials shows superparamagnetic or ferromagnetic properties. However, we observed a strong ferromagnetic signal in the RT Au-ITO sample at 400 K, which is higher in comparison to the observed blocking temperature from the M-T diagram. This unique property indicates that the underlying mechanism for ferromagnetism in Au-based nano-structures is very different from traditional 3d transition metals.

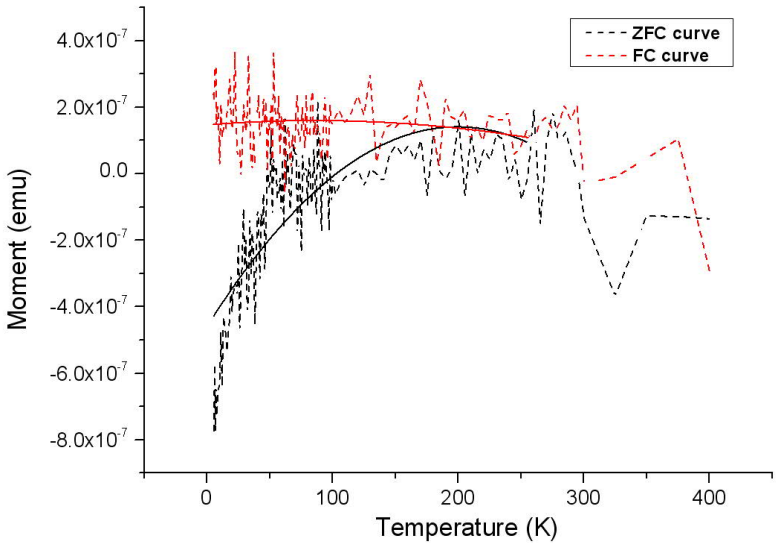

Figure 35: MT curve for Au-ITO sample made at room temperature. Dash lines are original data with noise, and the solid lines are average lines for both ZFC and FC.

Comparing our results to others mentioned in Chapter 1, we have seen that different measurement give very different values. As discussed in the paper, we and other researchers believe that the magnetism of Au NPs originates from the Au surface atoms, although it is still debatable if Au-S bonds or symmetry broke at surface that induced 5d holes on the surface Au atoms. So the change of surface area, or the size and shape of the Au NPs can

dramatically change the number or the state of surface atoms, which can give very different values under different conditions. Information about the morphology and bonding status of Au in the sample is required to examine if the Au is actually separated metallic NPs or bonded with ambient atoms. TEM and XPS analysis was performed. The details are given in the next sections.

5.3.2 Morphology of Au NPs in ITO and Al_2O_3: TEM characterization

Figure 36 provides a high resolution TEM image of sample S1 of the Au NPs surrounded by an ITO matrix. Figure 39 illustrates the analogous TEM of S3 wherein the Au was embedded in an Al_2O_3 matrix. The dark particles with clear lattice fringes are the Au NPs, which was verified by EDS. The boundary of the Au NPs with surrounding ITO or Al_2O_3 film is distinct and clear, which is completely different from the morphology described in Chapter 4, in which Au is alloyed with ITO under STEM ADF image (see Figure 29). Additionally, as evidenced by TEM, we did not observe any incorporation between the films and the Au NPs in either sample S1 or S3, which indicates that samples prepared at room temperature are metallic separated instead of bonding with ambient at a higher temperature. The bonding of Au is discussed in the next section, which will be further examined in light of XPS results.

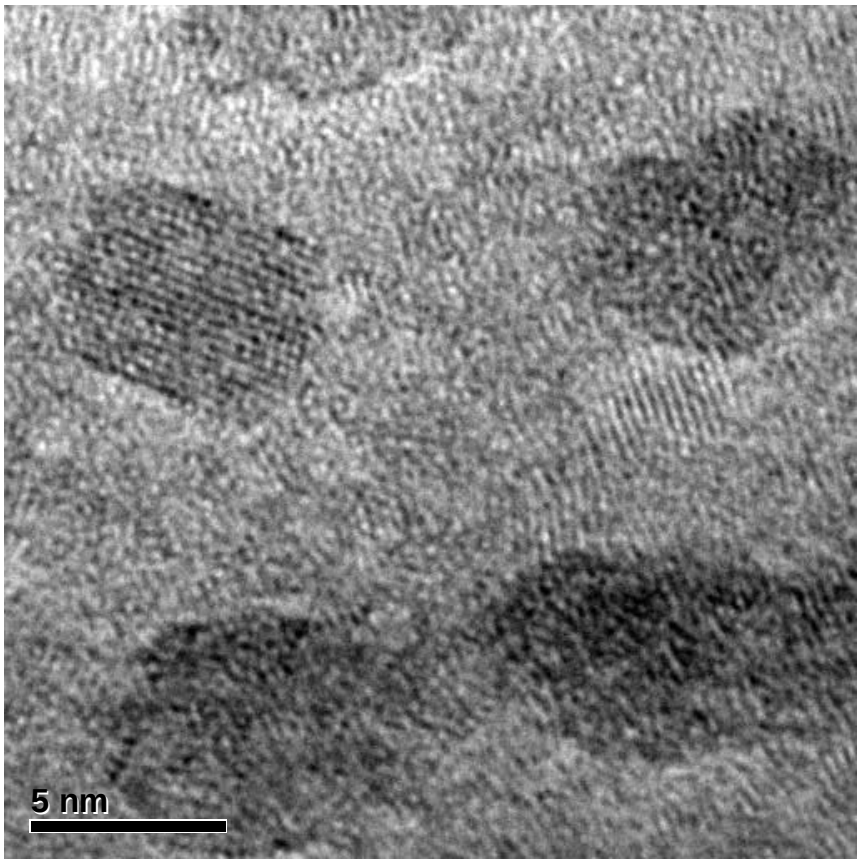

Figure 36: TEM picture of Au NPs in an ITO matrix

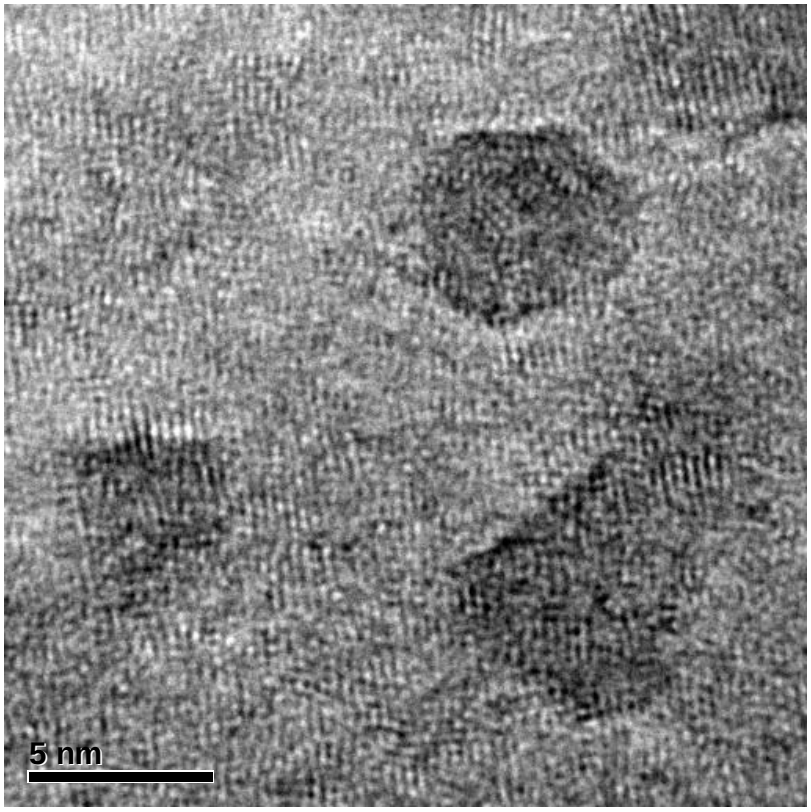

Figure 37: TEM picture of Au NPs in an Al2O3 matrix

5.3.3 Elemental characterizations by X-ray photoelectron spectroscopy (XPS)

As discussed in Chapter 4, we determined that Au was actually alloyed with ITO at a substrate temperature of 650 ^{o}C instead of metallic Au NPs. Furthermore, samples with chemically separated Au NPs are required for the purpose of magnetic testing. TEM pictures provided in Section 5.3.2 illustrate that Au NPs were present in both samples S1 and S3 prepared at room temperature. However, more conclusive information about the bonding conditions of Au can be provided by XPS spectra. In order to determine if the Au was actually chemically separated in the metallic phase or truly bonded with ITO in the sample S1 prepared at room temperature—as well as to understand the formation temperature of the Au-ITO alloy—we conducted an XPS scan on S1 (the Au-ITO prepared at room temperature) and S2 (the Au-ITO prepared at 400 ^{o}C). It should be noted that the melting temperature of indium is 156 ^{o}C.

Figure 38 shows the XPS results for S2 prepared at 400 ^{o}C (top), S1 prepared at RT (middle), and the Au-Al_2O_3 sample prepared at RT (bottom). There are several obvious Au-In peaks in the 400 ^{o}C Au-ITO sample, as shown in the top figure. In comparison, XPS results indicate relatively little contribution from the Au-In bonds in the RT Au-ITO sample. The most distinct difference between the top two figures, however, is the presence of several obvious Au-In peaks in S2 in the top diagram, whereas only very little contributions from Au-In bonds in the XPS results in S1. The XPS results confirm that a nano-structured Au-In alloy can be obtained when the temperature is higher than the melting temperature of indium in an Au-ITO composite, but hard to form when the temperature is significantly lower. In addition, the Au oxide peak is very small in the Au-Al_2O_3 sample prepared at RT, which indicates that Au is in its metallic phase as well. As a result, XPS and TEM results suggest that Au is mostly chemically separated in metallic NPs (e.g., S1, the Au-ITO sample prepared at room temperature).

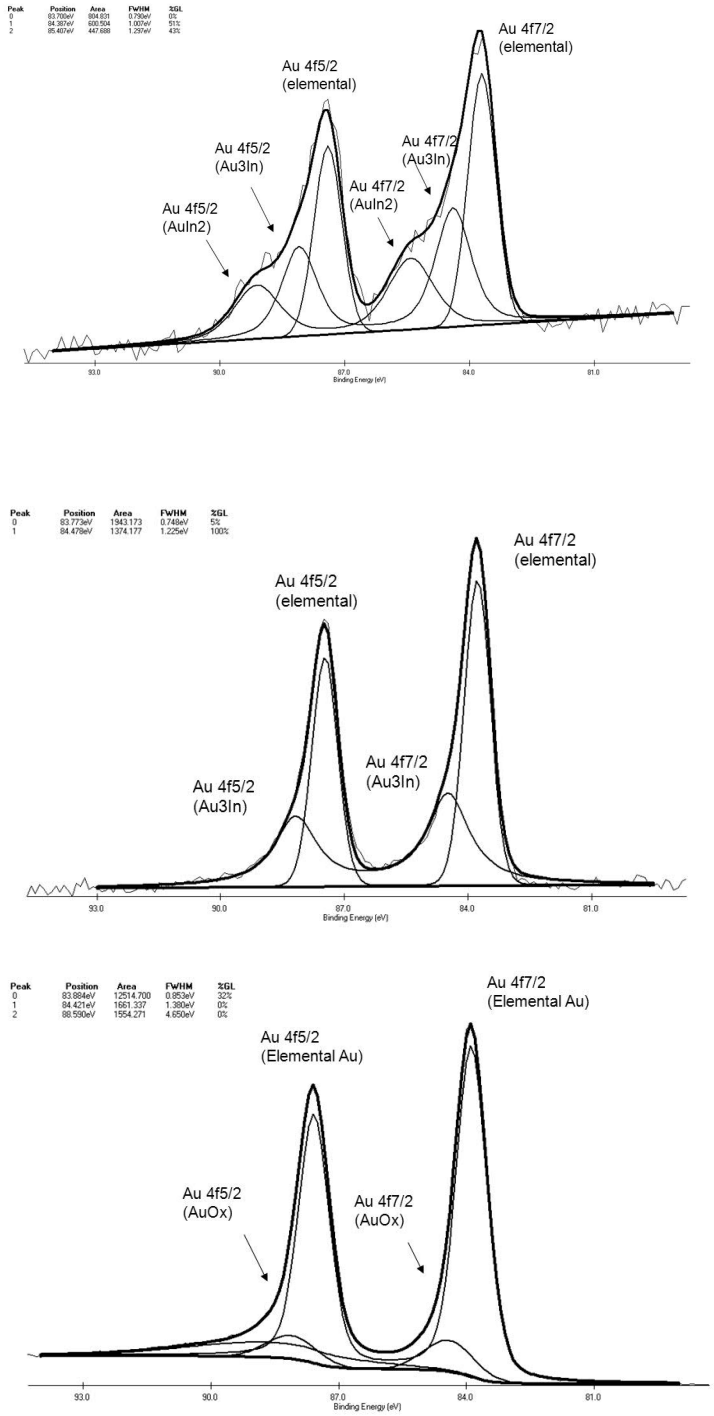

Figure 38: XPS of the Au-ITO sample prepared at 400 ^{o}C (top), Au-ITO sample prepared at RT (middle), and Au-Al_2O_3 sample prepared at RT (bottom).

Furthermore, given that the melting temperatures of metallic indium and indium oxide are 156 ^{o}C and 1,910 ^{o}C, respectively, we believe that the nano-structured Au was responsible for the phenomenon of alloy incorporation in sample S2. These XPS results agree with prior

results in chapter 4 that Au nanoparticles pump oxygen away from the ITO layers in Au-ITO composites above melting temperature of indium. Moreover, considering that Au-In has lower free energy than In-O at formation temperature, Au-rich indium alloys form in localized regions during synthesis of the samples. In summary, the high reactivity of gold nano-structured materials represents the underlying driving force for localized reduction, which results in the formation of Au-rich phases in Au-In alloys.

5.3.4 Summary

We prepared two Au-ITO samples—the first at room temperature (S1), and the second at 400 ^{o}C (S2) And Au-Al_2O_3 sample (S3) was also prepared at RT. All samples showed a clear ferromagnetic signal; additionally, as evidenced by TEM, samples S1 and S3 have a similar morphology. The Au element in sample S2 formed an alloy with indium, which was confirmed by XPS; this was not the case with either S1 or S3. TEM and XPS results suggest that Au is chemically separated in the case of metallic NPs in both S1 and S3. Figure 29 (Chapter 4) and XPS results for sample S2 indicate that Au can deplete oxygen in indium oxide structures and form nano-structured Au-In alloys when the synthesis temperature is higher than the melting temperature of indium; in contrast, this phenomenon rarely takes place when the temperature is comparatively low.

The magnetic results from this study clearly indicate that the three samples (S1, S2 and S3) are magnetic. The diamagnetic diagram for the ITO film on a sapphire substrate without gold is shown in the previous chapter (see Figure 33). The Au NPs in all three samples, therefore, can be credited for the observed magnetism.

CHAPTER 6:

X-RAY ANALYSES: XAS AND XMCD

6.1 Introduction

As discussed in Chapter 3, by utilizing left- and right-polarized X-rays, XMCD (X-ray magnetic circular dichroism) is a technique that can transfer the angular momentum of magnetic elements to excited photoelectrons. For this phase of the research, we used XMCD on an Au-ITO sample. Recall that XAS results indicated that the sample had a significant amount of d holes, which was indicated by the shift of the L3 edges of Au NPs compared to Au foil. However, no peak was observed in the XMCD spectrum.

6.2 Experimental Procedures

Due to specimen requirements for both for XAS and XMCD testing, samples for X-ray absorption must exceed 3 microns in thickness. To fabricate the samples, we utilized pulsed laser deposition (PLD) of solid metal and an oxide target by an excimer laser in high vacuum (~ 10^{-6} torr). The apparatus consists of a focusing lens for the incoming excimer laser (λ = 248 nm) and a vacuum chamber, in which targets and substrates were located. During PLD, the samples were deposited on sapphire c-plane substrates by a laser ablation of gold (Au) and indium oxide doped with tin oxide (ITO) targets. Prior to each deposition, the sapphire substrates were cleaned in acetone and isopropanol. The chamber was pumped to a base vacuum of ~ 10^{-7} torr. ITO and Au targets were alternately ablated to form the multi-layer samples at room temperature. The Au and ITO targets were ablated 165 and 1000 times, respectively, at a frequency of 10 Hz.

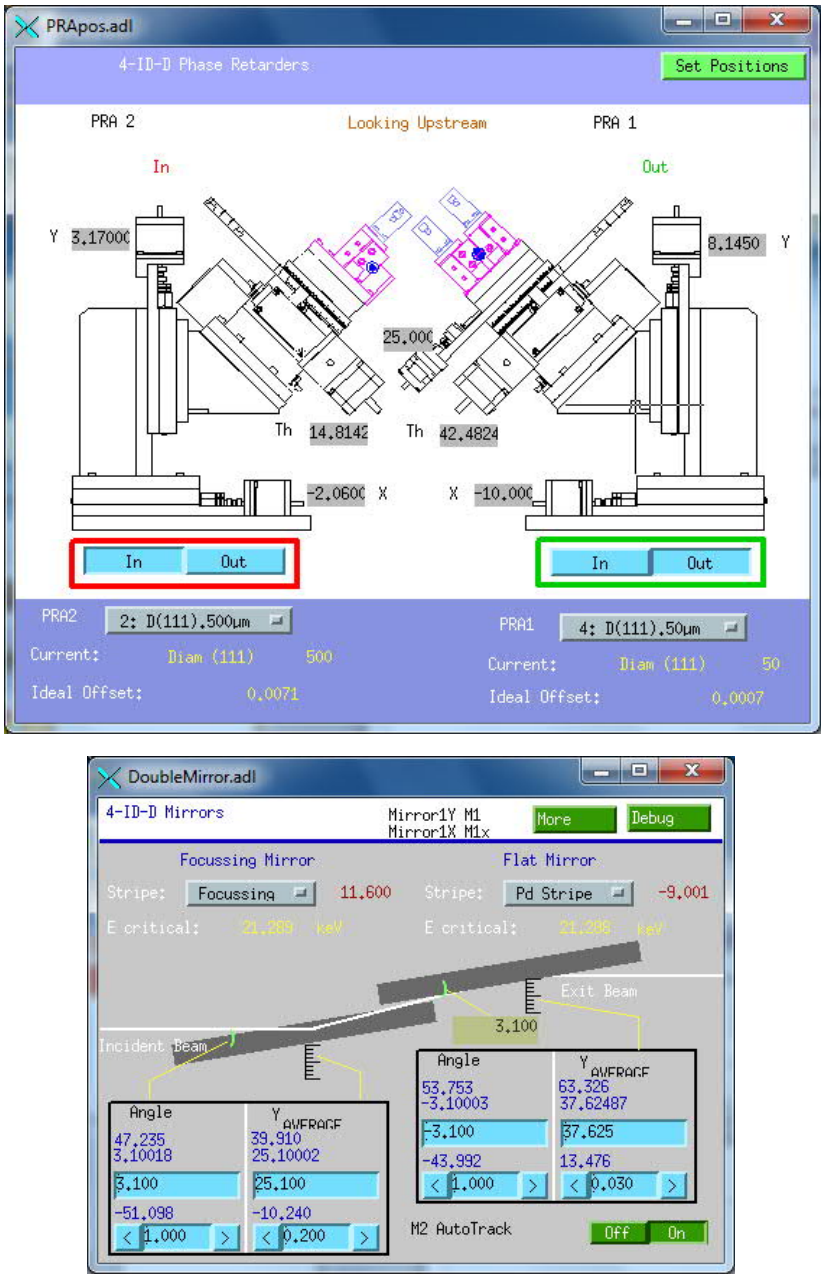

Figure 39: Experimental data when performing X-ray absorption

XAS and XMCD testing was conducted at Argonne National Laboratory's Advanced Photon Source (APS) on a Beamline 4-ID-D, which is an instrument that facilitates polarization-dependent spectroscopic and scattering studies of magnetic materials (see Figure 39, 40). The Beamline is equipped with crystal phase retarding optics, allowing the user to manipulate the polarization of the incoming X-ray beam on the sample. All data acquisition was performed on Sun workstations (UNIX/Solaris) using the SPEC software program. Beamline control is achieved though EPICS-based applications running VME-based

electronics. MEDM is used as a graphical interface to display and control various EPICS-based devices.

This particular cycle was repeated 400 times to form a ~3 micron thick film, considering the growth rates of Au and ITO, which were 0.12 and 0.15 nm per pulse, respectively. After deposition, samples were polished from the back to eliminate most of substrates for subsequent transmission X-ray absorption testing, and were then cleaned. Ultimately, as noted earlier, sample thickness could be no more than 30 microns.

6.3 XAS Spectra

As illustrated in Figure 40, we compared the peak shifts for both the Au NP sample and the Au foil after normalizing both curves. Note that the Au NP displayed a similar pattern of the Au foil, indicating that both have a similar electronic environment; however, the NP sample showed a significantly higher peak at the L3 edge compared to the foil. The intensity of the whiteline of the Au NP was also stronger in comparison to the Au foil, which means there is an increased concentration of d holes in the Au NP [4, 69]. We believe that the observed magnetism in gold NPs results from unfilled 5*d* holes, which is associated with the large surface-to-core ratio of nanoparticles. Nevertheless, due to surface effect there is a significant concentration of 5*d* holes generated on the surface of Au NPs, which creates surface Au atoms with unfilled 5*d* bands. The X-ray absorption spectrum is strong evidence of the existence of 5d holes in Au nanoparticles.

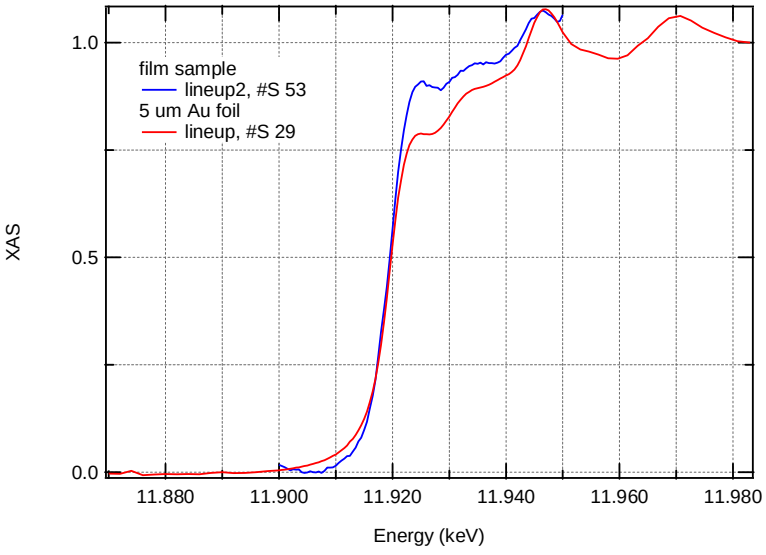

Figure 40: XAS spectrum obtained for both the Au NP sample and Au foil.

6.4 XMCD Spectra

XMCD results were also obtained at Argonne National Laboratory. As discussed earlier, XMCD is an element-specific technique. If a given element is suspected to be the origin of magnetism, a sign change in XAS signal would be observed when the direction of the magnetic field reverses. By subtracting the left-polarized XAS spectrum from right-polarized one, a peak at the L_3 edge should be seen in the XMCD spectrum. Figures 41 a and 41 b are XAS results with magnetic field in two opposite directions, and Figure 42 shows the XMCD results for our Au NPs by substracting one XAS result from the other in figure 41. The L_3 peak was located at 11.918 eV for the Au NP. However, we did not observe a sign reverse at the L_3 edge of the Au—nor a peak in our XMCD results.

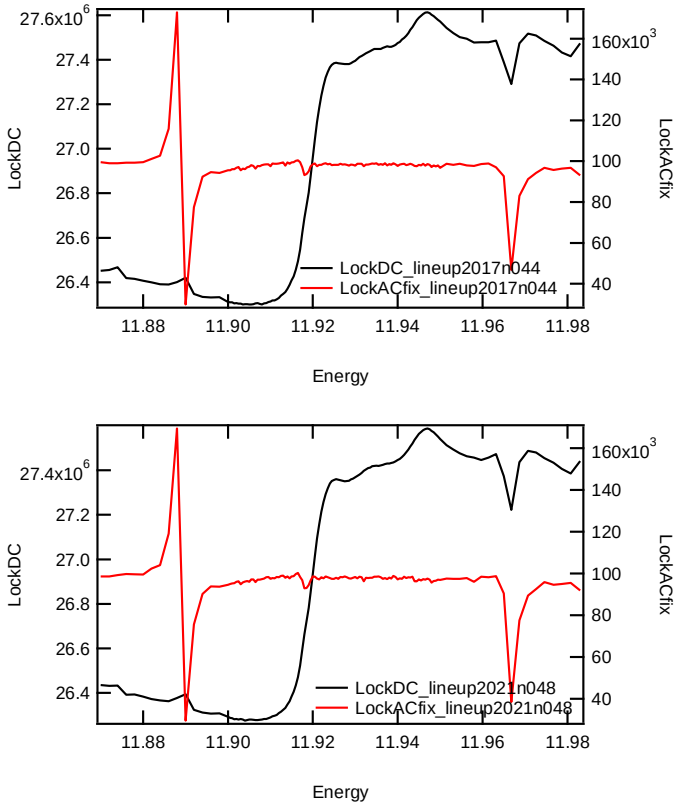

Figure 41. XAS spectrum of scans with magnetic field in two opposite directions respectively performed by left-polarized X-ray.

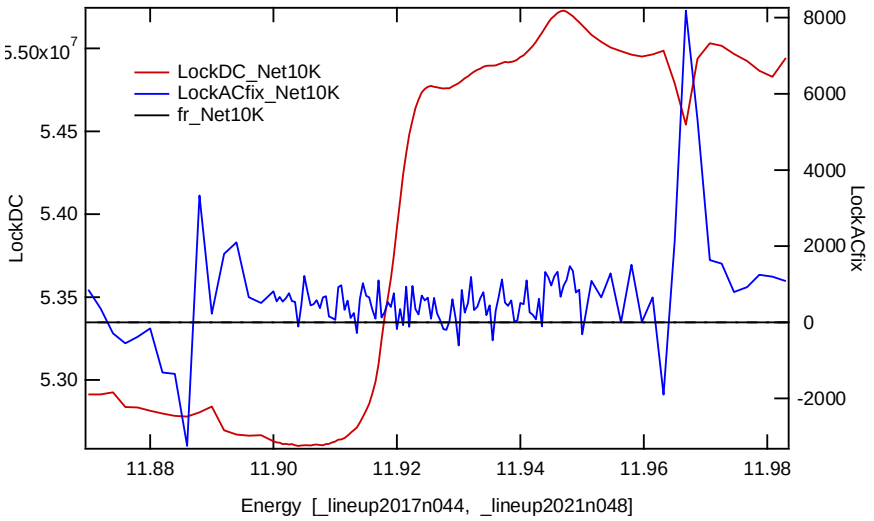

Figure 42: XMCD result: Difference of XAS spectra

One possible explanation for this unexpected result could be the insufficient amount of Au in the sample. Given that the mean size of our Au NPs was around 5 nm in diameter, and the planar dimension of the sample was 1 cm^2, the effective mass of Au compared to the entire sample was approximately 0.5 % wt. However, in order to detect the presence of a magnetic signal, at least 3 % wt. of Au is required. As a result, despite the fact that we detected a different shape of whiteline at the L3 edge in the Au NP sample compared to the Au foil, we were unable to identify a peak at L3 edge in the Au sample in the XMCD spectrum.

6.5 Possible Explanations for Observed Magnetism in Gold

This study investigated the formation, morphology and magnetic properties of Au-ITO alloy samples, as well as Au NPs in ITO and an Al_2O_3 matrix. Our samples were free from any organic binding, which could have the unwanted effect of inducing spin polarization on the Au surface atoms. Therefore, linking induced surface magnetism to the charge transfer along Au-S bonds would not be applicable in this case, since our samples did not contain any organic components. Considering that our XAS results indicated the presence of a significant number of 5d holes in the Au NPs sample, we believe that the most possible mechanism of magnetism in Au is associated with the existence of 5d holes. However, it is still under investigation if so-called size effect that induces surface anisotropy and spin-orbit

coupling is an explanation for the magnetism. It is believed that surface imbalance due to broken symmetry could induce Fermi holes in Au NPs, thereby leading to the observed magnetism. Due to the large ratio of surface atoms in Au NPs, an imbalance at the surface would be more apparent compared to bulk Au. The large surface area of Au NPs could result in the formation of d holes and subsequent polarization of spins at the surface of Au NPs. This hypothesis was supported by our experimental results.

CHAPTER 7:

CONCLUSION AND FUTURE WORK

To reiterate, an Au-based alloy was prepared as illustrated in the STEM picture in Figure 29. We believed that the true driving force behind this phenomenon is the high reactivity of Au NPs, which can regionally disassociate oxygen from the ITO oxides, thus creating phase separation with oxygen inhomogeneity. The Au-In phase diagrams suggest liquid phases exist for Au-In alloy at the experimental temperature of 650 ^{o}C, which also implies the possible solubility between Au and In after degeneration from corresponding oxide composites in ITO. The samples showed clear signs of ferromagnetism up to room temperature. A Au-free sample—but with the same amount of ITO on a sapphire substrate—was proven to be diamagnetic. Ferromagnetic impurities were ruled out as the source of the magnetic signal by careful compositional analysis. Therefore, the Au element in the Au-ITO sample is believed to be the source of magnetism. Nonetheless, the existence of magnetism in an Au-ITO sample does not necessarily support the idea that metallic Au NPs are the source for this magnetism in the sample since an Au-In alloy was formed. Au-based alloys are a distinctly different system in comparison to Au NPs. Thus, the mechanism associated with the observed magnetism in those alloy systems would likely be different in comparison to Au nanoparticles.-

In order to obtain bare Au NPs without any organic bonding or alloy formation, we prepared Au-ITO samples at both room temperature (S1) and at 400 ^{o}C (S2); Au-Al_2O_3 samples (S3) were also prepared at room temperature. All samples showed a clear ferromagnetic signal with similar morphology under TEM prepared at room temperature. The Au element in S2 bonded with indium, which was evidenced by XPS results. In constrast, this incorporation was not found for either the S1 or S3 samples. In fact, TEM and XPS results suggest that Au is chemically-separated as metallic NPs (as shown in S1 and S3). TEM images in Chapter 5 (Figure 36 and Figure 37) and XPS results for S2 both indicate that Au can deplete oxygen in an ITO structure and form nano-structured Au-In alloys—providing that the experimental temperature is above the melting temperature of indium

The experimental data generated by this study clearly indicate that samples S1, S2,

and S3 were magnetic. The diamagnetic characteristics for the ITO film on a sapphire substrate without gold were shown in Chapter 4, which confirmed that the presence of Au NPs in all three samples was responsible for the observed magnetism. Our samples were free from any organic capping layers, which could have induced spin polarization on Au surface atoms. Therefore, linking induced surface magnetism to the charge transfer along Au-S bonds would not be applicable in this case, since our samples did not contain any organic components.

Based on our XAS results, which indicated the presence of a significant number of 5d holes in our Au NPs samples, we believe that true mechanism for magnetism in Au is associated with those 5d holes. In other words, the resulting surface effect induces surface anisotropy and un-suppressed spin-orbit coupling. Another possibility is that the surface imbalance due to broken symmetry could have induced Fermi holes in Au NPs, thereby leading to the magnetism we observed. Due to large ratio of surface atoms in Au NPs, a surface imbalance is more apparent in those gold nanoparticles in comparison to bulk Au. The imbalance of 5d spins could result in d holes and the polarized surface of Au NPs due to un-suppressed spin-orbit coupling at symmetry broke surface. Nevertheless, in a confined system reduced coordination favors narrower electron bands and yields a larger density of states at the Fermi level. Thus, the presence of Au-S bonds may not be the reason for the observed magnetism in Au NPs. This hypothesis shows agreement with obtained experimental results.

XAS and XMCD were performed on Au NPs samples. The spectrum shift in the L3 edge of the NPs compared to the spectrum obtained for the L3 edge of the Au foil clearly indicates the presence of a considerable number of d holes generated in the Au NPs. It should be noted, however, that we did not detect a peak via XMCD results, which corresponds to the net sum of spectra from left- and right-polarized X-rays. A possible explanation for the missing peak in the XMCD spectrum is due to an insufficient amount of Au in the testing sample.

A future study should reproduce the samples utilized herein for additional element-specific measurements via XMCD testing. In so doing, it would be possible to determine the critical size of Au NPs that would generate ferromagnetism. Additionally, a

subsequent study should systematically study magnetism in other diamagnetic metals at the nano-scale—such as nano-Ag or Cu—and compare them with gold NPs in order to elucidate the various mechanisms associated with magnetism in diamagnetic nano-structures.

Reference

1. Crespo, P., et al., Permanent magnetism, magnetic anisotropy, and hysteresis of thiol-capped gold nanoparticles. Physical Review Letters, 2004. 93(8).
2. Dutta, P., et al., Magnetism in dodecanethiol-capped gold nanoparticles: Role of size and capping agent. Applied Physics Letters, 2007. 90(21).
3. Zhang, P. and T.K. Sham, X-ray studies of the structure and electronic behavior of alkanethiolate-capped gold nanoparticles: The interplay of size and surface effects. Physical Review Letters, 2003. 90(24).
4. Liu, H.J., et al., Electronic structure of ensembles of gold nanoparticles: Size and proximity effects. Physical Review B, 2005. 72(15).
5. Negishi, Y., et al., X-ray magnetic circular dichroism of size-selected, thiolated gold clusters. Journal of the American Chemical Society, 2006. 128(37): p. 12034-12035.
6. Novakovic, R., E. Ricci, and F. Gnecco, Surface and transport properties of Au-In liquid alloys. Surface Science, 2006. 600(23): p. 5051-5061.
7. Yamamoto, Y. and H. Hori, Direct observation of the ferromagnetic spin polarization in gold nanoparticles: A review. Reviews on Advanced Materials Science, 2006. 12(1): p. 23-32.
8. Yamamoto, Y., et al., Direct observation of ferromagnetic spin polarization in gold nanoparticles (vol 93, pg 116801, 2004). Physical Review Letters, 2006. 96(13).
9. de la Venta, J., et al., Magnetism in polymers with embedded gold nanoparticles. Advanced Materials, 2007. 19(6): p. 875-+.
10. J.T. Abiade, S.H.O., S. Pennycook, D. Christen, J. Thompson, and D. Kumar, Synthesis and Characterization of magnetic gold nanoparticles. MRS Spring Meeting, 2007. 9-13.
11. Luo, W., S.J. Pennycook, and S.T. Pantelides, s-electron ferromagnetism on gold and silver nano-clusters. Nano- Letters, 2007. 7(10): p. 3134-3137.
12. Magyar, R.J., et al., Density-functional study of magnetism in bare Au nano-clusters: Evidence of permanent size-dependent spin polarization without geometry relaxation. Physical Review B, 2007. 75(14).
13. Michael, F., et al., Size dependence of ferromagnetism in gold nanoparticles: Mean field results. Physical Review B, 2007. 76(22).
14. Phala, N.S. and E. van Steen, Intrinsic reactivity of gold nanoparticles: Classical, semi-empirical and DFT studies. Gold Bulletin, 2007. 40(2): p. 150-153.
15. Abiade, J.T., et al., The effect of matrix and substrate on the coercivity and blocking temperature of self-assembled Ni nanoparticles. Journal of Applied Physics, 2008. 104(7).
16. Tiwari, A., et al., Ferromagnetism in Cu-doped ZnO films: Role of charge carriers. Applied Physics Letters, 2008. 92(6).
17. Brivio, S., et al., Effects of Au nanoparticles on the magnetic and transport properties of La(0.67)Sr(0.33)MnO(3) ultrathin layers. Physical Review B, 2010. 81(9).
18. Deng, S.Z., et al., Thiol-Capped ZnO Nano-wire/Nano-tube Arrays with Tunable Magnetic Properties at Room Temperature. Acs Nano-, 2010. 4(1): p. 495-505.
19. Costelle, L., et al., Spin-glass magnetism of surface rich Au cluster film. Applied Physics Letters, 2011. 99(2).
20. Hernando, A., et al., Revisiting magnetism of capped Au and ZnO nanoparticles: Surface band structure

and atomic orbital with giant magnetic moment. Physica Status Solidi B-Basic Solid State Physics, 2011. 248(10): p. 2352-2360.
21. Ayuela, A., et al., sp magnetism in clusters of gold thiolates. New Journal of Physics, 2012. 14.
22. Burgos, M., et al., Gold, silver and palladium complexes with the 2,2'-dipyridylamine ligand. European Journal of Inorganic Chemistry, 2003(11): p. 2170-2174.
23. Crespo, P., et al.,Permanent magnetism in thiol capped nanoparticles, gold and ZnO. Acta Physica Polonica A, 2008. 113(1): p. 515-520.
24. Crespo, P., et al.,Fe impurities weaken the ferromagnetic behavior in Au nanoparticles. Physical Review Letters, 2006. 97(17).
25. Crespo, P., et al.,Influence of the Capping Molecule on the Magnetic Behavior of Thiol-Capped Gold Nanoparticles. Ieee Transactions on Magnetics, 2008. 44(11): p. 2768-2771.
26. de la Venta, J., et al.,Size Dependent Ferromagnetic-Like Behavior in Thiol Capped Gold Nanoparticles. Science of Advanced Materials, 2009. 1(3): p. 241-248.
27. De La Venta, J., et al.,Magnetic properties of organic coated gold surfaces. Modern Physics Letters B, 2007. 21(6): p. 303-319.
28. Guerrero, E., et al., Magnetometry and electron paramagnetic resonance studies of phosphine- and thiol-capped gold nanoparticles. Journal of Applied Physics, 2010. 107(6).
29. Guerrero, E., et al., Electronic structure, magnetic properties, and microstructural analysis of thiol-functionalized Au nanoparticles: role of chemical and structural parameters in the ferromagnetic behaviour. Journal of Nano-particle Research, 2008. 10: p. 179-192.
30. Guerrero, E., et al., Surface plasmon resonance and magnetism of thiol-capped gold nanoparticles. Nano-technology, 2008. 19(17).
31. Guerrero, E., et al., Evolution of the microstructure, chemical composition and magnetic behaviour during the synthesis of alkanethiol-capped gold nanoparticles. Acta Materialia, 2007. 55(5): p. 1723-1730.
32. Hernando, A., P. Crespo, and M.A. Garcia, Metallic magnetic nanoparticles. Thescientificworldjournal, 2005. 5: p. 972-1001.
33. Hernando, A., P. Crespo, and M.A. Garcia, Origin of orbital ferromagnetism and giant magnetic anisotropy at the nano-scale. Physical Review Letters, 2006. 96(5).
34. Munoz-Marquez, M.A., et al., Permanent magnetism in phosphine- and chlorine-capped gold: from clusters to nanoparticles. Journal of Nano-particle Research, 2010. 12(4): p. 1307-1318.
35. Hori, H., et al., Magnetic properties of nano--particles of Au, Pd and Pd/Ni alloys. Journal of Magnetism and Magnetic Materials, 2001. 226: p. 1910-1911.
36. Hori, H., et al., Diameter dependence of ferromagnetic spin moment in Au nano-crystals. Physical Review B, 2004. 69(17).
37. Suzuki, M., et al., Measurement of a Pauli and Orbital Paramagnetic State in Bulk Gold Using X-ray Magnetic Circular Dichroism Spectroscopy. Physical Review Letters, 2012. 108(4).
38. Takahashi, N., et al., Output properties of C-60 field-effect transistors with different source/drain electrodes. Applied Physics Letters, 2007. 90(8).
39. Taki, M., et al., Spin polarization of a 2D-electron gas and the magnetization problem of nano--particles. Physica E-Low-Dimensional Systems & Nano-structures, 2002. 12(1-4): p. 942-945.
40. Yamamoto, Y., et al., Direct observation of ferromagnetic spin polarization in gold nanoparticles. Physical Review Letters, 2004. 93(11).
41. Yamamoto, Y., et al., X-ray magnetic circular dichroism study of gold nanoparticles protected by

polymer. Journal of Magnetism and Magnetic Materials, 2004. 272: p. E1183-E1184.
42. Okazaki, K. and Y. Teraoka, Pencil-case structure in electron distribution of very thin film. Solid State Communications, 2000. 116(5): p. 269-272.
43. Okazaki, K. and Y. Teraoka, Magnetic structures in metallic thin films. Surface Science, 1999. 433: p. 672-675.
44. Hernando, A., et al., Giant magnetic anisotropy at the nano-scale: Overcoming the superparamagnetic limit. Physical Review B, 2006. 74(5).
45. LaShell, S., B.A. McDougall, and E. Jensen, Spin splitting of an Au(111) surface state band observed with angle resolved photoelectron spectroscopy. Physical Review Letters, 1996. 77(16): p. 3419-3422.
46. Koroteev, Y.M., et al., Strong spin-orbit splitting on Bi surfaces. Physical Review Letters, 2004. 93(4).
47. Petersen, L. and P. Hedegard, A simple tight-binding model of spin-orbit splitting of sp-derived surface states. Surface Science, 2000. 459(1-2): p. 49-56.
48. Teng, X.W., et al., Electronic and Magnetic Properties of Ultrathin Au/Pt Nano-wires. Nano- Letters, 2009. 9(9): p. 3177-3184.
49. Hori, H., et al., Anomalous magnetic polarization effect of Pd and Au nano--particles. Physics Letters A, 1999. 263(4-6): p. 406-410.
50. Taniyama, T., E. Ohta, and T. Sato, Observation of 4d ferromagnetism in free-standing Pd fine particles. Europhysics Letters, 1997. 38(3): p. 195-200.
51. Oba, Y., et al., Magnetic Intraparticle Structure in Ferromagnetic Pd Nano-particle. Journal of the Physical Society of Japan, 2009. 78(4).
52. Wienke, R., G. Schutz, and H. Ebert, Determination of Local Magnetic-Moments of 5d Impurities in Fe Detected Via Spin-Dependent Absorption. Journal of Applied Physics, 1991. 69(8): p. 6147-6149.
53. Thole, B.T., et al., X-ray Circular-Dichroism as a Probe of Orbital Magnetization. Physical Review Letters, 1992. 68(12): p. 1943-1946.
54. Neel, L.J., Phys. Radium, 1954. 15: p. 376-378.
55. Hernando, A., Magnetic properties and spin disorder in nano-crystalline materials. Journal of Physics-Condensed Matter, 1999. 11(48): p. 9455-9482.
56. Skomski, R., Nano-magnetics. Journal of Physics-Condensed Matter, 2003. 15(20): p. R841-R896.
57. Delin, A. and E. Tosatti, Magnetic phenomena in 5d transition metal nano-wires. Physical Review B, 2003. 68(14).
58. Sampedro, B., et al., Ferromagnetism in fcc twinned 2.4 nm size Pd nanoparticles. Physical Review Letters, 2003. 91(23).
59. Shinohara, T., T. Sato, and T. Taniyama, Surface ferromagnetism of Pd fine particles. Physical Review Letters, 2003. 91(19).
60. Brust, M., et al., Synthesis of Thiol-Derivatized Gold Nanoparticles in a 2-Phase Liquid-Liquid System. Journal of the Chemical Society-Chemical Communications, 1994(7): p. 801-802.
61. Singh, R.K. and D. Kumar, Pulsed laser deposition and characterization of high-T-c YBa2Cu3O7-x superconducting thin films. Materials Science & Engineering R-Reports, 1998. 22(4): p. 113-185.
62. Wende, H., Recent advances in X-ray absorption spectroscopy. Reports on Progress in Physics, 2004. 67(12): p. 2105-2181.
63. Eriksson, O., et al., Orbital Magnetism in Fe, Co, and Ni. Physical Review B, 1990. 42(4): p. 2707-2710.
64. Soderlind, P., et al., Spin and Orbital Magnetism in Fe-Co and Co-Ni Alloys. Physical Review B, 1992. 45(22): p. 12911-12916.
65. Ebert, H., et al., L-edge X-ray absorption in fcc and bcc Cu metal: Comparison of experimental and

first-principles theoretical results. Physical Review B, 1996. 53(23): p. 16067-16073.
66. J. StoK hr, Y.W., in: A.S. Schlachter, F.J. Wuilleumier(Eds.), New Directions in Research with Third-Generation Soft X-ray Synchrotron Radiation Sources. Kluwer Aca- demic Publishers, Netherlands, 1994: p. p. 221.
67. Stohr, J., Journal of Magnetism and Magnetic Materials. 1999(200): p. 470-497.
68. Carra, P., et al., X-ray Circular-Dichroism and Local Magnetic-Fields. Physical Review Letters, 1993. 70(5): p. 694-697.
69. Garzon, I.L., et al., Do thiols merely passivate gold nano-clusters? Physical Review Letters, 2000. 85(24): p. 5250-5251.
70. A. Tiwari, M.S., D. Kumar, J. T. Abiade, 2008. 92(062509).
71. T. Minami, H.S., H. Nanto, S. Takata, J. Appl. Phys., 1985: p. part 2, 24, L781.
72. Kuo, F.L., et al., A comparative study of the photoluminescence and conduction mechanisms of low temperature pulsed laser deposited and atomic layer deposited zinc oxide thin films. Physica Status Solidi a-Applications and Materials Science, 2010. 207(11): p. 2487-2491.
73. H. Kato, M.S., K. Miyamoto, T. Yao, 2002. 538(237–239).
74. C. G. Van de Walle, D.B.L., G. F. Neumark, and S. T. Pantelides, 1993. 47(9425).
75. D. C. Look, D.C.R., C. W. Litton, R. L. Jones, D. B. Eason, G. Cantwell, 2002. 81(1830).
76. Zunger, A., 2003. 83(57).
77. Wei, S.-H., 2004. 30(337).
78. Yan, Y.F., M.M. Al-Jassim, and S.H. Wei, Doping of ZnO by group-IB elements. Applied Physics Letters, 2006. 89(18).
79. Volnianska, O., et al., Theory of doping properties of Ag acceptors in ZnO. Physical Review B, 2009. 80(24).
80. Sun, L.J., et al., Effects of S incorporation on Ag substitutional acceptors in ZnO:(Ag, S) thin films. Solid State Communications, 2009. 149(39-40): p. 1663-1665.
81. H. S. Kang, B.D.A., J. H. Kim, G. H. Kim, S. H. Lim, H. W. Chang, S. Y. Lee, 2006. 88(202108).
82. Cao, Y.G., et al., Low resistivity p-ZnO films fabricated by sol-gel spin coating. Applied Physics Letters, 2006. 88(25).
83. Fujihara, S., C. Sasaki, and T. Kimura, Crystallization behavior and origin of c-axis orientation in sol-gel-derived ZnO : Li thin films on glass substrates. Applied Surface Science, 2001. 180(3-4): p. 341-350.
84. Turner, N.H. and A.M. Single, Determination of Peak Positions and Areas from Wide-Scan Xps Spectra. Surface and Interface Analysis, 1990. 15(3): p. 215-222.
85. Pireaux W.A., L.M., Thiry P.A., Delrue J.P., Caudano R., Surf. Sci., 1984. 141(221).
86. Juodkazis, K., et al., XPS studies on the gold oxide surface layer formation. Electrochemistry Communications, 2000. 2(7): p. 503-507.
87. Aita, C.R. and N.C. Tran, Core Level and Valence Band X-ray Photoelectron-Spectroscopy of Gold Oxide. Journal of Vacuum Science & Technology a-Vacuum Surfaces and Films, 1991. 9(3): p. 1498-1500.
88. Zhang, S.B., S.H. Wei, and A. Zunger, Intrinsic n-type versus p-type doping asymmetry and the defect physics of ZnO. Physical Review B, 2001. 63(7).
89. Abiade, J.T., et al., Structural and magnetic properties of self-assembled nickel nanoparticles in a yttria stabilized zirconia matrix. Thin Solid Films, 2008. 516(8): p. 2082-2086.
90. Melendrez, M.F., G. Cardenas, and M.S. Palencia, Colloidal Germanium Nanoparticles and Nano-cubes Synthesized by Chemical Liquid Deposition. Advanced Science Letters, 2011. 4(2): p. 526-535.

91. Simakin, A.V., et al., Nanoparticles produced by laser ablation of solids in liquid environment. Applied Physics a-Materials Science & Processing, 2004. 79(4-6): p. 1127-1132.
92. Link, S., et al., Laser-induced shape changes of colloidal gold nano-rods using femtosecond and nano-second laser pulses. Journal of Physical Chemistry B, 2000. 104(26): p. 6152-6163.
93. Waller, G.H., A. Stein, and J.T. Abiade, Nano-fabrication of doped, complex oxides. Journal of Vacuum Science & Technology B, 2012. 30(1).
94. Kumar, B. and R.K. Thareja, Synthesis of nanoparticles in laser ablation of aluminum in liquid. Journal of Applied Physics, 2010. 108(6).
95. Patil, P.P., et al., Pulsed-Laser Induced Reactive Quenching at a Liquid-Solid Interface - Aqueous Oxidation of Iron. Physical Review Letters, 1987. 58(3): p. 238-241.
96. Tang, E.J., et al., Surface modification of zinc oxide nano-particle by PMAA and its dispersion in aqueous system. Applied Surface Science, 2006. 252(14): p. 5227-5232.
97. Abiade, J.T., et al., A tribochemical study of ceria-silica interactions for CMP. Journal of the Electrochemical Society, 2006. 153(11): p. G1001-G1004.
98. Liufu, S.C., H.N. Xiao, and Y.P. Li, Effect of MA-Na copolymer adsorption on the colloidal stability of nano--sized ZnO suspension. Materials Letters, 2005. 59(27): p. 3494-3497.
99. Dange, C., et al., Adsorption mechanism and dispersion efficiency of three anionic additives [poly(acrylic acid), poly(styrene sulfonate) and HEDP] on zinc oxide. Journal of Colloid and Interface Science, 2007. 315(1): p. 107-115.
100. Liufu, S., H. Xiao, and Y.P. Li, Investigation of PEG adsorption on the surface of zinc oxide nanoparticles. Powder Technology, 2004. 145(1): p. 20-24.
101. Hong, N.H., et al., Room-temperature ferromagnetism observed in undoped semiconducting and insulating oxide thin films. Physical Review B, 2006. 73(13).
102. Sundaresan, A., et al., Ferromagnetism as a universal feature of nanoparticles of the otherwise nonmagnetic oxides. Physical Review B, 2006. 74(16).
103. Coey, J.M.D., d(0) ferromagnetism. Solid State Sciences, 2005. 7(6): p. 660-667.
104. Xing, G.Z., et al., Correlated d(0) ferromagnetism and photoluminescence in undoped ZnO nano-wires. Applied Physics Letters, 2010. 96(11).
105. Oba, F., et al., Defect energetics in ZnO: A hybrid Hartree-Fock density functional study. Physical Review B, 2008. 77(24).
106. Banerjee, S., et al., Enhancement of ferromagnetism upon thermal annealing in pure ZnO. Applied Physics Letters, 2007. 91(18).
107. Properties of Materials - Anisotropy, Symmetry and Structure - R. Newnham (Oxford, 2005)
108. Litran, R, et al, Magnetic and microstructural analysis of palladium nanoparticles with different capping systems, PHYSICAL REVIEW B, Volume: 73 Issue: 5, 2006

Appendix A:

Structural and Electrical Properties of Au-Doped Zinc Oxide Thin Films

Abstract

The structural and electrical properties of gold-doped zinc oxide (ZnO) thin films deposited by pulsed laser deposition (PLD) have been studied. Solid gold (Au) and ZnO targets were co-ablated during PLD in order to incorporate Au into the ZnO films. Hall measurements indicate that the Au-doped zinc oxide films are p-type with a carrier concentration of ~ 10^{20} cm^{-3}. X-ray photoelectron spectroscopy and photoluminescence spectroscopy results suggest that Au substitutes for zinc in the zinc oxide films.

Introduction

Zinc Oxide (ZnO) has generated broad interest for many diverse applications, such as transparent thin film transistors and other optoelectronic devices [70]. ZnO has three possible crystal structures; wurtzite, zincblende and rocksalt with wurtzite being the most thermodynamically stable at room temperature. UndopedZnO is intrinsically n-type with a density of around 10^{21} cm^{-3}[71] due to oxygen vacancies and zinc interstitials that serve as shallow donors.[72]n-type ZnO is also obtained by doping with group-III and group-VII elements [73]. However, p-type ZnO is difficult to prepare due to the formation of compensating native donor defects like oxygen vacancies and zinc interstitials. A further complication is the low solubility of many p-type dopants the ZnO[74]. A reliable method of preparing p-type ZnO is required in order to realize the potential of ZnO in applications, such as inexpensive, UV/blue light emitting diodes and other optoelectronics devices.

Therefore, doping ZnO p-type has been the focus of many studies, and it was predicted that nitrogen could serve as a shallow acceptor in ZnO. Experimentally, Look et al.[75], prepared N-doped p-type ZnO by molecular beam epitaxy with hole mobilities of ~ 2 cm^2/s. However, nitrogen is not very soluble in ZnO, which limits the mobility of the carriers. On the other hand, group-I elements were considered as dopants, but later abandoned because of their tendency to occupy interstitial rather than substitutional lattice sites [76, 77].

Group-IB elements like Au, Ag and Cu have been suggested as possible p-type dopants in ZnO due to their similarity in ionic radii with Zn, which makes doping of substitutional sites preferable [78]. Group IB elements, such as Cu and Ag, when implanted on substitutional Zn sites, have proven to be good candidates as shallow acceptors in ZnO nano-structures [78-80]. Kang et al. reported the observation of p-type ZnO doped with Ag, which supported the idea that Group-IB elements are good candidates as dopants in p-type ZnO[81].

So far p-type ZnO doped by Au has not been achieved yet. One of difficulties is the solubility of Au into ZnO is comparatively low. In this paper, we report recent results on our efforts to obtain p-type ZnO by co-ablation of Au and ZnO targets during pulsed laser deposition (PLD). Au has been embedded into ZnOlattice . Precipitates of gold have formed too. The stability of p-type doped ZnO will be tested in our future work.

Experimental

Au-doped ZnO samples were prepared by alternate ablation of a pure ZnO and Au targets onto c-plane sapphire substrates by pulsed laser deposition. Each cycle consisted of 50 pulses on the ZnO target and 40 laser pulses on the Au target. This cycle was repeated 80 times for a total of 4000 pulses on the ZnO target and 3200 laser pulses on the Au target. The samples were ablated in vacuum with pressure of ~10^{-6}torr using a 248 nm KrF laser and energy density of 3 J/cm^2. The laser repetition rate and substrate temperature were kept constant at 10 Hz and room temperature, respectively. A pure ZnO sample was prepared in the same system with 4000 pulses under identical conditions. Microstructural investigations were carried out by X-ray photoelectron spectroscopy (XPS) and transmission electron microscopy using a XPS system and JEOL3010 100kV microscope, respectively. The optical and electrical characteristics of the samples were characterized by photoluminescence spectroscopy and Hall measurements using a reconfigurable optical bench, and an Ecopia HMS5000 Hall system.

A-4 Results and discussion

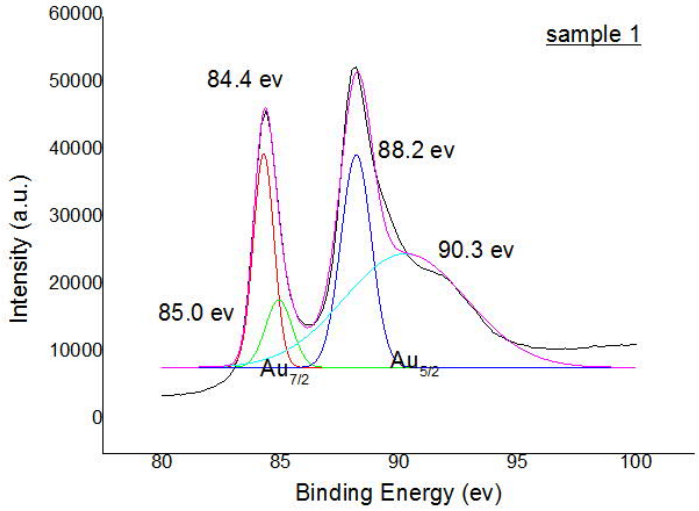

Figure A-1: XPS results of Au peaks for Au doped ZnO thin film.

Table A-1 is a summary of representative electrical properties of Au-doped and pure ZnO films characterized by Hall measurements. The ZnO thin films are the only contributors to the conductive features because the Al_2O_3 substrates are insulating. The Hall measurements of the Au-doped ZnO sample indicated a resistivity of 0.389Ω/cm, a Hall mobility of 0.05 $cm^2\ V^{-1}\ s^{-1}$, and a hole concentration of $+3.18 \times 10^{20}\ cm^{-3}$. Measurements on pure ZnO film grown under similar conditions reveal a resistivity of 0.284Ω/cm, a Hall mobility of 1.80 $cm^2\ V^{-1}\ s^{-1}$, and an electron concentration of $-1.85 \times 10^{19}\ cm^{-3}$. Consistent with other reports [82], we found very low resistivity in the Au-ZnO sample, which is necessary for future semiconductor applications.

The chemical bonding states of Au, Zn and O in the films were examined by XPS analysis and the results are shown in Figure A-1. The 2p electron binding energy of Zn in the XPS spectrum results (not shown) is attributed to Zn-O bonding. It has been reported that the binding energy of Zn participating in Zn–O bonds in bulk ZnO is 530.6 eV, and the binding energy of chemisorbed oxygen onto zinc is 531.8 eV[83]. Au is detected in the ZnO film. The two peaks at 84.4 eV and 88.2 eV can be attributed to metallic gold, whereas the ones at 85.0 eV and 90.3 eV are attributed to Au–O bonds as reported elsewhere [15]. The XPS results suggests that Au occupies Zn sites in the state of Au+ ions in the Au-doped ZnO thin film

[84-87]. In this case the Au+ ions act as acceptors and are responsible for the measured p-type electrical conductivity.

Table A-1: Hall-effect measurements of Au-doped ZnO and Pure ZnO

Samples	Bulk concentration (cm^{-3})	Resistivity (Ω/cm)	Conductivity	Hall mobility ($cm^2\ V^{-1}\ s^{-1}$)	Carrier type
Au-doped ZnO	3.18E+20	0.389	2.57	0.05	P
Pure ZnO	-1.85E+19	0.284	3.52	1.80	N

Figure A-2 shows a plane-view image of the Au-ZnO sample showing regions of the ZnO thin film and the gold particles that resulted formed due to Au precipitation. Generally there are two main features throughout the sample, a lighter phase that corresponds to the ZnO thin film and darker regions that represent Au precipitates. The mean size of the gold precipitates is ~ 5 nm. Considering that gold and ZnO targets are ablated separately, the formation of Au Nps in ZnO thin film indicates that the amount of Au is over the maximun solubility in the system and precipitates starts to form after gold embedded into and bonded with ZnO film, which is also supported by XPS bonding information. The electric carriers of metals are electrons which are n type, as a result, the observed Au precipitates are not responsible for the p-type properties in the system.

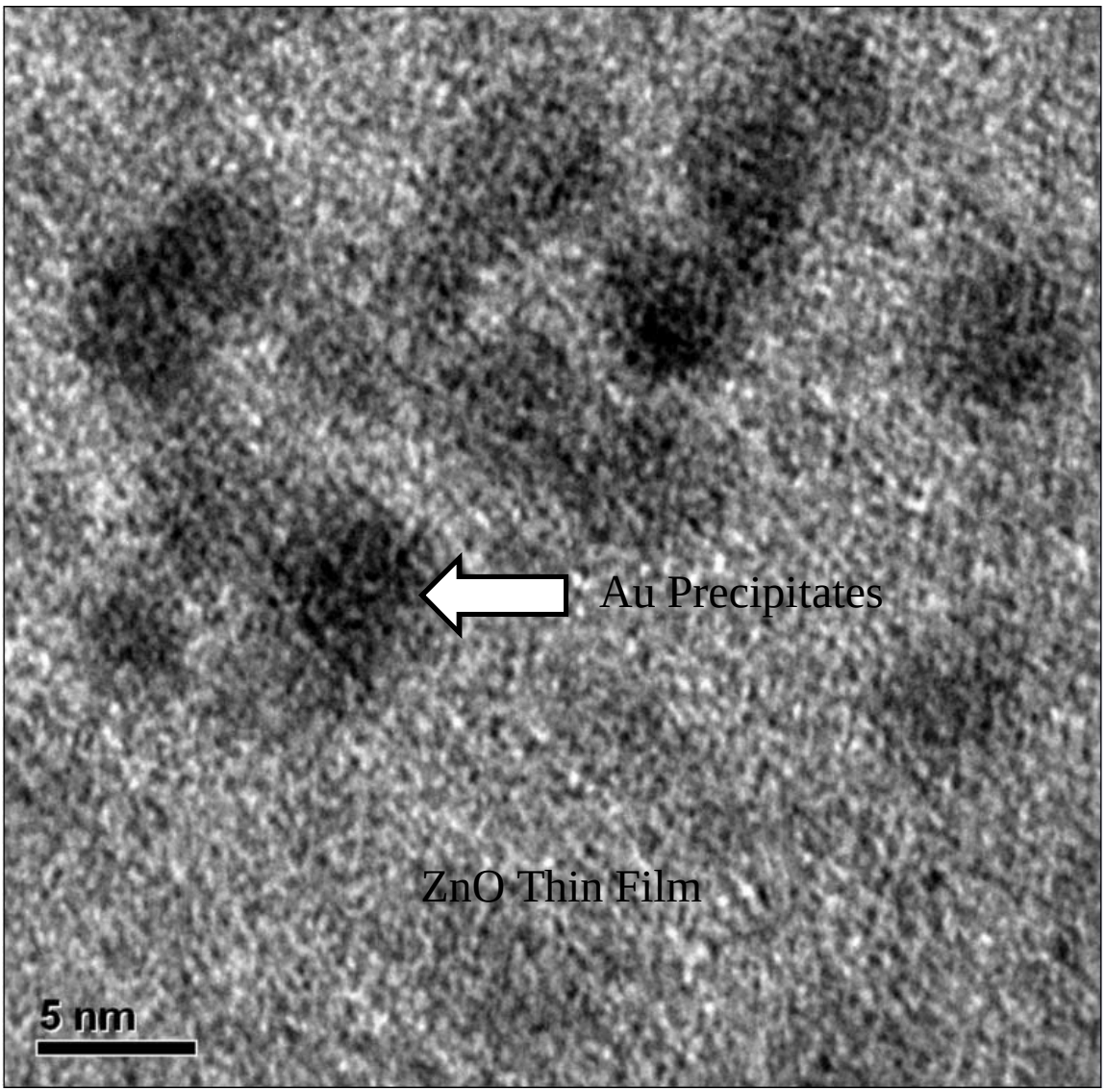

Figure A-2 TEM image of Au-doped ZnO film showing Au precipitates that formed in the bulk of the ZnO film

Photoluminescence (PL) measurements were carried out at room temperature, with an excitation wavelength of 340 nm for both samples. . The PL spectra are shown in Figure A-3. The PL of the pure ZnO sample is characterized by a shoulder around 400nm, a sharp peak at 424 nm, and a comparatively deep level emission at 544 nm. The Au doped sample exhibits two distinct peaks at 398 nm and 435 nm, a shoulder around 465nm and a broad emission band in the green and red spectral regions. We speculate that the appearance of these new spectral features in the Au doped ZnO samples is associated with the formation of new structural defects that are associated with the structural reorganization that accompanies the incorporation of Au.

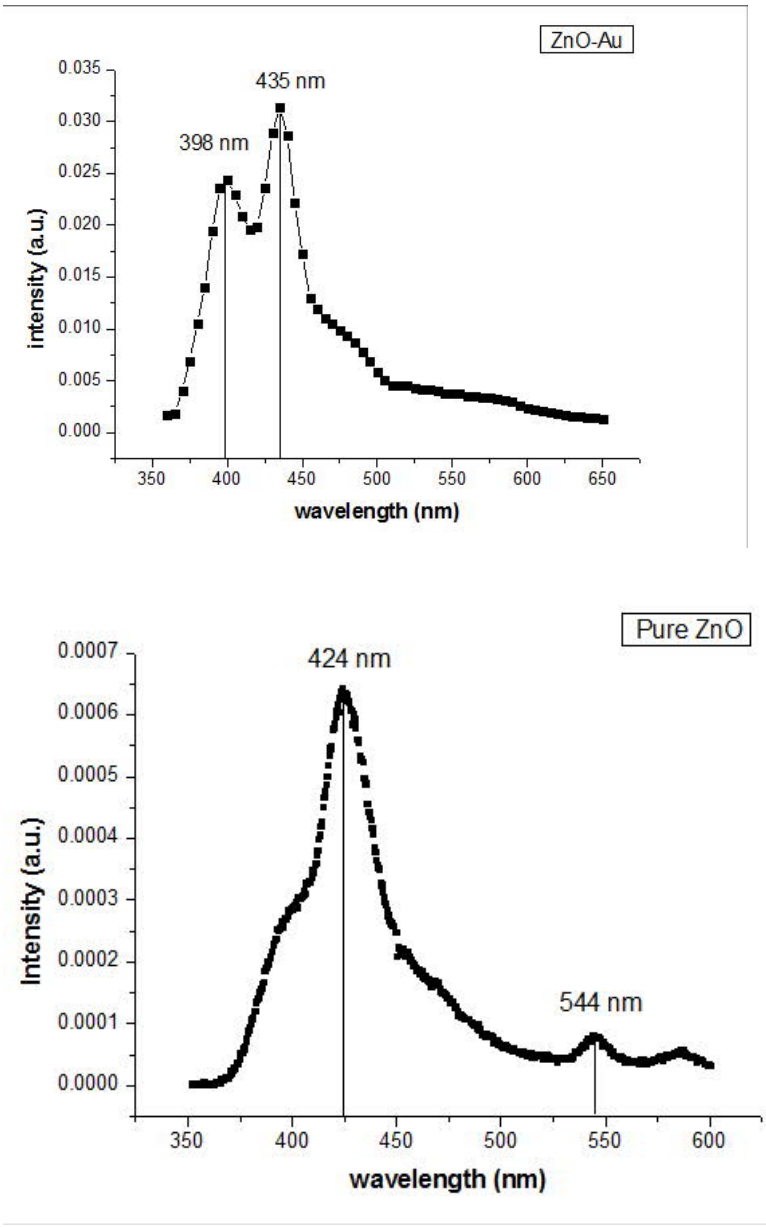

Figure A-3 Photoluminescence spectra of Pure ZnO (BOTTOM) and ZnO-Au (TOP)

Yan et al.[78] calculated the formation energy of substitutional group-IB elements in ZnO, and showed that the energy level position for Au substitutional dopant on a Zn site is comparable to that of substitutional nitrogen on the oxygen sites in ZnO. Since our p-type sample was prepared in vacuum which is an oxygen-poor condition, and in considering the results of the electrical and optical measurements, we speculate that oxygen rich conditions may not be necessary for the suppression self-compensating hole-killer defects, such as oxygen vacancies and Zn interstitials [88].

In conclusion, we used pulsed laser deposition to prepare p-type ZnO thin film by doping

with Au. The carrier type and concentration was confirmed by Hall Effect measurements. XPS results further confirmed such the bonding of Au to O, which was taken as an indication of substitutional Au on Zn sites. Our results indicate that oxygen rich condition may not be a key factor for achieving p-type ZnO thin films.

Reference：

1. A. Tiwari, M.S., D. Kumar, J. T. Abiade, 2008. 92(062509).
2. T. Minami, H.S., H. Nanto, S. Takata, J. Appl. Phys., 1985: p. part 2, 24, L781.
3. Kuo, F.L., et al., A comparative study of the photoluminescence and conduction mechanisms of low temperature pulsed laser deposited and atomic layer deposited zinc oxide thin films. Physica Status Solidi a-Applications and Materials Science, 2010. 207(11): p. 2487-2491.
4. H. Kato, M.S., K. Miyamoto, T. Yao, 2002. 538(237–239).
5. C. G. Van de Walle, D.B.L., G. F. Neumark, and S. T. Pantelides, 1993. 47(9425).
6. D. C. Look, D.C.R., C. W. Litton, R. L. Jones, D. B. Eason, G. Cantwell, 2002. 81(1830).
7. Zunger, A., 2003. 83(57).
8. Wei, S.-H., 2004. 30(337).
9. Yan, Y.F., M.M. Al-Jassim, and S.H. Wei, Doping of ZnO by group-IB elements. Applied Physics Letters, 2006. 89(18).
10. Volnianska, O., et al., Theory of doping properties of Ag acceptors in ZnO. Physical Review B, 2009. 80(24).
11. Sun, L.J., et al., Effects of S incorporation on Ag substitutional acceptors in ZnO:(Ag, S) thin films. Solid State Communications, 2009. 149(39-40): p. 1663-1665.
12. H. S. Kang, B.D.A., J. H. Kim, G. H. Kim, S. H. Lim, H. W. Chang, S. Y. Lee, 2006. 88(202108).
13. Cao, Y.G., et al., Low resistivity p-ZnO films fabricated by sol-gel spin coating. Applied Physics Letters, 2006. 88(25).
14. Fujihara, S., C. Sasaki, and T. Kimura, Crystallization behavior and origin of c-axis orientation in sol-gel-derived ZnO : Li thin films on glass substrates. Applied Surface Science, 2001. 180(3-4): p. 341-350.
15. Turner, N.H. and A.M. Single, Determination of Peak Positions and Areas from Wide-Scan Xps Spectra. Surface and Interface Analysis, 1990. 15(3): p. 215-222.
16. Pireaux W.A., L.M., Thiry P.A., Delrue J.P., Caudano R., Surf. Sci., 1984. 141(221).
17. Juodkazis, K., et al., XPS studies on the gold oxide surface layer formation. Electrochemistry Communications, 2000. 2(7): p. 503-507.
18. Aita, C.R. and N.C. Tran, Core Level and Valence Band X-ray Photoelectron-Spectroscopy of Gold Oxide. Journal of Vacuum Science & Technology a-Vacuum Surfaces and Films, 1991. 9(3): p. 1498-1500.
19. Zhang, S.B., S.H. Wei, and A. Zunger, Intrinsic n-type versus p-type doping asymmetry and the defect physics of ZnO. Physical Review B, 2001. 63(7).

Appendix B:

Ferromagnetic ZnO Nanoparticles Prepared by Pulsed Laser Deposition in Liquid

Abstract:

Pulsed laser ablation (PLA) has recently been used to synthesize metal and ceramic nano-structures. The PLA method is highly advantageous because nano-particle (NPs) synthesis is possible without organic binders or expensive equipment required to obtain high vacuum. In this letter we report on the synthesis and magnetic properties of ZnO nanoparticles by PLA of a solid ZnO target in water. The mean size of the ZnO NPs is ~ 100 nm after dispersion. The ZnO NPs show clear characteristics of room temperature ferromagnetism. The saturation moment (Ms) of the ZnO NPs is almost unchanged with temperature, which suggests the fundamental mechanism is different than the traditional double exchange model. So called d0 magnetism has been invoked to explain the magnetic characteristics.

Introduction

The preparation of NPs by pulsed laser ablation (PLA) of solid targets in vacuum or gas [19, 89] or reaction of appropriate chemicals using liquid-based techniques [90] has been widely studied. Chemical-based techniques usually require comparatively long processing times. Alternatively, physical-based methods like pulsed laser deposition require high vacuum or a stable gas pressure, which necessitates the use of expensive equipment. Liquid-based techniques have emerged as the most popular for synthesis of nano-structures of various morphologies. However, the various techniques generally suffer from one or more of the following: 1) low yield, 2) compositional inhomogeneity, 3) hazardous chemical wastes, 4) particle agglomeration, 5) need for multiple synthesis steps and 6) difficulty with scale-up for large-scale production. PLA of solid targets in liquids combines the compositional control of vacuum deposition techniques and morphological control of liquid-based synthesis approaches.

PLA in liquids is a chemically simple and clean synthesis technique that is performed at ambient temperatures and pressures [91, 92]. The laser parameters (frequency, energy, wavelength, etc.) and the laser-solid interactions [93] are the most important processing factors in PLA in liquid media [94]. The popularity of PLA in liquid media is due to the possibility of direct formation of metastable phases that exist in high temperature and high-pressure regions of phase diagrams. This capability is due to the high temperature and high pressures generated during laser ablation in liquids and the high density of ablated species in the confining liquid.[95]The simplicity of the technique also facilitates investigation of intriguing nano-scale physical phenomena like the recently reported ferromagnetism in un-doped oxide nano-structures.

In this letter we report on the synthesis and magnetic properties of ZnO nanoparticles by PLA. In order to examine whether ferromagnetism is an intrinsic property of such oxides, a bare ZnO NP sample was prepared without any doping or organic coating. The nanoparticles were synthesized by ablation of a solid ZnO target immersed in water.

Experiment

We prepared ZnO nano-structures in de-ionized water by laser ablation on corresponding bulk targets immersed in liquid, which is shown in Figure B-1. The target was fixed on the top of the liquid encapsulated target holder, whose window is transparent to the incoming KrFexcimer laser with wavelength of 248nm. The target holder was designed so that the target would be exactly at the focal point of the lens. All the experiments were performed at room temperature. Several samples were made by altering the total number of laser pulses, or laser energy, at a laser frequency of 10 Hz. Microstructural investigations were carried out at the Nano-scale Characterization and Fabrication Laboratory (NCFL) using the LEO (Zeiss) 1550 scanning electron microscope (SEM). The elemental composition of the samples was determined during TEM investigation by energy dispersive X-ray spectroscopy (EDS). Since the particles were dispersed in water, a drop of liquid was taken and allowed to dry on a silicon wafer for SEM analysis. The magnetic properties of ZnO NPs were measured using a physical property measurement system (PPMS) equipped with a

vibrating sample magnetometer. Moment versus magnetic field loops (MH loops) were performed at various magnetic fields.

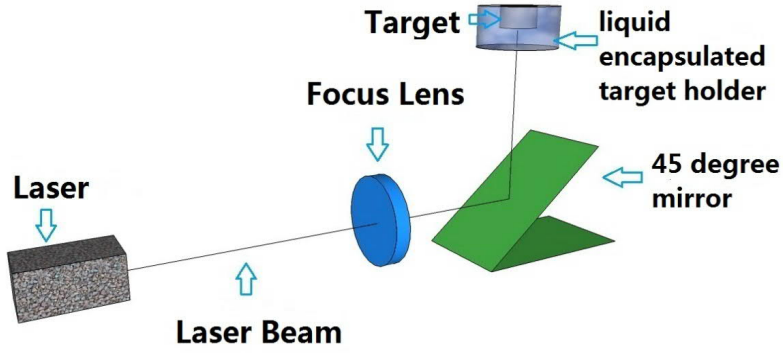

Figure B-1 Schematic diagram of a custom built PLA system

We synthesized ZnO nanoparticles in water by varying the number of laser pulses on a solid ZnO target. The number of pulses was varied from 5,000 pulses (Sample A), to 10,000 pulses (Sample B) and 12,000 pulses (Sample C). We chose 5,000 pulses as the minimum number of laser pulses to ensure the amount of particles in the sample was sufficient for characterization. The laser energy was kept constant at 135mJ. The center of the beam was carefully located near the center of ZnO target. After each deposition, the target was rotated to ensure uniform ablation during the next run. Each sample contained 5 ml of de-ionized water. The encapsulated target holder was sealed during deposition, which reduced contamination from air.

Results and discussion

Morphology characterization

The number of laser pulses on the ZnO target was varied to understand the effect of laser irradiation on particle morphology. SEM analysis of the samples suggests that as the total numbers of laser pulses is increased, the concentration of particles inside the liquid also increases dramatically. However, the mean size of ZnO nanoparticles is nearly constant. A

small number of larger clusters formed during ablation, which is expected, because the surface energy of nano-structured ZnO is high, driving particle agglomeration[96]. The clusters are non-spherical with sizes ~ 100 nm.

The SEM images of sample C before dispersion (not shown) indicate the changes in ZnO morphology from separated NPs to clustered NPs due to agglomeration is more pronounced when the number of laser pulses on the target was increased to 12,000. The clustered NPs are randomly oriented and some are intertwined, connected particles with appearance similar to nano-rods.

A drop of the ZnO nano-particle solution was allowed to dry on a silicon wafer for elemental analysis using SEM with a built-in EDS detector. The EDS analysis was carried out under mapping mode in order to get average concentration over a large area. As shown in Table B-1, carbon, zinc, silicon and oxygen were detected. Zn and O are from our NPs and Si is from the wafer that was used as support for the NPs during microscopy analysis. Carbon contamination was also detected, which is unavoidable. The EDS results also suggest that the amount of ZnO increases with an increase in the number of laser pulses on the target.

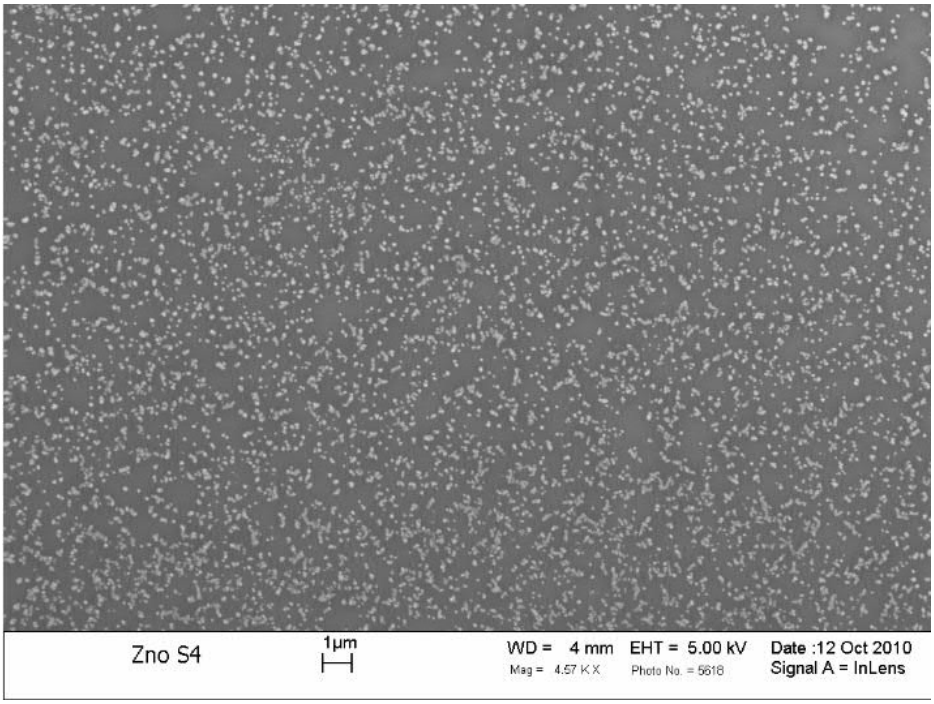

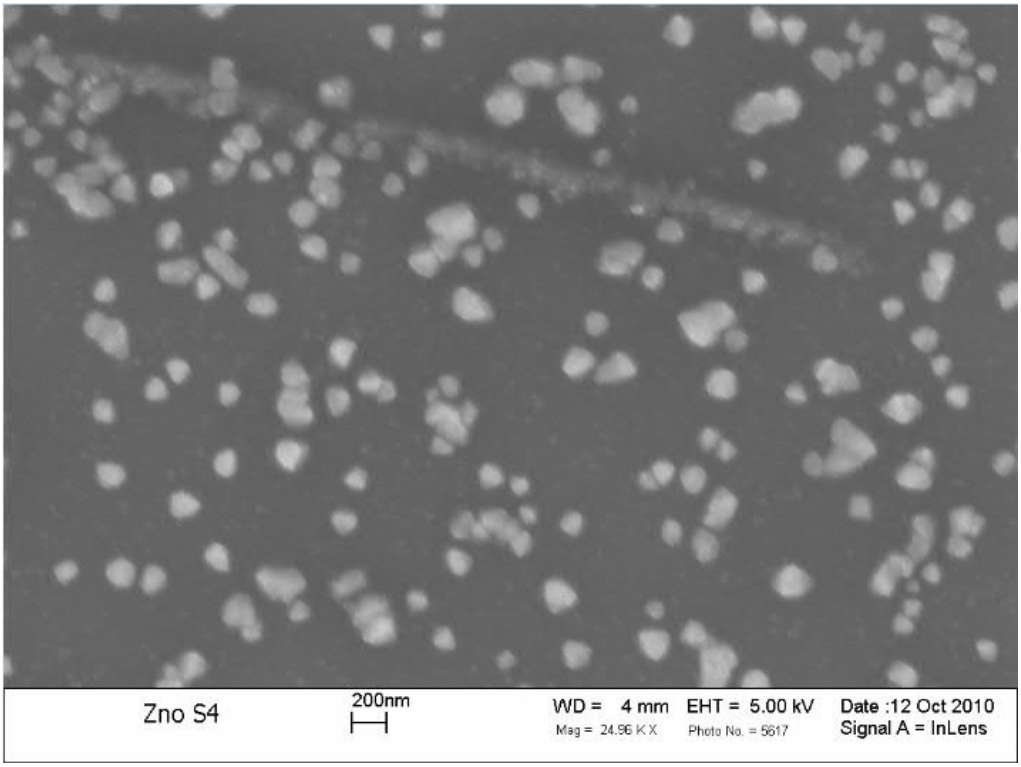

Figure B-2: SEM image (top) and (bottom) showing dispersed ZnO NPs (Sample C)

Figure B-2 clearly demonstrates the efficacy of PLA for the synthesis of nanoparticles. It should be noted that a wide variety of targets may be used as long as the properties of the liquid allow sufficient coupling of the incoming laser radiation with the target. The increase in NP agglomeration with increasing number of laser pulses may be mitigated by controlling the particle concentration, which is related to the number of laser shots on the target. Alternately, pH-adjusting additives and/or surfactants may be used to stabilize the dispersion.

As indicated in Figure B-2, NP agglomeration became appreciable in sample C made with 12,000 laser pulses on the target. The high surface energy ZnO NPs form interconnected particles by Zn–O–Zn bonding promoted by the existence of water molecules, which impedes the separation of ZnO nanoparticles. The removal of such bonding after preparation was utilized to reduce the number of hard agglomerates in the suspension. In the absence of stabilizing agents, the NP may agglomerate quickly, resulting particles of larger effective diameter[97]. We dispersed the ZnO sample C with poly (acrylic acid) (PAA, MW 1800, Aldrich, St Louis, MO) with repeat unit [-CH2CH (CO2H)-]. Since high pH promotes PAA dispersant adsorption onto ZnO surfaces [98, 99], NH4OH was used to adjust the suspension

to pH of ~ 9.5, which is close to the isoelectric point of ZnO.[100] The SEM image in Figure B-2 was captured after dispersion showing the monodispersed particle size is ~ 100 nm.

Magnetic characterization

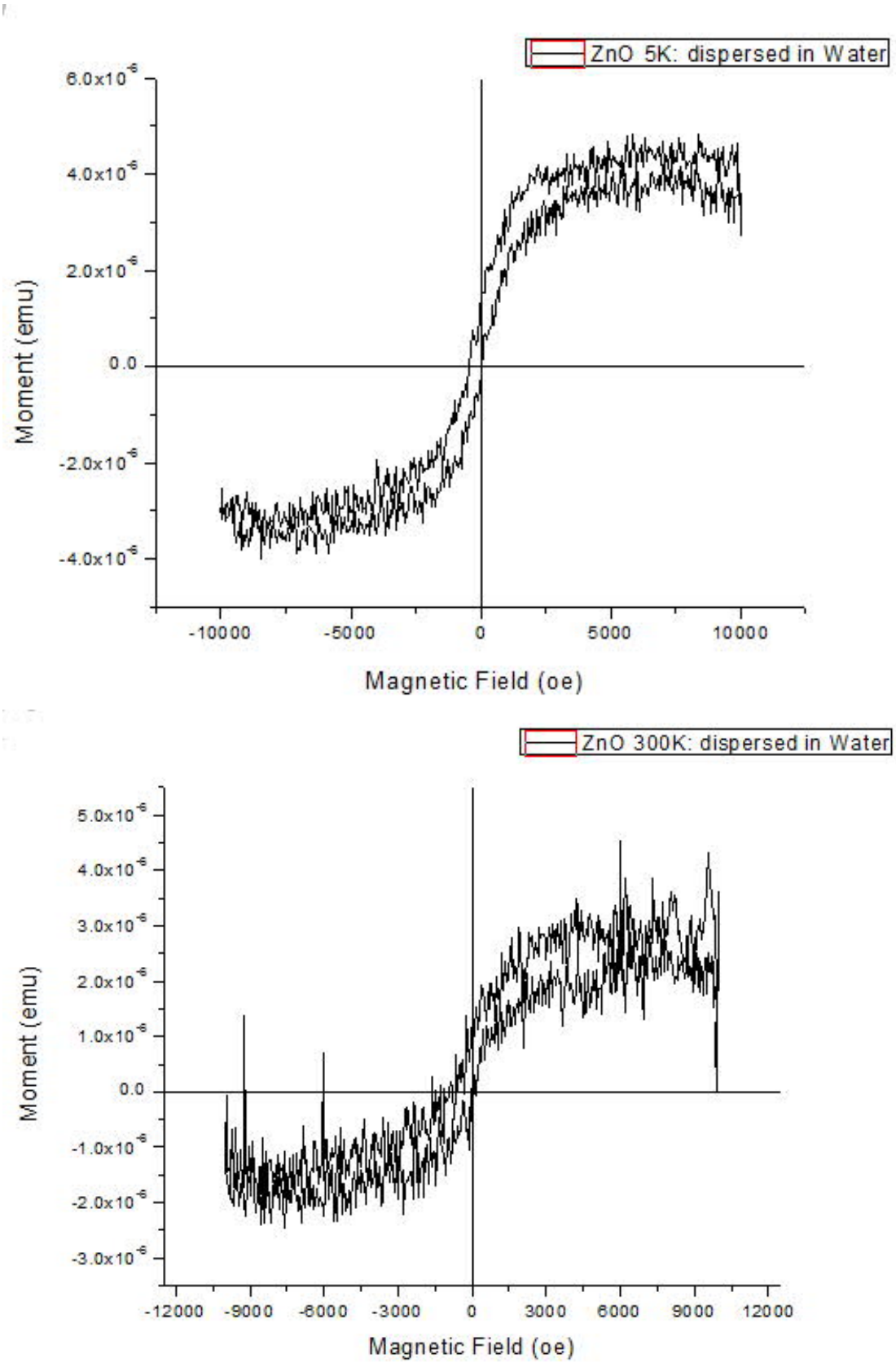

Figure B-3: Magnetic hysteresis loop at 5K (top) and 300K (bot) of ZnO NPs

It was found that ferromagnetism can be observed in undoped semiconducting and insulating oxide thin films, such as TiO2, HfO2, and In2O3[101]. Sundaresan'set al. reported ferromagnetism in CeO2, Al2O3, ZnO, In2O3, and SnO2 NPs. The room temperature magnetic signals in various oxide nanoparticles have been attributed to exchange interactions between localized electron spin moments coming from oxygen vacancies at the surfaces of the nanoparticles [102].

Our experimental approach allows us to test this observation by direct synthesis of oxide nanoparticles with desired composition. In Figure B-3, we plot moment versus field of dispersed ZnO NPs sample at 5K and 300K. The original data, which contains signals from both Si and ZnO, has a diamagnetic contribution resulting from the Si wafer. We obtained the MH loop for ZnO NPs by subtracting the linear diamagnetic contribution from Si. Both loops at 5K and 300K show ferromagnetic characteristics of hysteresis with coercivity and remanence. The saturation moment (Ms) is ~ 10-6 emu. It is also noticeable that Ms only slightly decreases when the measurement temperature was increased to 300K, which indicates the mechanism of magnetization is completely different from traditional double exchange model. Recently, such observations in other oxides such as In2O3, and SnO_2 which were reported by Sundaresan's group [102], were attributed to unpaired electrons on the surface of oxide NPs. Another possible explanation was initially termed as d0 magnetism [103]. It was suggested that the magnetism can possibly result from partially or fully filled d orbitals derived from Zn atoms coordinating oxygen vacancies (VO) [104]. Our ZnO NPs were produced in water, which is a poor oxidant. In such circumstances, oxygen vacancies always result in nonstoichiometry[105]. A sizable magnetic moment may be detected due to the presence of oxygen vacancies [106].

Conclusion

In summary, ZnO NPs were prepared by pulsed laser ablation in liquid. The mean size of the particles is only related to laser parameters like energy and repetition rate and not the number of laser pulses. An increase in the number of laser pulses on the target results only in

an increase in the particle concentration. The ZnO particles were ferromagnetic with characteristic features of remanence and coercivity at 300K. The unchanged Ms indicates the mechanism dominating such magnetic behavior is completely different from traditional models wherein Ms is a function of temperature. A theory based on d0 ferromagnetism is a possible theoretical support for our observation of ferromagnetism in the ZnO NPs.

Table B-1: SEM/EDS elemental analysis of samples B and C.

Sample	Element	Weight%	Atomic%
Sample C: ZnO 12,000	C	6.83	15.75
	O	4.71	8.16
	Si	68.66	67.71
	Zn	19.79	8.39
Sample B: ZnO10,000	C	9.30	19.21
	O	6.56	10.18
	Si	76.75	67.81
	Zn	7.39	2.81

Reference

1. Yamamoto, Y., et al., Direct observation of ferromagnetic spin polarization in gold nanoparticles. Physical Review Letters, 2004. 93(11).
2. Teng, X.W., et al., Electronic and Magnetic Properties of Ultrathin Au/Pt Nano-wires. Nano- Letters, 2009. 9(9): p. 3177-3184.
3. Crespo, P., et al., Permanent magnetism, magnetic anisotropy, and hysteresis of thiol-capped gold nanoparticles. Physical Review Letters, 2004. 93(8).
4. Zhang, P. and T.K. Sham, X-ray studies of the structure and electronic behavior of alkanethiolate-capped gold nanoparticles: The interplay of size and surface effects. Physical Review Letters, 2003. 90(24).
5. Hori, H., et al., Anomalous magnetic polarization effect of Pd and Au nano--particles. Physics Letters A, 1999. 263(4-6): p. 406-410.
6. Dutta, P., et al., Magnetism in dodecanethiol-capped gold nanoparticles: Role of size and capping agent. Applied Physics Letters, 2007. 90(21).
7. Hernando, A., et al., Giant magnetic anisotropy at the nano-scale: Overcoming the superparamagnetic limit. Physical Review B, 2006. 74(5).
8. de la Venta, J., et al., Magnetism in polymers with embedded gold nanoparticles. Advanced Materials, 2007. 19(6): p. 875-+.
9. Negishi, Y., et al., X-ray magnetic circular dichroism of size-selected, thiolated gold clusters. Journal of the American Chemical Society, 2006. 128(37): p. 12034-12035.
10. Liu, H.J., et al., Electronic structure of ensembles of gold nanoparticles: Size and proximity effects. Physical Review B, 2005. 72(15).
11. Novakovic, R., E. Ricci, and F. Gnecco, Surface and transport properties of Au-In liquid alloys. Surface Science, 2006. 600(23): p. 5051-5061.
12. Yamamoto, Y. and H. Hori, Direct observation of the ferromagnetic spin polarization in gold nanoparticles: A review. Reviews on Advanced Materials Science, 2006. 12(1): p. 23-32.
13. Yamamoto, Y., et al., Direct observation of ferromagnetic spin polarization in gold nanoparticles (vol 93, pg 116801, 2004). Physical Review Letters, 2006. 96(13).
14. J.T. Abiade, S.H.O., S. Pennycook, D. Christen, J. Thompson, and D. Kumar, Synthesis and Characterization of magnetic gold nanoparticles. MRS Spring Meeting, 2007. 9-13.
15. Luo, W., S.J. Pennycook, and S.T. Pantelides, s-electron ferromagnetism on gold and silver nano-clusters. Nano- Letters, 2007. 7(10): p. 3134-3137.
16. Magyar, R.J., et al., Density-functional study of magnetism in bare Au nano-clusters: Evidence of permanent size-dependent spin polarization without geometry relaxation. Physical Review B, 2007. 75(14).
17. Michael, F., et al., Size dependence of ferromagnetism in gold nanoparticles: Mean field results. Physical Review B, 2007. 76(22).
18. Phala, N.S. and E. van Steen, Intrinsic reactivity of gold nanoparticles: Classical, semi-empirical and DFT studies. Gold Bulletin, 2007. 40(2): p. 150-153.
19. Abiade, J.T., et al., The effect of matrix and substrate on the coercivity and blocking temperature of self-assembled Ni nanoparticles. Journal of Applied Physics, 2008. 104(7).
20. Tiwari, A., et al., Ferromagnetism in Cu-doped ZnO films: Role of charge carriers. Applied Physics Letters, 2008. 92(6).
21. Brivio, S., et al., Effects of Au nanoparticles on the magnetic and transport properties of

La(0.67)Sr(0.33)MnO(3) ultrathin layers. Physical Review B, 2010. 81(9).
22. Deng, S.Z., et al., Thiol-Capped ZnO Nano-wire/Nano-tube Arrays with Tunable Magnetic Properties at Room Temperature. Acs Nano-, 2010. 4(1): p. 495-505.
23. Costelle, L., et al., Spin-glass magnetism of surface rich Au cluster film. Applied Physics Letters, 2011. 99(2).
24. Hernando, A., et al., Revisiting magnetism of capped Au and ZnO nanoparticles: Surface band structure and atomic orbital with giant magnetic moment. Physica Status Solidi B-Basic Solid State Physics, 2011. 248(10): p. 2352-2360.
25. Ayuela, A., et al., sp magnetism in clusters of gold thiolates. New Journal of Physics, 2012. 14.
26. Hori, H., et al., Diameter dependence of ferromagnetic spin moment in Au nano-crystals. Physical Review B, 2004. 69(17).
27. Burgos, M., et al., Gold, silver and palladium complexes with the 2,2'-dipyridylamine ligand. European Journal of Inorganic Chemistry, 2003(11): p. 2170-2174.
28. Crespo, P., et al., Permanent magnetism in thiol-capped nanoparticles, gold and ZnO. Acta Physica Polonica A, 2008. 113(1): p. 515-520.
29. Crespo, P., et al., Fe impurities weaken the ferromagnetic behavior in Au nanoparticles. Physical Review Letters, 2006. 97(17).
30. Crespo, P., et al., Influence of the Capping Molecule on the Magnetic Behavior of Thiol-Capped Gold Nanoparticles. Ieee Transactions on Magnetics, 2008. 44(11): p. 2768-2771.
31. de la Venta, J., et al., Size Dependent Ferromagnetic-Like Behavior in Thiol Capped Gold Nanoparticles. Science of Advanced Materials, 2009. 1(3): p. 241-248.
32. De La Venta, J., et al., Magnetic properties of organic coated gold surfaces. Modern Physics Letters B, 2007. 21(6): p. 303-319.
33. Guerrero, E., et al., Magnetometry and electron paramagnetic resonance studies of phosphine- and thiol-capped gold nanoparticles. Journal of Applied Physics, 2010. 107(6).
34. Guerrero, E., et al., Electronic structure, magnetic properties, and microstructural analysis of thiol-functionalized Au nanoparticles: role of chemical and structural parameters in the ferromagnetic behaviour. Journal of Nano-particle Research, 2008. 10: p. 179-192.
35. Guerrero, E., et al., Surface plasmon resonance and magnetism of thiol-capped gold nanoparticles. Nano-technology, 2008. 19(17).
36. Guerrero, E., et al., Evolution of the microstructure, chemical composition and magnetic behaviour during the synthesis of alkanethiol-capped gold nanoparticles. Acta Materialia, 2007. 55(5): p. 1723-1730.
37. Hernando, A., P. Crespo, and M.A. Garcia, Metallic magnetic nanoparticles. Thescientificworldjournal, 2005. 5: p. 972-1001.
38. Hernando, A., P. Crespo, and M.A. Garcia, Origin of orbital ferromagnetism and giant magnetic anisotropy at the nano-scale. Physical Review Letters, 2006. 96(5).
39. Munoz-Marquez, M.A., et al., Permanent magnetism in phosphine- and chlorine-capped gold: from clusters to nanoparticles. Journal of Nano-particle Research, 2010. 12(4): p. 1307-1318.
40. Hori, H., et al., Magnetic properties of nano--particles of Au, Pd and Pd/Ni alloys. Journal of Magnetism and Magnetic Materials, 2001. 226: p. 1910-1911.
41. Suzuki, M., et al., Measurement of a Pauli and Orbital Paramagnetic State in Bulk Gold Using X-ray Magnetic Circular Dichroism Spectroscopy. Physical Review Letters, 2012. 108(4).
42. Takahashi, N., et al., Output properties of C-60 field-effect transistors with different source/drain

electrodes. Applied Physics Letters, 2007. 90(8).
43. Taki, M., et al., Spin polarization of a 2D-electron gas and the magnetization problem of nano--particles. Physica E-Low-Dimensional Systems & Nano-structures, 2002. 12(1-4): p. 942-945.
44. Yamamoto, Y., et al., X-ray magnetic circular dichroism study of gold nanoparticles protected by polymer. Journal of Magnetism and Magnetic Materials, 2004. 272: p. E1183-E1184.
45. Okazaki, K. and Y. Teraoka, Pencil-case structure in electron distribution of very thin film. Solid State Communications, 2000. 116(5): p. 269-272.
46. Okazaki, K. and Y. Teraoka, Magnetic structures in metallic thin films. Surface Science, 1999. 433: p. 672-675.
47. LaShell, S., B.A. McDougall, and E. Jensen, Spin splitting of an Au(111) surface state band observed with angle resolved photoelectron spectroscopy. Physical Review Letters, 1996. 77(16): p. 3419-3422.
48. Koroteev, Y.M., et al., Strong spin-orbit splitting on Bi surfaces. Physical Review Letters, 2004. 93(4).
49. Petersen, L. and P. Hedegard, A simple tight-binding model of spin-orbit splitting of sp-derived surface states. Surface Science, 2000. 459(1-2): p. 49-56.
50. Taniyama, T., E. Ohta, and T. Sato, Observation of 4d ferromagnetism in free-standing Pd fine particles. Europhysics Letters, 1997. 38(3): p. 195-200.
51. Oba, Y., et al., Magnetic Intraparticle Structure in Ferromagnetic Pd Nano-particle. Journal of the Physical Society of Japan, 2009. 78(4).
52. Wienke, R., G. Schutz, and H. Ebert, Determination of Local Magnetic-Moments of 5d Impurities in Fe Detected Via Spin-Dependent Absorption. Journal of Applied Physics, 1991. 69(8): p. 6147-6149.
53. Thole, B.T., et al., X-ray Circular-Dichroism as a Probe of Orbital Magnetization. Physical Review Letters, 1992. 68(12): p. 1943-1946.
54. Neel, L.J., Phys. Radium, 1954. 15: p. 376-378.
55. Hernando, A., Magnetic properties and spin disorder in nano-crystalline materials. Journal of Physics-Condensed Matter, 1999. 11(48): p. 9455-9482.
56. Skomski, R., Nano-magnetics. Journal of Physics-Condensed Matter, 2003. 15(20): p. R841-R896.
57. Delin, A. and E. Tosatti, Magnetic phenomena in 5d transition metal nano-wires. Physical Review B, 2003. 68(14).
58. Sampedro, B., et al., Ferromagnetism in fcc twinned 2.4 nm size Pd nanoparticles. Physical Review Letters, 2003. 91(23).
59. Shinohara, T., T. Sato, and T. Taniyama, Surface ferromagnetism of Pd fine particles. Physical Review Letters, 2003. 91(19).
60. Brust, M., et al., Synthesis of Thiol-Derivatized Gold Nanoparticles in a 2-Phase Liquid-Liquid System. Journal of the Chemical Society-Chemical Communications, 1994(7): p. 801-802.
61. Singh, R.K. and D. Kumar, Pulsed laser deposition and characterization of high-T-c YBa2Cu3O7-x superconducting thin films. Materials Science & Engineering R-Reports, 1998. 22(4): p. 113-185.
62. Wende, H., Recent advances in X-ray absorption spectroscopy. Reports on Progress in Physics, 2004. 67(12): p. 2105-2181.
63. Eriksson, O., et al., Orbital Magnetism in Fe, Co, and Ni. Physical Review B, 1990. 42(4): p. 2707-2710.
64. Soderlind, P., et al., Spin and Orbital Magnetism in Fe-Co and Co-Ni Alloys. Physical Review B, 1992. 45(22): p. 12911-12916.
65. Ebert, H., et al., L-edge X-ray absorption in fcc and bcc Cu metal: Comparison of experimental and first-principles theoretical results. Physical Review B, 1996. 53(23): p. 16067-16073.
66. J. StoK hr, Y.W., in: A.S. Schlachter, F.J. Wuilleumier(Eds.), New Directions in Research with

Third-Generation Soft X-ray Synchrotron Radiation Sources. Kluwer Aca- demic Publishers, Netherlands, 1994: p. p. 221.
67. Stohr, J., Journal of Magnetism and Magnetic Materials. 1999(200): p. 470-497.
68. Carra, P., et al., X-ray Circular-Dichroism and Local Magnetic-Fields. Physical Review Letters, 1993. 70(5): p. 694-697.
69. Garzon, I.L., et al., Do thiols merely passivate gold nano-clusters? Physical Review Letters, 2000. 85(24): p. 5250-5251.
70. A. Tiwari, M.S., D. Kumar, J. T. Abiade, 2008. 92(062509).
71. T. Minami, H.S., H. Nanto, S. Takata, J. Appl. Phys., 1985: p. part 2, 24, L781.
72. Kuo, F.L., et al., A comparative study of the photoluminescence and conduction mechanisms of low temperature pulsed laser deposited and atomic layer deposited zinc oxide thin films. Physica Status Solidi a-Applications and Materials Science, 2010. 207(11): p. 2487-2491.
73. H. Kato, M.S., K. Miyamoto, T. Yao, 2002. 538(237–239).
74. C. G. Van de Walle, D.B.L., G. F. Neumark, and S. T. Pantelides, 1993. 47(9425).
75. D. C. Look, D.C.R., C. W. Litton, R. L. Jones, D. B. Eason, G. Cantwell, 2002. 81(1830).
76. Zunger, A., 2003. 83(57).
77. Wei, S.-H., 2004. 30(337).
78. Yan, Y.F., M.M. Al-Jassim, and S.H. Wei, Doping of ZnO by group-IB elements. Applied Physics Letters, 2006. 89(18).
79. Volnianska, O., et al., Theory of doping properties of Ag acceptors in ZnO. Physical Review B, 2009. 80(24).
80. Sun, L.J., et al., Effects of S incorporation on Ag substitutional acceptors in ZnO:(Ag, S) thin films. Solid State Communications, 2009. 149(39-40): p. 1663-1665.
81. H. S. Kang, B.D.A., J. H. Kim, G. H. Kim, S. H. Lim, H. W. Chang, S. Y. Lee, 2006. 88(202108).
82. Cao, Y.G., et al., Low resistivity p-ZnO films fabricated by sol-gel spin coating. Applied Physics Letters, 2006. 88(25).
83. Fujihara, S., C. Sasaki, and T. Kimura, Crystallization behavior and origin of c-axis orientation in sol-gel-derived ZnO : Li thin films on glass substrates. Applied Surface Science, 2001. 180(3-4): p. 341-350.
84. Turner, N.H. and A.M. Single, Determination of Peak Positions and Areas from Wide-Scan Xps Spectra. Surface and Interface Analysis, 1990. 15(3): p. 215-222.
85. Pireaux W.A., L.M., Thiry P.A., Delrue J.P., Caudano R., Surf. Sci., 1984. 141(221).
86. Juodkazis, K., et al., XPS studies on the gold oxide surface layer formation. Electrochemistry Communications, 2000. 2(7): p. 503-507.
87. Aita, C.R. and N.C. Tran, Core Level and Valence Band X-ray Photoelectron-Spectroscopy of Gold Oxide. Journal of Vacuum Science & Technology a-Vacuum Surfaces and Films, 1991. 9(3): p. 1498-1500.
88. Zhang, S.B., S.H. Wei, and A. Zunger, Intrinsic n-type versus p-type doping asymmetry and the defect physics of ZnO. Physical Review B, 2001. 63(7).
89. Abiade, J.T., et al., Structural and magnetic properties of self-assembled nickel nanoparticles in a yttria stabilized zirconia matrix. Thin Solid Films, 2008. 516(8): p. 2082-2086.
90. Melendrez, M.F., G. Cardenas, and M.S. Palencia, Colloidal Germanium Nanoparticles and Nano-cubes Synthesized by Chemical Liquid Deposition. Advanced Science Letters, 2011. 4(2): p. 526-535.
91. Simakin, A.V., et al., Nanoparticles produced by laser ablation of solids in liquid environment. Applied Physics a-Materials Science & Processing, 2004. 79(4-6): p. 1127-1132.

92. Link, S., et al., Laser-induced shape changes of colloidal gold nano-rods using femtosecond and nano-second laser pulses. Journal of Physical Chemistry B, 2000. 104(26): p. 6152-6163.
93. Waller, G.H., A. Stein, and J.T. Abiade, Nano-fabrication of doped, complex oxides. Journal of Vacuum Science & Technology B, 2012. 30(1).
94. Kumar, B. and R.K. Thareja, Synthesis of nanoparticles in laser ablation of aluminum in liquid. Journal of Applied Physics, 2010. 108(6).
95. Patil, P.P., et al., Pulsed-Laser Induced Reactive Quenching at a Liquid-Solid Interface - Aqueous Oxidation of Iron. Physical Review Letters, 1987. 58(3): p. 238-241.
96. Tang, E.J., et al., Surface modification of zinc oxide nano-particle by PMAA and its dispersion in aqueous system. Applied Surface Science, 2006. 252(14): p. 5227-5232.
97. Abiade, J.T., et al., A tribochemical study of ceria-silica interactions for CMP. Journal of the Electrochemical Society, 2006. 153(11): p. G1001-G1004.
98. Liufu, S.C., H.N. Xiao, and Y.P. Li, Effect of MA-Na copolymer adsorption on the colloidal stability of nano--sized ZnO suspension. Materials Letters, 2005. 59(27): p. 3494-3497.
99. Dange, C., et al., Adsorption mechanism and dispersion efficiency of three anionic additives [poly(acrylic acid), poly(styrene sulfonate) and HEDP] on zinc oxide. Journal of Colloid and Interface Science, 2007. 315(1): p. 107-115.
100. Liufu, S., H. Xiao, and Y.P. Li, Investigation of PEG adsorption on the surface of zinc oxide nanoparticles. Powder Technology, 2004. 145(1): p. 20-24.
101. Hong, N.H., et al., Room-temperature ferromagnetism observed in undoped semiconducting and insulating oxide thin films. Physical Review B, 2006. 73(13).
102. Sundaresan, A., et al., Ferromagnetism as a universal feature of nanoparticles of the otherwise nonmagnetic oxides. Physical Review B, 2006. 74(16).
103. Coey, J.M.D., d(0) ferromagnetism. Solid State Sciences, 2005. 7(6): p. 660-667.
104. Xing, G.Z., et al., Correlated d(0) ferromagnetism and photoluminescence in undoped ZnO nano-wires. Applied Physics Letters, 2010. 96(11).
105. Oba, F., et al., Defect energetics in ZnO: A hybrid Hartree-Fock density functional study. Physical Review B, 2008. 77(24).
106. Banerjee, S., et al., Enhancement of ferromagnetism upon thermal annealing in pure ZnO. Applied Physics Letters, 2007. 91(18).